

Electronic Thesis and Dissertation Repository

8-10-2017 2:00 PM

A biomechanical approach for real-time tracking of lung tumors during External Beam Radiation Therapy (EBRT)

Elham Karami, *The University of Western Ontario*

Supervisor: Abbas Samani, *The University of Western Ontario*

: Ting-Yim Lee, *The University of Western Ontario*

A thesis submitted in partial fulfillment of the requirements for the Doctor of Philosophy degree in Medical Biophysics

© Elham Karami 2017

Follow this and additional works at: <https://ir.lib.uwo.ca/etd>



Part of the [Biomedical Engineering and Bioengineering Commons](#)

Recommended Citation

Karami, Elham, "A biomechanical approach for real-time tracking of lung tumors during External Beam Radiation Therapy (EBRT)" (2017). *Electronic Thesis and Dissertation Repository*. 4816.
<https://ir.lib.uwo.ca/etd/4816>

This Dissertation/Thesis is brought to you for free and open access by Scholarship@Western. It has been accepted for inclusion in Electronic Thesis and Dissertation Repository by an authorized administrator of Scholarship@Western. For more information, please contact wlsadmin@uwo.ca.

Abstract

Lung cancer is the most common cause of cancer related death in both men and women. Radiation therapy is widely used for lung cancer treatment. However, this method can be challenging due to respiratory motion. Motion modeling is a popular method for respiratory motion compensation, while biomechanics-based motion models are believed to be more robust and accurate as they are based on the physics of motion. In this study, we aim to develop a biomechanics-based lung tumor tracking algorithm which can be used during External Beam Radiation Therapy (EBRT). An accelerated lung biomechanical model can be used during EBRT only if its boundary conditions (BCs) are defined in a way that they can be updated in real-time. As such, we have developed a lung finite element (FE) model in conjunction with a Neural Networks (NNs) based method for predicting the BCs of the lung model from chest surface motion data.

To develop the lung FE model for tumor motion prediction, thoracic 4D CT images of lung cancer patients were processed to capture the lung and diaphragm geometry, trans-pulmonary pressure, and diaphragm motion. Next, the chest surface motion was obtained through tracking the motion of the ribcage in 4D CT images. This was performed to simulate surface motion data that can be acquired using optical tracking systems. Finally, two feedforward NNs were developed, one for estimating the trans-pulmonary pressure and another for estimating the diaphragm motion from chest surface motion data.

The algorithm development consists of four steps of: 1) Automatic segmentation of the lungs and diaphragm, 2) diaphragm motion modelling using Principal Component Analysis (PCA), 3) Developing the lung FE model, and 4) Using two NNs to estimate the trans-pulmonary pressure values and diaphragm motion from chest surface motion data. The results indicate that the Dice similarity coefficient between actual and simulated tumor volumes ranges from 0.76 ± 0.04 to 0.91 ± 0.01 , which is favorable. As such, real-time lung tumor tracking during EBRT using the proposed algorithm is feasible. Hence, further clinical studies involving lung cancer patients to assess the algorithm performance are justified.

Keywords

Lung cancer, respiratory motion, real-time motion tracking, lung biomechanical model, Finite Element Method, Principal Component Analysis, indirect motion tracking, chest motion, surrogate signal, Neural Networks, intra-fraction motion, inter-fraction motion

Co-Authorship Statement

The following thesis is comprised of four manuscripts: one published manuscript, and three manuscripts submitted to journals and being under review.

In Chapter 2, “Anatomy-based algorithm for automatic segmentation of human diaphragm in non-contrast CT images” by Elham Karami, Yong Wang, Stewart Gaede, Ting-Yim Lee, and Abbas Samani published in *J. Med. Imag.* 3(4), 046004 (Nov 22, 2016) is presented. Dr Yong Wang, an expert radiologist, helped with the manual segmentation of the diaphragm which was required for the algorithm validation. Dr. Samani helped with the study design and interpretation of results. I designed the algorithm, implemented the algorithm in ITK, prepared the raw data, analyzed, and interpreted the results, and wrote the manuscript under guidance and supervision of Drs. Samani, Lee, and Gaede.

In Chapter 3, “In-vivo lung biomechanical model for effective tumor motion tracking in external beam radiation therapy” under review in *Medical Physics Journal*, by Elham Karami, Stewart Gaede, Ting-Yim Lee, and Abbas Samani is presented. Dr. Samani helped with the study design and interpretation of results. I developed the lung biomechanical model, tested the model on patient data, and wrote the manuscript under guidance and supervision of Drs. Samani, Lee, and Gaede.

In Chapter 4, “Novel PCA-based model of human diaphragm motion derived from 4D CT Images for effective tumor motion management” under review in *J. Med. Imag.*, by Elham Karami, Stewart Gaede, Ting-Yim Lee, and Abbas Samani is presented. Dr. Samani helped with study design and interpretation of results. I developed the PCA-based diaphragm motion model, tested the model on patient data, and wrote the manuscript under guidance and supervision of Drs. Samani, Lee, and Gaede.

In Chapter 5, “A Neural Network approach for biomechanics-based tracking of lung tumors during External Beam Radiation Therapy (EBRT)” submitted to *Expert Systems with Applications Journal*, by Elham Karami, Stewart Gaede, Ting-Yim Lee, and Abbas Samani is presented. Dr. Samani helped with study design and interpretation of results. I developed

the model, tested the model on patient data, and wrote the manuscript under guidance and supervision of Drs. Samani, Lee, and Gaede.

Dedication

To my loving parents who are the most honest and pure people I know.

Acknowledgements

During my graduate studies, I had the opportunity to work with several people and I would like to seize this opportunity to thank these individuals without their supports, this achievement would not have been realized.

I would like to thank my primary supervisor, Dr Samani, for his forward and continuous encouragements during my PhD studies. He is one the best teachers and mentors I have ever known and I would like to thank him for being extremely caring and supportive. I was also very lucky to have the opportunity of being co-supervised by Dr Lee who kindly guided me through this project and helped me develop different vision on medical problems. The best part about being supervised by my two supervisors was that they are both great, honest, hardworking people and working with them was a source of inspiration for me.

I also appreciate the input provided by members of my advisory committee, Dr. Gaede, and Dr. Wong. I also thank my colleagues here at Western for their support and frequent constructive comments they provided which often inspired me to move forward with my PhD project.

My deepest gratitude goes to my kind family, specially my parents. I have the most loving parents and siblings and nothing was harder than living thousands of kilometers far from them. Despite the huge distance, they managed to make me feel they are right here, beside me.

Table of contents

Abstract	i
Co-Authorship Statement.....	iii
Dedication	v
Acknowledgements.....	vi
Table of contents.....	vii
List of Tables	xi
List of Figures	xiii
List of Appendices	xix
List of Abbreviations	xx
1 « Introduction ».....	1
1.1 Lung Cancer	1
1.2 Treatment Strategies for NSCLC	4
1.2.1 Surgical resection.....	4
1.2.2 Chemotherapy.....	4
1.2.3 Radiation therapy	5
1.2.4 External beam radiation therapy	5
1.3 Respiratory induced target motion.....	7
1.3.1 Anatomy of the respiratory system.....	7
1.3.2 Physiology of the respiratory system.....	7
1.4 Motion compensation methods	9
1.4.1 Motion encompassing methods.....	10
1.4.2 Respiratory gating methods	11
1.4.3 Breath-hold methods.....	11
1.4.4 Real-time tracking methods	11
1.5 The proposed tracking method and theory.....	13
1.6 Connected component labeling	16
1.7 Simple Region Growing (SRG) Algorithm.....	17
1.8 Circle Hough transform.....	18
1.9 The Theory of Elasticity.....	20

1.9.1	Finite Elasticity	20
1.9.2	Infinitesimal versus finite (large) deformation	22
1.9.3	Stress Tensor and Principle of Linear Momentum	22
1.9.4	Linear Elastic Material.....	24
1.9.5	Hyper-elastic material.....	25
1.10	Principal Component Analysis	27
1.11	Neural Networks.....	28
1.11.1	Feedforward neural network.....	31
1.11.2	Training MLP: The Back-Propagation Algorithm.....	32
1.12	Research Objectives	35
1.13	Thesis Roadmap	36
1.13.1	Chapter 2 - Anatomy-based algorithm for automatic segmentation of the human diaphragm in non-contrast CT images	36
1.13.2	Chapter 3 - In-vivo lung biomechanical model for effective tumor motion tracking in external beam radiation therapy.....	37
1.13.3	Chapter 4 - Novel PCA-based Model of Human Diaphragm Motion Derived from 4D CT Images for Effective Tumor Motion Management	37
1.13.4	Chapter 5 - A Neural Network Approach for Biomechanics-based Tracking of Lung Tumors during External Beam Radiation Therapy	37
1.13.5	Chapter 6 – Conclusions and future work.....	38
1.14	References	38
Chapter 2	« Anatomy-based algorithm for automatic segmentation of human diaphragm in non-contrast CT images ».....	46
2.1	Introduction	46
2.2	Diaphragm Anatomy	48
2.3	Methods.....	50
2.3.1	Data Acquisition	50
2.3.2	Diaphragm Segmentation Algorithm.....	50
2.4	Results	60
2.5	Discussion	64
2.6	Conclusion.....	67
2.7	References	68
Chapter 3	« In-vivo lung biomechanical model for effective tumor motion tracking in external beam radiation therapy ».....	72

3.1	Introduction	72
3.2	Materials & Methods.....	76
3.2.1	Physiology of breathing	76
3.2.2	Data acquisition	78
3.2.3	Lung geometry and finite element mesh.....	78
3.2.4	Tissue mechanical properties.....	79
3.2.5	Boundary conditions	79
3.2.6	Diaphragm.....	80
3.2.7	The trans-pulmonary pressure.....	81
3.2.8	Validation.....	83
3.2.9	Implementation	84
3.3	Results	84
3.3.1	Qualitative validation.....	84
3.3.2	Quantitative validation.....	87
3.4	Discussion and Conclusions.....	89
3.5	References	91
Chapter 4	« Novel PCA-based Model of Human Diaphragm Motion Derived from 4D CT Images for Effective Tumor Motion Management »	96
4.1	Introduction	96
4.2	Materials and methods	98
4.2.1	Overview of expert system for lung tumor tracking.....	98
4.2.2	Data acquisition	100
4.2.3	Image segmentation and registration	101
4.2.4	Landmark set selection using trans-finite interpolation.....	101
4.2.5	Principal component analysis	104
4.2.6	Validation.....	105
4.3	RESULTS.....	106
4.3.1	Actual and PCA model based displacements comparison.....	106
4.3.2	Biomechanics based tumor tracking results using the “true” and PCA model based diaphragm displacements.....	113
4.4	Discussion and conclusions.....	115
4.5	References	117

Chapter 5	« A Neural Network Approach for Biomechanics-based Tracking of Lung Tumors during External Beam Radiation Therapy »	123
5.1	Introduction	123
5.2	Materials and methods	126
5.2.1	Data acquisition	126
5.2.2	Rib motion tracking for obtaining the chest motion data	127
5.2.3	Diaphragm motion and trans-pulmonary pressure data	129
5.2.4	Neural Networks Training	132
5.2.5	Validation.....	134
5.3	Results	135
5.3.1	Qualitative validation.....	135
5.3.2	Quantitative validation.....	137
5.4	Discussion and Conclusions.....	141
5.5	References	144
Chapter 6	« Summary, Conclusion, and Future Work »	149
6.1	Summary	149
6.2	Conclusions and Future Directions	153
6.3	Closing Remarks	154
Appendices.....		156
Appendix A: Research Ethics		156
Curriculum vitae		157

List of Tables

Table 1-1 The TNM staging of lung cancer. The table is adopted from Sobin et al.	4
Table 2-1 Results summarizing the comparison between the automatic and manual segmentation of the diaphragm of 9 patients using the mean distance to the closest point (MDCP), Housdorff distance, Average Symmetric Absolute Surface Distance (ASASD) and Symmetric RMS Surface Distance (SRMSSD).	64
Table 3-1 The Dice similarity coefficient values between actual and simulated GTVs (optimization step). The simulation has been performed between time point #6 (end exhalation phase) and the other 5 time points moving backward.	88
Table 3-2 The Dice similarity coefficient values between actual and simulated GTVs (validation step). The simulation has been performed between time point #6 (end exhalation phase) and the other 4 time points moving forward.	88
Table 4-1 Tumor displacement values in LR, AP and SI directions obtained from “true” diaphragm motion data and the PCA model-generated diaphragm displacement field. The displacement errors resulting from the two different boundary conditions and the Mean±SD values are also provided.	115
Table 5-1 Mean error in inter-fraction diaphragm motion (mm) and trans-pulmonary pressure (cmH2O) prediction for subjects #4 and #5.	139
Table 5-2 Dice similarity coefficient between actual Gross Tumor Volume (GTV) and the lung biomechanical model estimated GTV for three subjects over the full respiratory cycle. The lung biomechanical model is driven with image derived (actual) boundary conditions. These patients were used to assess the algorithm performance in estimating the intra-fraction motion variation.	140
Table 5-3 Dice similarity coefficient between actual Gross Tumor Volume (GTV) and the lung biomechanical model estimated GTV for two subjects over the full respiratory cycle. The lung biomechanical model is driven with image derived (actual) boundary conditions. These patients were used to assess the algorithm performance in estimating the inter-fraction motion variation.	140
Table 5-4 Dice similarity coefficient between actual Gross Tumor Volume (GTV) and the lung biomechanical model estimated GTV for four subjects over the full respiratory cycle. The lung biomechanical model is driven with Neural Network estimated BCs.	

These patients were used to assess the algorithm performance in estimating the intra-fraction motion variation.....	141
Table 5-5 Dice similarity coefficient between actual Gross Tumor Volume (GTV) and the lung biomechanical model estimated GTV for four subjects over the full respiratory cycle. The lung biomechanical model is driven with Neural Network estimated BCs. These patients were used to assess the algorithm performance in estimating the inter-fraction motion variation.....	
	141

List of Figures

Figure 1–1 Age standardized net survival versus survival duration for prostate, female breast, colorectal and lung cancers. Ages 15-99, Canada (excluding Quebec), 2006-2008. Adopted from “Canadian Cancer Statistics” ²	1
Figure 1–2 Color wash of the dose distribution for a lung cancer patient where the dose deposited along the paths of the beam is shown in purple. Adopted from Rana et al. ¹²	6
Figure 1–3 (a) The alveolar, pleural, and trans-pulmonary pressures. (b) Changes in the amplitude of intra-alveolar, intra-pleural, and trans-pulmonary pressures during respiratory cycle.....	9
Figure 1–4 The Gross Tumor Volume (GTV) delineated at (a) end-inhalation and, (b) end-exhalation phase of respiration. (c) The green contour depicts Internal Target Volume (ITV) obtained from combining the GTVs, while the Planning Target Volume (PTV) is shown in yellow. Adopted from Glide-Hurst et al ¹⁵	10
Figure 1–5 A block diagram of lung tumor tracking algorithm which involves a pre-treatment and an intra-treatment step. (a) Pre-treatment tracking of chest surface motion and image based estimation of the lung boundary conditions. The lung BCs include lung-diaphragm contact surface displacements shown in orange and lung trans-pulmonary pressure shown in purple. (b) Constructing a correlation model (e.g. using neural network (NN) between chest surface motion data and lung boundary conditions. The NN training requires the diaphragm to be presented in a compact form. (c) Chest surface motion tracking during treatment and predicting the boundary conditions in real-time. (d) Calculating lung tumor position and deformation using an accelerated lung biomechanical model.	14
Figure 1–6 (a) An example of a binary image including three connected components. (b) The labeled connected components.	17
Figure 1–7 (a) An image of the original circle. (b) The parametric representation of the original circle. The local maxima point, i.e. the intersection of circles is the center of original circle.	19
Figure 1–8 A general elastic object at undeformed (time t_0) and deformed (time t) states.	20
Figure 1–9 A very small cubic particle within the elastic material.	23

Figure 1–10 A single neuron.....	29
Figure 1–11 The most common neuron activation functions. (a) Sigmoid, (b) tanh, (c) ReLU.....	30
Figure 1–12 An example of feedforward neural network.....	31
Figure 2–1 (a) A schematic view of the human diaphragm where surrounding structures (e.g. ribs and aorta) are shown, (b) an axial CT image showing the aorta and diaphragm pillars, (c) a schematic view of the human diaphragm and (d) a coronal CT image showing the relative positions of the thoracic organs and abdominal organs.....	49
Figure 2–2 Block diagram of the proposed segmentation method.	51
Figure 2–3 (a) The intersection area between the first axial slice of the 3D CT volume and the trachea being segmented by image thresholding used to find the initial seed point for bronchial tree segmentation. (b) The red box depicts the trachea (oval area) which is usually present in the first axial slice of the CT image.	53
Figure 2–4 (a) A coronal sub-image containing the heart which has been thresholded for values smaller than 35 HU, (b) The zero voxels in the thresholded binary sub-image are labeled as “contained” (blue) and “uncontained” (black) voxels, (c) The color labeled connected components of the “contained” voxels, and (d) Segmented heart overlaid on the CT image.....	55
Figure 2–5 The diaphragm’s contact surfaces with both lungs obtained from applying an arc detection algorithm on the most inferior voxels of both lungs.	56
Figure 2–6 (a) A sub-image (within the shown box) containing the heart’s contact surface with the diaphragm, and (b) The segmented heart’s contact surface with the diaphragm obtained from applying the Canny edge detection algorithm on the selected sub-image.....	57
Figure 2–7 (a) Segmented ribcage and aorta after performing morphological image closing overlaid on the CT image and (b) Axial section of the contact surface between the diaphragm, ribs, spine, and aorta.	58
Figure 2–8 The results obtained for subject #1. The 1 st row depicts automatically delineated (blue) sections of the diaphragm overlaid on their manually delineated counterpart (white). (a) and (b) are coronal and (c) is an axial view. The 2 nd row depicts 3D construction of the diaphragm surface. (d) front, (e) back and (f) top views.	61

Figure 2–9 The results obtained for subject #2. The 1st row depicts automatically delineated (blue) sections of the diaphragm overlaid on their manually delineated counterpart (white). (a) and (b) are coronal and (c) is an axial view. The 2nd row depicts 3D construction of the diaphragm surface. (d) front, (e) back and (f) top views. 62

Figure 2–10 The results obtained for subject #3. The 1st row depicts automatically delineated (blue) sections of the diaphragm overlaid on their manually delineated counterpart (white). (a) and (b) are coronal and (c) is an axial view. The 2nd row depicts 3D construction of the diaphragm surface. (d) front, (e) back and (f) top views. 62

Figure 3–1 A block diagram of lung tumor tracking algorithm which involves a pre-treatment and an intra-treatment step. (a) Pre-treatment tracking of chest surface motion and image based estimation of the lung boundary conditions. The lung BCs include lung-diaphragm contact surface displacements shown in orange and lung trans-pulmonary pressure shown in purple. (b) Building a correlation model (e.g. using neural network (NN) between chest surface motion data and lung boundary conditions. The NN training requires the diaphragm to be presented in a compact form. (c) Intra-treatment chest surface motion tracking and predicting the boundary conditions in real-time. (d) Calculating lung tumor position and deformation using an accelerated lung biomechanical model. 74

Figure 3–2 (a) The alveolar, pleural, and trans-pulmonary pressures. (b) Changes in the amplitude of intra-alveolar, intra-pleural, and trans-pulmonary pressures during respiratory cycle. 77

Figure 3–3 (a) Coronal and (b) sagittal views of the lung mesh with tumor elements depicted as red. 79

Figure 3–4 (a) Diaphragm nodes. (b) The trans-pulmonary pressure is applied on the lung surface shown in red. 80

Figure 3–5 The lung was segmented, excluding dense features such as tumor and major blood vessels and airways, to be used for optimization. The left image corresponds to end inhale phase and the right image corresponds to end exhale phase while the 3 images in the middle represent phases in between. 82

Figure 3–6 Block diagram of the proposed optimization framework for patient specific calculation of trans-pulmonary pressure and Poisson’s ratio values. The optimization

requires the lung FE mesh at end exhale, and the diaphragm displacement values obtained from registration. Initial values of trans-pulmonary pressure magnitude and Poisson’s ratio are assigned to the model and the deformed lung mesh corresponding to the target phase is obtained. The deformed mesh is used in conjunction with Thin Plate Spline registration method to create the simulated image and calculate the cost. 83

Figure 3–7 Optimized values of (a) trans-pulmonary pressure and (b) Poisson’s ratio values vs. respiration phase. Phases 1, 6 and 10 represent start exhalation, end exhalation and end inhalation, respectively..... 85

Figure 3–8 CT image difference between actual “end exhalation” and “end inhalation” CT images (a), (b), (c) and difference between actual and simulated “end inhalation” CT images (d), (e), (f) for the 3 subjects..... 86

Figure 3–9 (a) Mean absolute error per landmark’s 3D position versus respiration phase. (b) Mean distance between actual and simulated lung surfaces versus respiration phase.89

Figure 4–1 A block diagram of lung tumor tracking system. It involves four steps of (a) pre-treatment chest surface motion tracking and image based estimation of the lung boundary conditions. These boundary conditions include prescribed displacement boundary conditions of lung bottom surface which is equal to diaphragm surface displacements shown in orange and lung pleural pressure shown in purple. (b) Fitting a function (e.g. using neural network (NN) which maps chest surface data to lung boundary conditions. This fitting requires the diaphragm to be presented in a compact form. (c) Intra-treatment chest surface data acquisition and mapping to boundary conditions in real-time. (d) Calculating lung tumor position using an accelerated lung biomechanical model..... 100

Figure 4–2 TFI domain meshing technique: (a) A 2D computational domain and (b) An example of a corresponding 2D physical domain..... 102

Figure 4–3 (a) 2D projection of the diaphragm’s dome in an axial plane intersecting with segmented 7th to 11th ribs, (b) Four corners points, A,B, C and D were used to partition the boundary of the dome, (c) Using the 7th to 11th ribs to obtain additional anatomical landmarks for TFI and (d) The final TFI grid with $6 \times 16 = 96$ landmarks. 104

Figure 4–4 Segmentation results for a diaphragm’s right dome, (a) Coronal view and (b) Sagittal view..... 106

Figure 4–5 Landmark selection for (a) patient H2 and (b) patient P6. Points shown with ‘+’ are generated by the TFI method. A subset of these points (shown with ‘o’) are selected for results comparison. 107

Figure 4–6 “True” (solid line) and model generated (dashed line) SI positions of Group #1 (a and b), Group #2 (c and d) and Group #3 (e and f) of landmarks. 108

Figure 4–7 The mean error per landmark (mm) in the LR(left), AP(middle) and SI(right) directions versus respiratory phase for subjects (a) H1, (b) H2, (c) P2, and (d) P6. 112

Figure 4–8 The Bland-Altman plots for subjects (a) H2 and (b) P6 indicating favorable agreement between “true” and model generated displacement fields. 113

Figure 4–9 (a) 3D FE model of the lung at end exhalation phase; (b) 3D displacement distribution superimposed on the end exhalation phase; (c) a sagittal section of the displacement distribution through the tumor and (d) a coronal section of the displacement distribution through the tumor. 114

Figure 5–1 A block diagram of lung tumor tracking system. It involves four steps of (a) pre-treatment chest surface motion tracking and image based estimation of the lung boundary conditions. These boundary conditions include prescribed displacement boundary conditions of lung bottom surface which is equal to diaphragm surface displacements shown in orange and lung trans-pulmonary pressure shown in purple. (b) Fitting a function (e.g. using neural network (NN) which maps chest surface data to lung boundary conditions. This fitting requires the diaphragm to be presented in a compact form. (c) Intra-treatment chest surface data acquisition and mapping to boundary conditions in real-time. (d) Calculating lung tumor position using an accelerated lung biomechanical model. 125

Figure 5–2 Segmented 8th, 9th and 10th left ribs, 6th and 10th right ribs and the sternum body..... 127

Figure 5–3 The x, y, and z displacement component data of segmented ribs and sternum body for subject #2..... 129

Figure 5–4 (a) The diaphragm nodes. (b), (c) and (d) corresponding SI, AP and LR displacement curves for subject #2. Each curve color in (b), (c), and (d) represents a node of the diaphragm. 130

Figure 5–5 Optimization framework used to calculate trans-pulmonary pressure at each phase of respiration. In this framework, a pre-developed lung biomechanical model for which the trans-pulmonary pressure acts as BC, is used to optimize the pressure. The cost function is the difference between the actual CT images and the images constructed using the deformed mesh and TPS image registration method.	131
Figure 5–6 (a)The optimized pressure curves for subjects #1, #2 and #3. (b)The pre-treatment (solid line) and follow-up (dashed line) optimized pressure curves for subjects #4 and #5.....	132
Figure 5–7 Normalized principal components of (a) chest, and (b)diaphragm motion data for subject #2.....	133
Figure 5–8 Feed forward NN used to estimate the diaphragm motion from chest motion data. The network has one hidden layer with two nodes.	134
Figure 5–9 Intra-fraction validation test. (a) Actual and NN estimated trans-pulmonary pressure curves, and (b) diaphragm motion principal components for subject #2.	136
Figure 5–10 Results obtained from inter-fraction motion estimation test. (a) Actual and NN-estimated trans-pulmonary pressure curves, and (b) diaphragm motion principal components for subject #4.	136
Figure 5–11 (a), (b) and (c) Mean error in pressure estimation vs respiration phase. (d), (e) and (f) Mean error in diaphragm motion estimation vs respiration phase.	138

List of Appendices

Appendix A: Research Ethics	Error! Bookmark not defined.
Curriculum vitae	Error! Bookmark not defined.

List of Abbreviations

3D	Three Dimensional
4D CT	Four-Dimensional Computed Tomography
AAM	Active Appearance Model
ANN	Artificial Neural Network
ASASD	Average Symmetric Absolute Surface Distance
COPD	Chronic Obstructive Pulmonary Disease
CT	Computed Tomography
DIBH	Deep Inspiration Breath Hold
EBRT	External Beam Radiation Therapy
FE	Finite Element
FEA	Finite Element Analysis
FFD	Free Form Deformation
GPU	Graphics Processing Unit
GTV	Gross Tumor Volume
ITK	Insight Toolkit
ITV	Internal Target Volume
MDCP	Mean Distance to the Closest Point
MLP	Multi-Layer Perceptron
NN	Neural Network
NSCLC	Non-Small Cell Lung Cancer
NTCP	Normal Tissue Complication Probability

OS	Overall Survival
PCA	Principal Component Analysis
PTV	Planning Target Volume
RMS	Root Mean Squared
RPM	Real-time Position Management™
SCLC	Small Cell Lung Cancer
SRG	Simple Region Growing
SRMSSD	Symmetric RMS Surface Distance
TCP	Tumor Control Probability
TFI	Trans-finite Interpolation
TNM	Tumor Node Metastases
TPS	Thin Plate Spline

Chapter 1

1 « Introduction »

1.1 Lung Cancer

According to statistics, cancer is the leading cause of death in most countries¹. The Canadian Cancer Society predicted that in 2016, 202,400 individuals will suffer from cancer, and ~40% of them will die of this disease². Lung and bronchus, breast, colorectal, and prostate cancer account for half the cancer incidents, while the number of deaths caused by lung cancer is more than the other three major cancers combined. As shown in Figure 1-1, which depicts the net survival for the four major cancers, the 5-year survival rate of lung cancer is only 17% which is very low compared to the other three cancers.

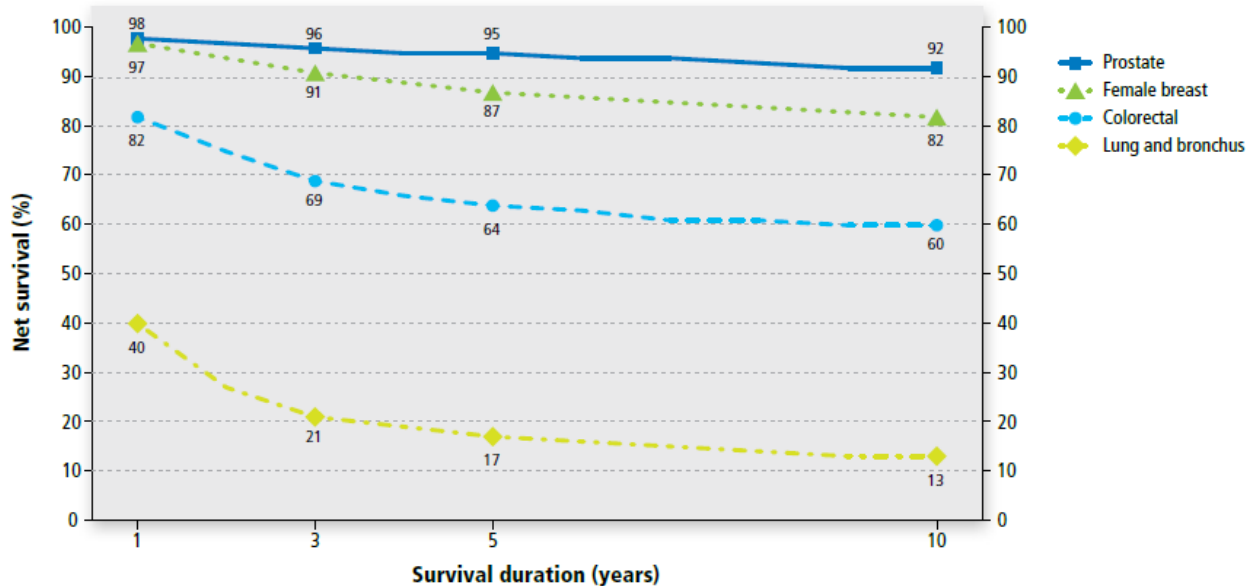


Figure 1–1 Age standardized net survival versus survival duration for prostate, female breast, colorectal and lung cancers. Ages 15-99, Canada (excluding Quebec), 2006-2008. Adopted from “Canadian Cancer Statistics”².

There are two types of lung cancer, small cell lung cancer (SCLC) and non-small cell lung cancer (NSCLC), with 85% of the patients being diagnosed with the latter. SCLC, which is also known as oat cell carcinoma or small cell undifferentiated carcinoma, is the most aggressive type of lung cancer that usually starts in the bronchi in the center of the lungs³. NSCLC has subtypes which differ in the type of lung cells from which the disease originates. They are grouped as NSCLC because the treatment approach for them is similar. Adenocarcinoma, which accounts for 40% of lung cancers, starts in the glandular cells in the outer part of the lung. Squamous cell carcinoma initiates in squamous cells lining the bronchus. Finally, large cell carcinoma which exhibits rapid progression can grow anywhere in the lung⁴.

The treatment method is decided based on patients TNM staging which denotes the status of tumor, node, and metastasis. Table 1-1 depicts the TNM staging for NSCLC⁵.

Stage	Tumor(T)	Nodal(N)	Metastasis(M)	5-year survival
0	Tis	N0	M0	
IA	T1a, b	N0	M0	49%
IB	T2a	N0	M0	45%
IIA	T2b	N0	M0	30%
	T1a, b	N1	M0	
	T2a	N1	M0	
IIB	T2b	N1	M0	31%
	T3	N0	M0	
IIA	T1a, b, T2a	N2	M0	14%
	T3	N1, N2	M0	
	T4	N0, N1	M0	

IIIB	T4	N2	M0	5%
	Any T	N3	M0	
IV	Any T	Any N	M1	1%

T denotes tumor size:

is: Carcinoma in situ

1: Surrounded by lung or visceral lung without invasion into the main bronchus.

1a: Tumor 2cm or less in greatest direction

1b: Tumor more than 2 cm but less than 3 cm in greatest direction

2: Tumor has any of: involves main bronchus, 2 cm or more from carina; or invades visceral pleura; or associated with obstructive pneumonitis that extends to the hilar region but does not involve entire lung

2a: Tumor more than 3 cm but less than 5 cm in greatest direction

2b: Tumor more than 5 cm but less than 7 cm in greatest direction

3: Tumor has any of: more than 7 cm; invades any of parietal wall, parietal pericardium, mediastinal pleura, chest wall, diaphragm, and phrenic nerve; involves main bronchus at less than 2 cm distal to the carina but not involving the carina; or associated with pneumonitis or the entire lung, or separate tumor nodule(s) in the same lobe as primary

4: Tumor has any of: invades mediastinum, heart, great vessels, trachea, recurrent laryngeal nerve, oesophagus, vertebral body, or carina; or separate tumor nodules in different ipsilateral lobe to that of the primary

N denotes extent of regional Lymph Node spread

0: No regional lymph node metastasis

1: Metastasis in ipsilateral peribronchial and/or ipsilateral hilar lymph nodes and intrapulmonary nodes, including involvement by direct extension

2: Metastasis in ipsilateral mediastinal and/or sub-carinal lymph nodes

3: Metastasis in: contralateral mediastinal, contralateral hilar, ipsilateral, or contralateral scalene, and supraclavicular nodes

M denotes distant metastases

0: No distant metastasis

1: Distant metastases present

Table 1-1 The TNM staging of lung cancer. The table is adopted from Sobin et al.⁵

1.2 Treatment Strategies for NSCLC

1.2.1 *Surgical resection*

Types of surgery used to treat (and possibly cure) NSCLC include pneumonectomy, lobectomy, segmentectomy (or wedge resection) and sleeve resection⁶. Pneumonectomy is performed by removing an entire lung and is usually needed when the tumor is close to the center of the chest. Lobectomy involves removing the entire lobe containing the tumor(s). In segmentectomy, only part of a lobe is removed and it is the treatment of choice when the patient cannot withstand removing the whole lobe due to poor lung function. Sleeve resection is used to treat cancers in large airways in the lungs and similar to segmentectomy, the surgeon's goal is to preserve more lung function. With any of these operations, nearby lymph nodes are also removed to look for possible spread of the cancer. Lobectomy is the preferred type of operation for NSCLC as it provides better local control and overall survival (OS)⁷. Surgery is the standard of care for stage I and II NSCLC (sometimes stage III). However, it is often precluded due to significant co-morbidities, poor cardiac function, or decreased pulmonary reserve exhibited by the patient^{6,8}.

1.2.2 *Chemotherapy*

Chemotherapy is usually used as the main treatment method for NSCLC, when cancer has progressed too far or the patient cannot go through surgery due to poor health conditions. In addition, chemotherapy may be used before surgery to shrink the tumor (neoadjuvant

therapy), after surgery to kill remaining cancer cells (adjuvant therapy) or along with radiation therapy (concurrent therapy), when surgery is not an option^{6,9}.

1.2.3 Radiation therapy

Radiation therapy becomes the optimal treatment method for NSCLC when the lung tumor cannot be removed because of its size or location, when the patient cannot go through surgery due to poor health conditions, or if a person does not want surgery⁶. In addition, patients might receive radiation before surgery to shrink the tumor and make the operation easier. Also, post-surgery radiation therapy is frequently used to kill the remaining cancer cells that surgery might have missed. Finally, radiation treatment can serve as palliative therapy to relieve symptoms of advanced NSCLC such as pain, bleeding, trouble swallowing, and cough. As such, radiation therapy is used widely in almost all stages of NSCLC. Radiation can be delivered using external beams or internal seeds (Brachytherapy). The focus of this study is on External Beam Radiation Therapy (EBRT).

1.2.4 External beam radiation therapy

1.2.4.1 Three-dimensional conformal radiation therapy (3D-CRT)

In EBRT, high energy x-ray beams are used to target the cancerous tissue. In this process, the normal tissue located along the x-ray beam paths receives some radiation dose, as demonstrated for a sample patient in Figure 1-2. The goal of radiation treatment planning, which decides how the prescription dose is delivered and the dose distribution, is to maximize the tumor control probability (TCP) while minimizing the normal tissue complication probability (NTCP)¹⁰.

While conventional 2D-RT technique usually uses opposing anterior and posterior radiation fields, 3D-CRT uses multiple co-planar fields to maximize the tumor dose coverage and minimize the normal tissue exposure. In 3D-CRT, a prescription dose of 66 Gy or higher is delivered to the tumor over the course of six weeks, in 30 daily fractions. While such scheme results in low NTCP, the TCP and overall survival are low, leading inoperable patients to forego any treatment options¹¹. One solution to this problem is to

escalate the dose to NSCLC lesions, but the increase in dose is associated with increased dose to normal lung, resulting in high NTCP.

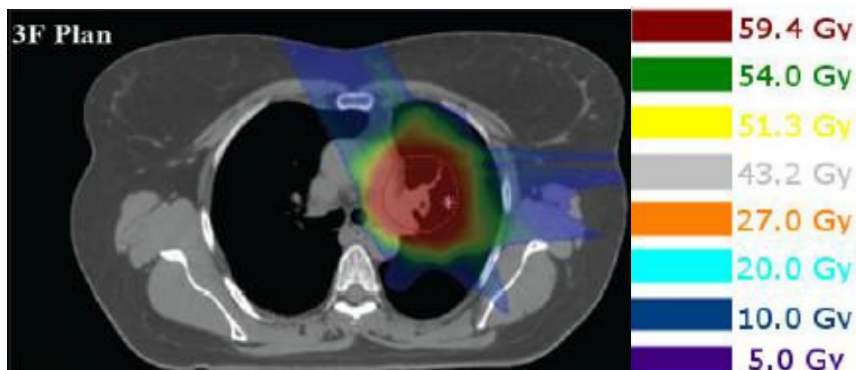


Figure 1–2 Color wash of the dose distribution for a lung cancer patient where the dose deposited along the paths of the beam is shown in purple. Adopted from Rana et al.¹²

1.2.4.2 Intensity modulated radiation therapy (IMRT)

IMRT involves using an automated optimization process, known as inverse treatment planning, to modulate the intensity of each beam delivered to the tumor. Using such optimization process, desired tumor coverage is achieved while healthy tissue is relatively spared. Using IMRT, higher radiation dose can be delivered to the tumor compared to 3D-CRT.

1.2.4.3 Stereotactic ablative body radiation therapy (SABR)

Stereotactic ablative body radiotherapy (SABR) is a hypo-fractionated treatment method which imitates the surgical knife in ablating the tumor with a high dose of radiation delivered in fewer (usually 1 to 5) treatment sessions compared to conventional treatment methods. A recent study¹⁰ on comparing the outcome of SABR and surgery for stage I and II NSCLC patients reported a 3-year OS of 95% for patients treated with SABR which is a significant improvement to the outcome of surgery which is 79%.

1.3 Respiratory induced target motion

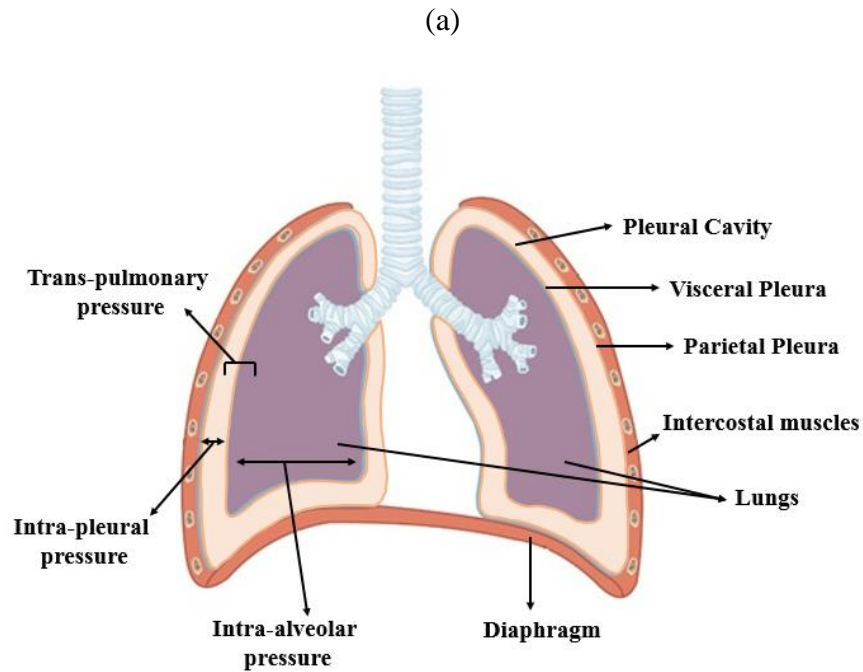
1.3.1 Anatomy of the respiratory system

The lungs are passive, pyramid-shaped organs that are connected to the trachea by the right and left bronchi. The inferior surface of the lungs is bordered by the diaphragm which is a thin dome-shaped sheath and acts as the primary muscle of respiration. The next important group of respiratory muscles are the external intercostals which are attached between the ribs and maintain the width of ribcage. Due to contraction of intercostal muscle fibers, each rib moves toward the rib above, with the overall effect of raising the ribcage and increasing the ribcage volume, assisting in inhalation. The left and right lungs are enveloped with the pleurae which are serous membranes attached to the mediastinum. The pleurae have two layers of visceral and parietal pleura, the former being superficial to the lungs and the latter being the outer layer that connects to the thoracic wall, the mediastinum, and the diaphragm. The pleural cavity is the space between the visceral and parietal pleura. The pleurae have two major roles. First, they produce pleural fluid which acts as lubricant to reduce the friction between visceral and parietal pleurae and prevent trauma during breathing. The produced lubricant is adhesive and causes the lungs to enlarge following the thoracic wall expansion. Second, the pleurae create cavities that separate major organs and prevent organ interference and spread of infection¹³.

1.3.2 Physiology of the respiratory system

Figure 1-3 (a) depicts a schematic of the respiratory system where the lungs, pleural cavity, trachea, and respiratory muscles are illustrated. Before inspiration, the respiratory muscles are relaxed and the intra-alveolar pressure is equal to the atmospheric pressure. The inspiration phase begins by contraction of the main respiratory muscles, i.e. diaphragm and external intercostals, and expansion of the chest cavity. The diaphragm is responsible for 75% of enlargement of thoracic cavity during inspiration while the contraction of external intercostals enlarges the thoracic cavity in lateral and AP dimensions. As the thoracic cavity expands, the intrapleural pressure drops and the lungs expand. This lung expansion leads to reduction of alveolar pressure; hence air flows in. At the end of inspiration, the inspiratory muscles relax, the diaphragm is dome-shaped again and the rib cage falls

because of gravity, once the external intercostals relax. As the chest wall and stretched lungs recoil, the volume decreases, the pressure increases; hence the air flows out. As shown in Figure 1-3 (a), the net pressure applied to the lung is the trans-pulmonary pressure which is the difference between the alveolar pressure and intrapleural pressure. It is noteworthy that the spatial distribution of trans-pulmonary pressure is not uniform¹⁴.



(b)

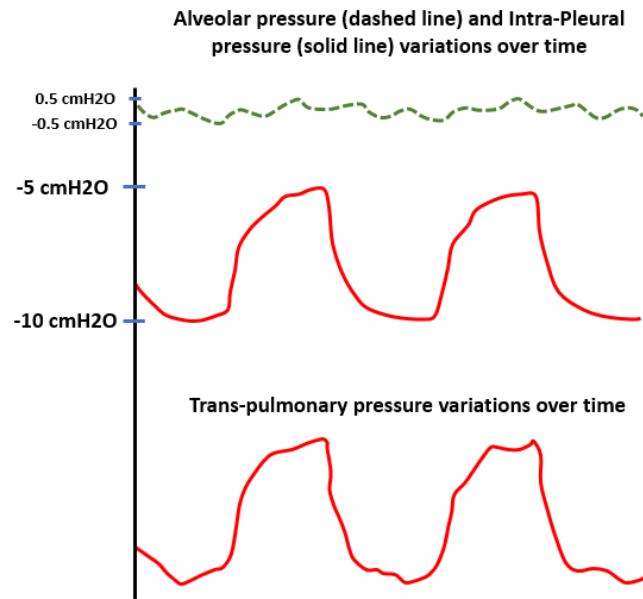


Figure 1–3 (a) The alveolar, pleural, and trans-pulmonary pressures. (b) Changes in the amplitude of intra-alveolar, intra-pleural, and trans-pulmonary pressures during respiratory cycle.

Figure 1-3 (b) depicts the temporal variations of the intra-alveolar and intra-pleural pressures during the respiratory cycle. The diaphragm and ribcage motion cause the temporal and spatial variations of the trans-pulmonary pressure, while the bottom surface of the lungs undergo loading created by diaphragm motion. As such, two different mechanisms cause the respiratory motion. These mechanisms might be out of phase and lung disease such as Chronic Obstructive Pulmonary Disease (COPD) and cancer affect both mechanisms. Therefore, the respiratory motion is usually irregular and difficult to model.

1.4 Motion compensation methods

The methods used to compensate for tumor motion are divided into four groups of 1) Motion encompassing methods, 2) Respiratory gating methods, 3) Breath-hold methods, and 4) Real-time tumor tracking methods.

1.4.1 Motion encompassing methods

Most radiotherapy facilities are not equipped with radiation delivery systems which account for respiratory motion, i.e. the tumor motion is present during radiation treatment. As such, the tumor mean position and its range of motion should be obtained prior to treatment to plan for radiation delivery accordingly. Four-Dimensional Computed Tomography (4D-CT) is the most popular approach which integrates organ motion into the acquisition of the CT data set and facilitates treatment planning. Each 4D-CT data set includes volumetric images obtained at different respiratory phases. For each 3D CT image in a 4D CT set, the Gross Tumor Volume (GTV) can be obtained to form the Internal Target Volume (ITV) by combining all GTVs. The GTV, ITV and Planning Target Volume (PTV) are shown in Figure 1-4.

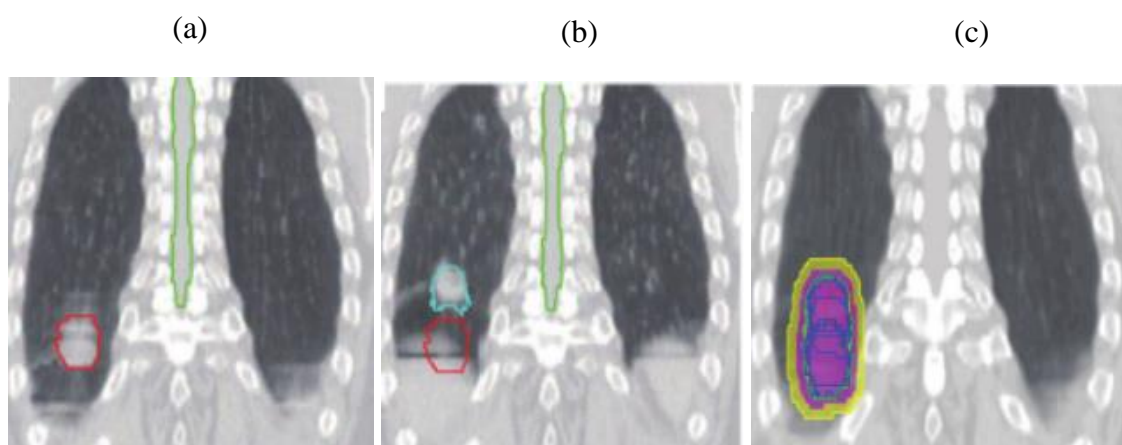


Figure 1–4 The Gross Tumor Volume (GTV) delineated at (a) end-inhalation and, (b) end-exhalation phase of respiration. (c) The green contour depicts Internal Target Volume (ITV) obtained from combining the GTVs, while the Planning Target Volume (PTV) is shown in yellow. Adopted from Glide-Hurst et al¹⁵.

The disadvantage of motion-encompassing methods is that the volume, which is being irradiated, is larger than the actual tumor volume, as it includes significant volume of normal lung tissue. According to results published by Keall et al., when the tumor path length is greater than 5 mm, other motion compensation methods can yield significant normal tissue sparing¹⁶.

1.4.2 Respiratory gating methods

Examining the respiratory cycle, there is a particular portion where the respiratory motion is smaller. Respiratory gating is a motion compensation method in which the radiation beam is on only within that particular portion of the breathing cycle, which is known as the “gate.” The position and width of the gate is not fixed for all patients and is determined using external or internal markers to monitor the patient’s respiratory motion^{17–22}. The disadvantage of a gating method is that the radiation administration is not continuous and gated procedures are longer than non-gated procedures. While the gating results in tumor motion reduction, some motion still occurs within the gate and is called “residual motion.”²³ The gate width is chosen in such a way to minimize the residual motion and maximize the duty cycle.

1.4.3 Breath-hold methods

Breath-hold methods attempt to control the patient’s breathing volume either voluntarily or by using an occlusion valve¹⁶. The application of an occlusion valve allows for a temporary block in the air flow to the patient and thus, immobilize the target. The irradiation is performed during the target immobilization period. Deep inspiration breath-hold (DIBH) is an alternative breath holding technique where the patient adjusts his or her breathing according to a specific respiratory trace^{24–27}. Breath-hold methods require the patients to be trained on how to breathe during the treatment planning CT and the treatment sessions. A reproducible motion control can be achieved by asking the patients to begin with quiet breathing, continue with two breathing periods of slow deep inspiration and expiration and hold the breath at end inhale. Whether an occlusion valve is used or the patients are asked to hold their breath voluntarily, the breath is held for 10 – 20 seconds for every iteration. While breath-hold techniques are effective for tumor motion immobilization, most lung cancer patients suffer from poor pulmonary function and have difficulty with breath-hold procedures.

1.4.4 Real-time tracking methods

An alternative approach for respiratory motion compensation is real-time tumor tracking where the direction of the radiation beam is adjusted dynamically to follow the tumor’s changing position. The implementation of real-time tumor tracking requires using the MLC

or robotic arms to control the radiation beam direction. Alternatively, the tumor can be aligned to the beam using the couch motion. Ideally, continuous real-time tracking results in a 100% duty cycle and the elimination of tumor-motion margin. Ideal real-time tumor tracking involves four requirements: (1) tumor motion/deformation estimation in real-time; (2) tumor motion/deformation prediction to account for system mechanical delays; (3) beam alignment system; and (4) dosimetry adaptation required to account for respiration induced lung volume variations and critical structures motion. The focus of this thesis is the first requirement, which is tumor motion/deformation estimation in real-time. Tumor positioning methods can be divided into two groups of direct and indirect methods.

1.4.4.1 Direct real-time tracking methods

1.4.4.1.1 Direct real-time imaging

The most straight-forward method for finding the tumor position in real-time is real-time imaging²⁸. Currently, the modality of choice for lung real-time imaging is x-ray fluoroscopy. However, x-ray fluoroscopy of most lung tumors does not provide high-contrast images suitable for automatic image segmentation. Therefore, fiducial markers are implanted in or near the tumor to be used as surrogate for tumor motion^{22,29}. Fiducial markers used for real-time imaging are high-Z metal markers which can be readily observed in x-ray images. The possible migration of fiducial markers dictates using three or more fiducial markers instead of one marker. By using multiple markers, the marker migration can be detected by monitoring the distance between markers. While real-time imaging of tumor or implanted fiducial markers results in high accuracy of tumor positioning, the involved additional imaging radiation dose is an issue. To decrease the radiation exposure, hybrid methods have been developed which combine non-continuous imaging episodes with continuous monitoring of respiratory signals which are correlated with tumor motion²⁸⁻³².

1.4.4.1.2 Electromagnetic tumor tracking

An alternative approach for direct tumor tracking is to implant miniature, powered radiofrequency (RF) coils in or near the tumor and track them electromagnetically³³⁻³⁶.

While electromagnetic tracking is a viable alternative to radiographic tracking, it is still invasive and unsafe due to possible risk of pneumothorax or clip migration³⁷.

1.4.4.2 Indirect real-time tracking methods

The second group of real-time tracking methods are indirect tracking methods where an external respiratory signal, e.g. chest motion data, is used to find the tumor motion. To develop a successful indirect real-time tracking method, a strong and robust correlation between external signal and internal organ motion must be established. However, several studies indicate that having strong and stationary correlation between 1D external signals, e.g. spirometry or 1D chest motion data and internal organ motion is not a safe assumption^{30,38-40}.

Several methods have been proposed to address the non-stationary issue in indirect tumor tracking. One solution is to monitor and update the correlation continually during treatment by acquiring images of the tumor position synchronously with the respiratory signal³². This can be accomplished with adaptive filter algorithms, which are designed to predict nonstationary signals by periodically updating the empirical relationship between the input (e.g., breathing) and the output (e.g., tumor position) signals³¹.

An alternative solution to adaptive filtering is to use a multi-dimensional surrogate signal which has been shown to have stronger and more robust correlation with internal organ motion⁴¹. Recent studies indicate that the size of GTV can vary by up to %62⁴². As such, an effective tumor tracking method should be able to estimate the tumor volumetric variations as well as tumor rigid motion.

1.5 The proposed tracking method and theory

A block diagram of the proposed tumor tracking method is shown in Figure 1-5.

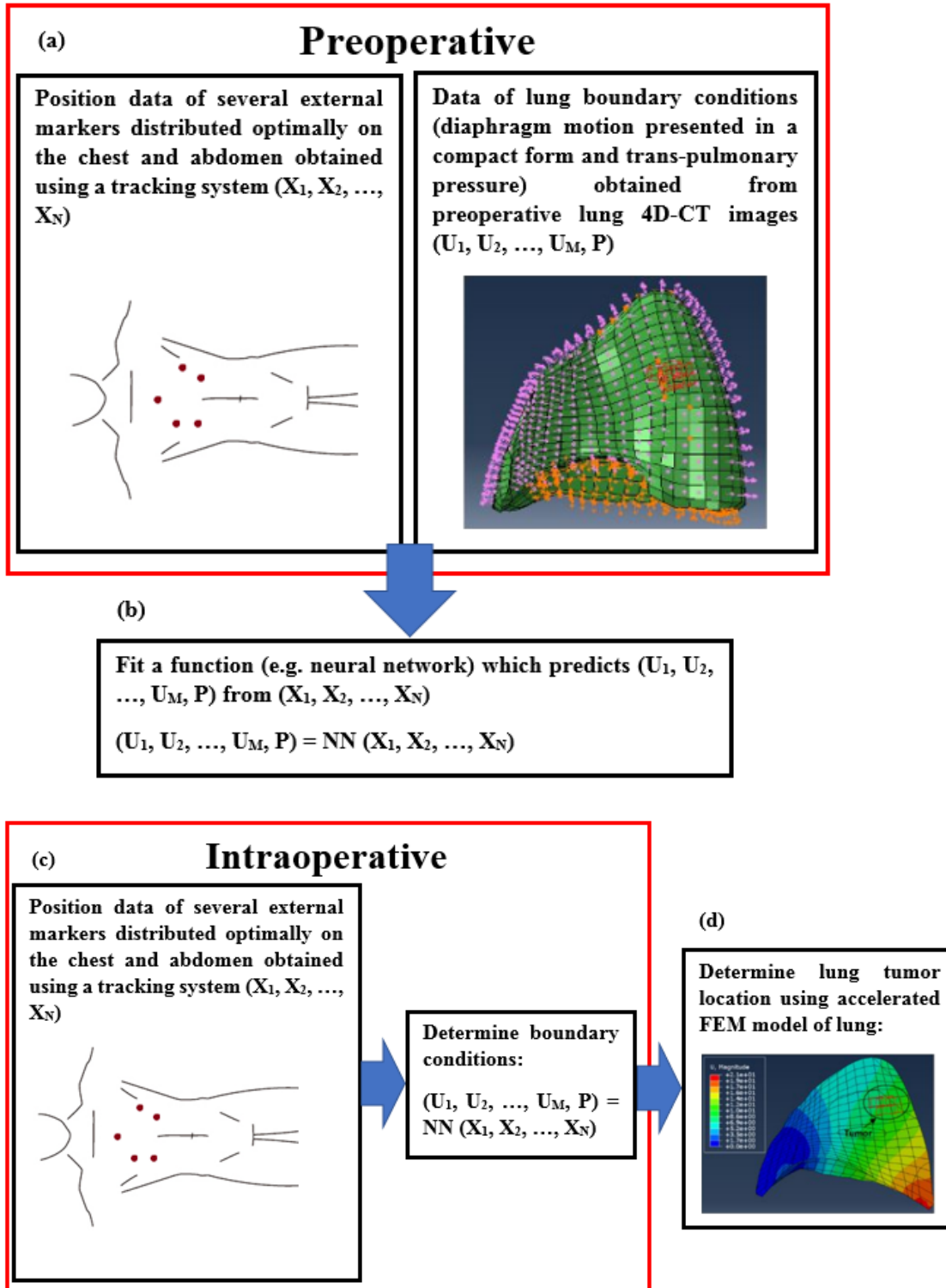


Figure 1–5 A block diagram of lung tumor tracking algorithm which involves a pre-treatment and an intra-treatment step. (a) Pre-treatment tracking of chest surface motion and image based estimation of the lung boundary conditions. The lung BCs include lung-diaphragm contact surface displacements shown in orange

and lung trans-pulmonary pressure shown in purple. (b) Constructing a correlation model (e.g. using neural network (NN) between chest surface motion data and lung boundary conditions. The NN training requires the diaphragm to be presented in a compact form. (c) Chest surface motion tracking during treatment and predicting the boundary conditions in real-time. (d) Calculating lung tumor position and deformation using an accelerated lung biomechanical model.

As shown in Figure 1-5, we use a lung biomechanical model to predict the tumor motion and deformation using the real-time lung boundary conditions (BCs) obtained from the chest motion data. In our proposed lung Finite Element (FE) model, the lung boundary conditions include the diaphragm motion and trans-pulmonary pressure. The latter is the difference between intra-alveolar and intra-pleural pressures and it is calculated through optimization. Many research groups have tackled lung biomechanical modeling⁴³⁻⁵². While existing lung biomechanical models are fairly accurate, most of them cannot be incorporated into our lung tumor tracking algorithm. Apart from Fuerst et al. (2015) which proposed a generative lung biomechanical model, other lung biomechanical models suggest using a contact surface which limits the lung expansion to the segmented chest cavity at end inhale phase. This type of modeling approach limits the real-time application of lung biomechanical modeling as it is difficult to model different breathing patterns, while being computationally expensive. In this study, our main goal is to improve the results published by Fuerst et al. (2015) by incorporating our physiological knowledge about pressure gradients and using more realistic material properties, e.g. incompressibility parameters. Our proposed lung biomechanical model requires the real-time position of the diaphragm and the trans-pulmonary pressure values as boundary conditions. Those BCs are obtained from a Neural Network (NN) which inputs the chest motion data and outputs the lung boundary conditions.

In contrast to indirect heuristic mathematical methods of lung tumor motion prediction which rely solely on data fitting to a mathematical model⁵³, the proposed method is a hybrid method of heuristic data fitting in conjunction with tissue deformation, physics based model. The first component of data fitting model is an NN used to predict the lung BCs from input chest surface motion data. To ensure robustness of this NN, an optimal number of markers leading to the highest correlation between chest surface motion data and tumor motion can be determined and used instead of a single marker. The second component is

the lung biomechanical model which inputs the BCs obtained from the NN to output the tumor position and geometry. This hybrid approach is believed to be more effective than using a solely heuristic model (e.g. NN) to calculate tumor position and geometry directly from the chest wall surface motion data. The reason is that the NN in the latter scenario is expected to be highly complex while being prone to data overfitting. Using an accurate lung biomechanical model in the proposed system has two advantages: 1) accuracy of tumor motion tracking will be high and 2) tumor geometry variations during respiration can be taken into account, paving the way for more accurate radiation dose distribution calculation. The novelties of this tumor tracking algorithm are: 1) developing a lung biomechanical model which is designed specifically for radiotherapy, 2) effective usage of PCA for diaphragm motion modeling by taking advantage of Transfinite Interpolation method for consistent landmark selection, 3) Proposing a machine learning approach for updating the lung boundary conditions in real-time required for the biomechanics-based tumor motion/deformation estimation. The next six sections address the theoretical background required for developing the proposed tumor tracking algorithm.

1.6 Connected component labeling⁵⁴

In connected component labeling, the concept of pixel connectivity is used to group image pixels into components. In fact, a connected component is a group of pixels which are connected in some way and share similar pixel intensity values. Pixel connectivity defines the way pixels in a 2D image (or voxels in a 3D image) are connected. In 2D, there are 3 types of connectivity, including 4-connectivity, 6-connectivity, and 8-connectivity. Here, we assume binary input image and 8- connectivity. The 8-connectivity means that for a specific pixel, all its neighbors that touch one of its edges or corners are connected to that pixel. For a pixel at (x, y) , its 8-connected pixels are $(x \pm 1, y)$, $(x, y \pm 1)$, and $(x \pm 1, y \pm 1)$.

To convert a binary image into labeled connected components, the entire image is scanned, pixel-by-pixel (from top to bottom and left to right) to identify connected pixel regions. The labeling operator scans the binary image and for each non-zero pixel p , examines its

four neighbors which have already been encountered in the scan (i.e. $(x - 1, y)$, $(x - 1, y - 1)$, $(x, y - 1)$, and $(x + 1, y - 1)$). If all four neighbors are 0, a new label is assigned to p . If only one neighbor is non-zero and has been labeled, its label is assigned to p . If more than one of the neighbors has already been labeled, one of the labels is assigned to the p and the equivalences are noted down. Once the first image scan is complete, the equivalent label pairs are classified into equivalence classes and each class is assigned a unique label. Finally, the image is scanned for the second time to assign the class labels to the connected components. For display purpose, the labels might be different gray levels or colors. Figure 1-6 (a) depicts an example of a binary image which includes three connected components. The application of connected component labeling algorithm on Figure 1-6 (a) is shown in Figure 1-6 (b).

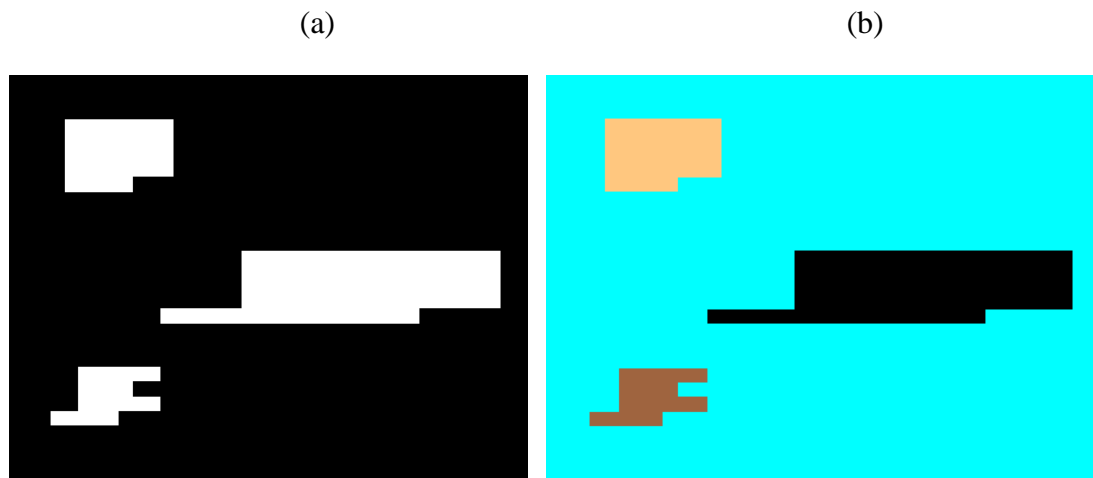


Figure 1-6 (a) An example of a binary image including three connected components. (b) The labeled connected components.

1.7 Simple Region Growing (SRG) Algorithm

Region growing⁵⁵ is a simple region-based image segmentation method which is initialized with selecting some seed points from the region of interest. The seed point selection is then followed by examining the neighboring pixels to determine if they should be added to the region. The initial seeds required for beginning the segmentation process can be selected manually or automatically, while each seed can be a single pixel or a group of pixels. Here,

we assume the number of initial seeds is N which are stored in N sets of S_1, S_2, \dots and S_N . Let A contain all pixels which are adjacent to at least one of the pixels in the seed sets, S_i 's:

$$A = \{x \notin \bigcup_{i=1}^N S_i \mid nbr(x) \cap \bigcup_{i=1}^N S_i \neq \emptyset\} \quad (1 - 1)$$

Where $nbr(x)$ is the set of all immediate neighbors of x . At each step during the segmentation process, one pixel from A is selected and examined based on a homogeneity criterion to decide if it should be added to one of its neighboring regions, i.e. S_i 's. To do so, first the pixel's neighboring regions are identified. S_i is a neighboring region of x if $nbr(x) \cap S_i \neq \emptyset$. Next, the homogeneity criterion is tested on the pixel. In Adams and Bischof⁵⁵, the criterion is to choose a pixel whose grey-value is closest to the average gray-value of one of its neighboring growing regions. This criterion ensures that each segmented region is as homogeneous as possible. If the examined pixel passes the homogeneity criterion, it is added to its neighboring region while A and corresponding neighboring region are updated. This process continues until all the pixels in the image are allocated to one and only one of the growing regions.

1.8 Circle Hough transform

The Hough transform is a feature extraction technique suitable for features of a particular shape which can be specified in some parametric form. The feature detection is based on a voting procedure which finds the local maxima in a so-called accumulator space in which the objects are represented in their parametric form.

Lines and circles are two groups of objects which can be identified in an image using the Hough transform. For instance, a circle with radius R and center (a, b) can be described with the parametric equations:

$$(x - a)^2 + (y - b)^2 = R^2 \quad (1 - 2)$$

The Hough transform begins by creating an accumulator array with the same size as the number of unknown parameters, i.e., three, in the case of circles. The 3D parameter space

is hard to implement, as such, the circular Hough transform is usually performed with fixed parameter R , making the parameter space 2D. Imagine the R parameter is fixed, i.e. we know the radius of circle we would like to find in the image. According to (1-2), for each non-zero pixel (x, y) in the original image, its representation in the parametric space is a circle with center (x, y) . The intersection point of all such circles in the parametric (accumulator) space corresponds to the center of original circle. To find the intersection point, we use the accumulator array which keeps track of the number of times the circles pass through each point in the parametric space. The local maxima point, i.e. the intersection of circles in the Figure 1-7 (b) is the center of circle shown in Figure 1-7 (a). We can find multiple circles with the same radius by looking for all local maxima in the parametric space. In the case of unknown circle radius, we can iterate through possible radii, using the same technique described for fixed R . In this case, the parametric space is 3D and the circle can be found by finding the local maxima in the 3D accumulator array.

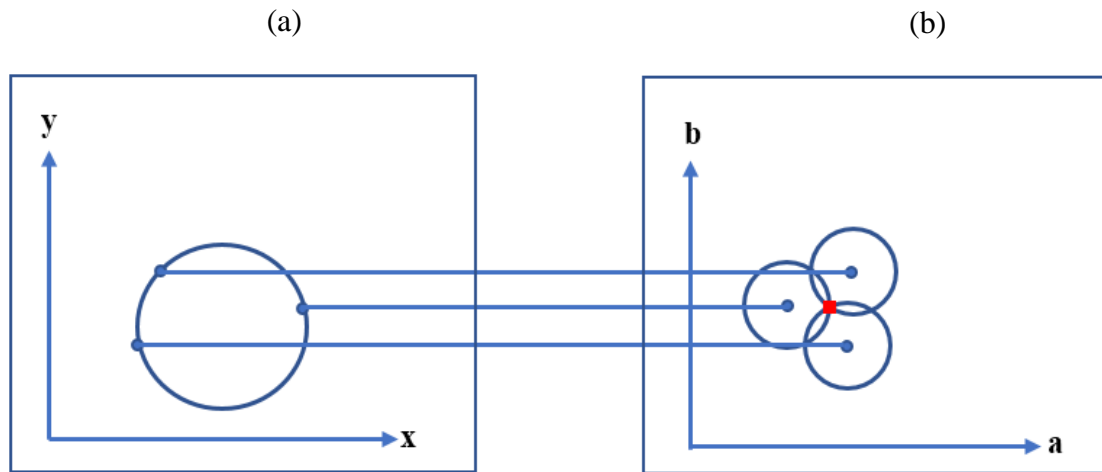


Figure 1-7 (a) An image of the original circle. (b) The parametric representation of the original circle. The local maxima point, i.e. the intersection of circles is the center of original circle.

1.9 The Theory of Elasticity

1.9.1 Finite Elasticity

The theory of elasticity deals with the elastic materials and their deformation. More specifically, it describes the material's mechanical behavior and its deformation in the presence of external force. In general, the deformation of an elastic object geometry can be represented with the schematic shown in Figure 1-8, where t_0 and t denote the undeformed and deformed states, respectively.

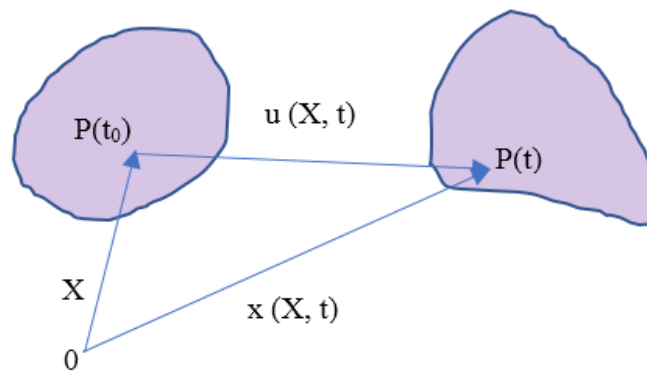


Figure 1-8 A general elastic object at undeformed (time t_0) and deformed (time t) states.

As shown in this figure, each point $P(t_0)$ at position \mathbf{X} inside the undeformed geometry, is relocated by deformation field $\mathbf{u}(\mathbf{X}, t)$ to its new position $\mathbf{x}(\mathbf{X}, t)$ and its new coordinates is denoted by $P(t)$. As such

$$\mathbf{x}(\mathbf{X}, t) = \mathbf{X} + \mathbf{u}(\mathbf{X}, t) \quad (1 - 3)$$

Applying the differential calculus principles on Equation (1-3) we can write

$$d\mathbf{x} = d\mathbf{X} + (\nabla\mathbf{u})d\mathbf{x} \quad (1 - 4)$$

Where the displacement gradient $\nabla \mathbf{u}$ is defined as

$$\nabla \mathbf{u} = \begin{pmatrix} \frac{\partial u_1}{\partial X_1} & \frac{\partial u_1}{\partial X_2} & \frac{\partial u_1}{\partial X_3} \\ \frac{\partial u_2}{\partial X_1} & \frac{\partial u_2}{\partial X_2} & \frac{\partial u_2}{\partial X_3} \\ \frac{\partial u_3}{\partial X_1} & \frac{\partial u_3}{\partial X_2} & \frac{\partial u_3}{\partial X_3} \end{pmatrix} \quad (1-5)$$

Using the tensor notation, Equation (1-3) can be written as

$$d\mathbf{x} = \mathbf{F}d\mathbf{X} \quad (1-6)$$

In Equation (1-6), \mathbf{F} denotes the deformation gradient tensor. Using Equation (1-4), \mathbf{F} is defined as:

$$\mathbf{F} = \mathbf{I} + \nabla \mathbf{u} \quad (1-7)$$

where \mathbf{I} is the identity tensor. To calculate the strain tensor, the relationship between the length of $d\mathbf{x}$ and $d\mathbf{X}$ is calculated using the dot product of Equation (1-6):

$$ds^2 = d\mathbf{x} \cdot d\mathbf{x} = d\mathbf{X} \cdot \mathbf{C}d\mathbf{X} \quad (1-8)$$

where ds is the length of $d\mathbf{x}$. In Equation (1-6), \mathbf{C} is the right Cauchy-Green deformation tensor and it can be written as:

$$\mathbf{C} = \mathbf{F}^T \mathbf{F} \quad (1-9)$$

Equation (1-8) indicates that when $\mathbf{C}=\mathbf{I}$, the length of $d\mathbf{x}$ and $d\mathbf{X}$ is the same, implying that the object has gone only through rigid body motion. The right Cauchy-Green deformation tensor can be expressed in terms of displacement gradient using Equation (1-7) and the tensor calculus principles:

$$\mathbf{C} = \mathbf{I} + \nabla \mathbf{u} + (\nabla \mathbf{u})^T + (\nabla \mathbf{u})^T (\nabla \mathbf{u}) \quad (1-10)$$

If the tensor \mathbf{E} is defined as

$$\mathbf{E} = \frac{1}{2} [\nabla \mathbf{u} + (\nabla \mathbf{u})^T + (\nabla \mathbf{u})^T (\nabla \mathbf{u})] \quad (1 - 11)$$

The right Cauchy-Green deformation tensor can be summarized as:

$$\mathbf{C} = \mathbf{I} + 2\mathbf{E} \quad (1 - 12)$$

In Equations (1-11) and (1-12), \mathbf{E} is the Green-Lagrange strain tensor, and its relation to deformation gradient tensor, \mathbf{F} , is obtained using Equations (1-9) and (1-11) :

$$\mathbf{E} = \frac{1}{2} [\mathbf{F}^T \mathbf{F} - \mathbf{I}] \quad (1 - 13)$$

1.9.2 Infinitesimal versus finite (large) deformation

Depending on whether the material is going through small or large deformations, Equation (1-11) can be used differently. When the deformation and consequently its partial derivatives are very small, the components of $(\nabla \mathbf{u})^T (\nabla \mathbf{u})$ are infinitesimal and in the Cartesian coordinates system, \mathbf{E} can be reduced to:

$$\mathbf{E} = \frac{1}{2} [\nabla \mathbf{u} + (\nabla \mathbf{u})^T] \quad (1 - 14)$$

$$\varepsilon_{ij} = \frac{1}{2} \left(\frac{\partial u_i}{\partial X_j} + \frac{\partial u_j}{\partial X_i} \right), i, j = 1, 2, 3 \quad (1 - 15)$$

In case of large deformations, Equation (1-11) cannot be simplified. In this research project, we used a finite element solver called ABAQUS. It is noteworthy that ABAQUS by default uses Equation (1-15) for strain. When the deformations are large, the geometric-nonlinearity option must be set on in ABAQUS to use the Green- Lagrange strain tensor \mathbf{E} .

1.9.3 Stress Tensor and Principle of Linear Momentum

In this section, we first introduce the components of Cauchy stress and then derive the differential equations of motion for an infinitesimal volume of the continuum material

undergoing deformation. Figure 1-9 depicts a very small cubic particle within the elastic material. In this Figure, $e_j, j = 1, 2, 3$ are the unit vectors defined normal to the faces of the cube and \mathbf{t} denotes the internal traction vector defined as:

$$\mathbf{t} = \frac{d\mathbf{F}}{dA} \quad (1 - 16)$$

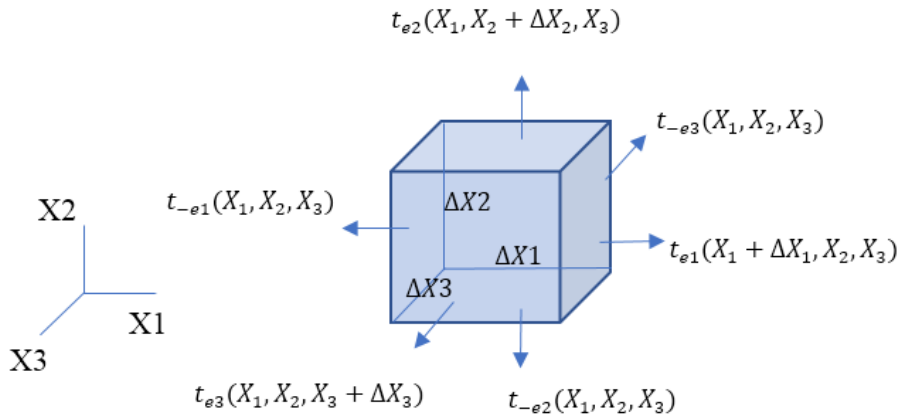


Figure 1-9 A very small cubic particle within the elastic material.

where $d\mathbf{F}$ is the force applied to the differential area dA . The relationship between the components of Cauchy stress (true stress) and the tractions vectors, t_{ei} s is given by:

$$\begin{cases} t_{e1} = \sigma_{11}e_1 + \sigma_{12}e_2 + \sigma_{13}e_3 \\ t_{e2} = \sigma_{21}e_1 + \sigma_{22}e_2 + \sigma_{23}e_3 \\ t_{e3} = \sigma_{31}e_1 + \sigma_{32}e_2 + \sigma_{33}e_3 \end{cases} \quad (1 - 17)$$

The Newton's law of motion should be satisfied for the small volume of continuum. Using the Cartesian coordinates systems for the cubic volume and assuming that $\Delta x_i \rightarrow 0$, we can write:

$$\frac{\partial t_{e1}}{\partial x_1} + \frac{\partial t_{e2}}{\partial x_2} + \frac{\partial t_{e3}}{\partial x_3} + \rho \mathbf{B} = \rho \mathbf{a} \quad (1 - 18)$$

where \mathbf{B} is the body force per unit mass through the continuum, ρ is the mass density at position \mathbf{x}_i representing the cube, and \mathbf{a} is the acceleration vector at point \mathbf{x}_i . Using (1-17), this equilibrium equation can be written in terms of Cauchy stress tensor components as:

$$\frac{\partial \sigma_{ij}}{\partial x_j} + \rho B_i = \rho a_i \quad i, j = 1, 2, 3 \quad (1 - 19)$$

The equivalent form of Equation (1-19) in tensor format is:

$$\text{div} \boldsymbol{\sigma} + \rho \mathbf{B} = \rho \mathbf{a} \quad (1 - 20)$$

The deformation of a continuum body is described with this last relationship which is the well-known Cauchy's equation of motion.

1.9.4 Linear Elastic Material

The five fundamental principles of continuum physics, including the principle of conservation of mass, the principle of linear momentum, the principle of angular momentum, the principle of conservation of energy, and the entropy inequality, are used to describe the mechanical response of an elastic material which undergoes specific loading and boundary conditions. In addition to continuum physics principles, the material's intrinsic mechanical properties such as its stiffness, compressibility, and its active response are required for determining the material's deformation. In continuum mechanics, the material's intrinsic mechanical behavior is described using the *constitutive law* which describes the relationship between stresses and strains generated in the continuum body. The relationship between the stress and strain may be linear or nonlinear. In the linear case, which is the simplest material model, the constitutive law is the *Hooke's law*:

$$\sigma_{ij} = C_{ijkl} \varepsilon_{kl} \quad (1 - 21)$$

where σ_{ij} are the Cauchy stresses, ε_{kl} are the infinitesimal strain tensor components introduced in Equation (1-15) and C_{ijkl} are the components of the *elasticity tensor*, which is a fourth-order tensor with 81 coefficients. The *elasticity tensor* can be reduced to 21 independent coefficients by applying the continuum mechanics principles and symmetry. The Hooke's law can be simplified for an *isotropic linear elastic material* as:

$$\sigma_{ij} = \lambda \varepsilon_{kk} \delta_{ij} + 2\mu \varepsilon_{ij} \quad (1 - 22)$$

where λ and μ are *Lame's constants* and δ_{ij} is Kronecker delta. The equivalent form of Equation (1-22) in tensor form is:

$$\boldsymbol{\sigma} = \lambda \varepsilon_{kk} \mathbf{I} + 2\mu \boldsymbol{\varepsilon} \quad (1 - 23)$$

Lame's constants can be written in terms of *Poisson's ratio* and Young's Modulus as:

$$\lambda = \frac{\nu E}{(1 + \nu)(1 - 2\nu)}, \quad \mu = \frac{E}{2(1 + \nu)} \quad (1 - 24)$$

The mechanical response of an isotropic linear elastic material, under specific loading conditions can be described using Equations (1-23) and (1-20).

1.9.5 Hyper-elastic material

The material's mechanical response can be non-linear. Such non-linearity might be an intrinsic characteristic of the material or a response to large (strain over 5%) deformations that redistributes the internal forces within the material. The latter is called geometric nonlinearity and can be expressed by linear elastic materials too. Hyper-elasticity is used to describe materials that express both types of nonlinearity.

Theoretically, a hyperelastic material is defined based on this postulation that the strain energy per unit volume of the material's reference geometry can be defined using a *Helmholtz free-energy function* such as U . For cases where U solely depends on the

deformation gradient tensor, \mathbf{F} , or other strain tensors, or strain scalar invariants, it is called *the strain energy function* denoted as $U(\mathbf{F})$.

The material's mechanical behavior is characterized by the strain energy function. The Cauchy stress tensor (true stress) can be derived based on the strain energy function for a homogenous hyperelastic material as:

$$\boldsymbol{\sigma} = J^{-1} \mathbf{F} \frac{dU(\mathbf{F})}{d\mathbf{F}} \quad (1 - 25)$$

where J is the volume ratio which can be written in terms of the deformation gradient tensor as:

$$J = \det(\mathbf{F}) \quad (1 - 26)$$

For an incompressible material, the relation (1-26) can be written as:

$$\boldsymbol{\sigma} = -p\mathbf{I} + \mathbf{F} \frac{dU(\mathbf{F})}{d\mathbf{F}}, \quad \det(\mathbf{F}) = 1 \quad (1 - 27)$$

where p is an indeterminate Lagrange multiplier which can be characterized as a hydrostatic pressure. It is noteworthy that p can be determined based on the equilibrium equations and boundary conditions defined for the hyper-elastic material. For isotropic hyperelastic material, the following constitutive law can be derived based on the strain energy function⁵⁶:

$$\boldsymbol{\sigma} = 2J^{-1} \left[I_3 \frac{\partial U}{\partial I_3} \mathbf{I} + \left(\frac{\partial U}{\partial I_1} + I_1 \frac{\partial U}{\partial I_2} \right) \mathbf{B} - \frac{\partial U}{\partial I_2} \mathbf{B}^2 \right] \quad (1 - 28)$$

Equation (1-28) is considered as the basis for defining constitutive laws for different hyper-elastic behaviors. In this equation, U is a function of scalar invariants, i.e. I_1 , I_2 , and I_3 , which are defined as:

$$I_1 = \text{tr}(\mathbf{B}) = \lambda_1^2 + \lambda_2^2 + \lambda_3^2 \quad (1 - 29 - a)$$

$$I_2 = \frac{1}{2} \left[(\text{tr}(\mathbf{B}))^2 - \text{tr}(\mathbf{B}^2) \right] = \lambda_1^2 \lambda_2^2 + \lambda_1^2 \lambda_3^2 + \lambda_2^2 \lambda_3^2 \quad (1 - 29 - b)$$

$$I_3 = \det(\mathbf{B}) = J^2 = \lambda_1^2 \lambda_2^2 \lambda_3^2 \quad (1 - 29 - c)$$

where λ_1 , λ_2 , and λ_3 are the principle stretches and \mathbf{B} is the left Cauchy-Green deformation tensor defined as:

$$\mathbf{B} = \mathbf{F}\mathbf{F}^T \quad (1 - 30)$$

Equation (1-28) can be used for derivation of constitutive law of isotropic hyper-elastic materials provided that the strain energy function is known.

1.10 Principal Component Analysis

Principal component analysis (PCA) is a well-known technique for dimensionality reduction, where only strong patterns in the data sets are maintained^{57,58}. The dimensionality reduction is performed through finding a reduced linear subspace which maintains most of the variability of the data. For a given set of data on n dimensions, the reduced linear subspace is a new coordinate system, formed by d orthogonal vectors which are linear transformations of the original data points, i.e. $d \leq n$.

According to Hotelling's definition of PCA⁵⁸, the principal components of data vectors $x_i, i \in 1 \dots t$, are the d orthogonal vectors which maintain the maximal data variance when the data is projected to those vectors. Let U_1 be the first principal component having the maximum variance expressed by $x_i, i \in 1 \dots t$. Given an $n \times t$ matrix X , which has t

columns of n -dimensional centered observations, the first principal component, U_1 , can be expressed as a linear combination of X :

$$U_1 = w^T X \quad (1 - 31)$$

where $w = [w_1 \dots w_n]$ is the weight vector. As such, the variance of U_1 is given by:

$$\text{var}(U_1) = \text{var}(w^T X) = w^T S w \quad (1 - 32)$$

where S is the covariance matrix of X . To find the proper w which maximizes $\text{var}(U_1)$, we choose w to maximize $w^T S w$ under the condition that it has a unit length:

$$\max w^T S w \quad (1 - 33)$$

$$\text{subject to } w^T w = 1$$

The optimization problem is solved using a Lagrange multiplier α_1 :

$$L(w, \alpha) = w^T S w - \alpha_1 (w^T w - 1) \quad (1 - 34)$$

Differentiating with respect to w gives n equations,

$$S w = \alpha_1 w \quad (1 - 35)$$

By pre-multiplying both sides by w^T we have:

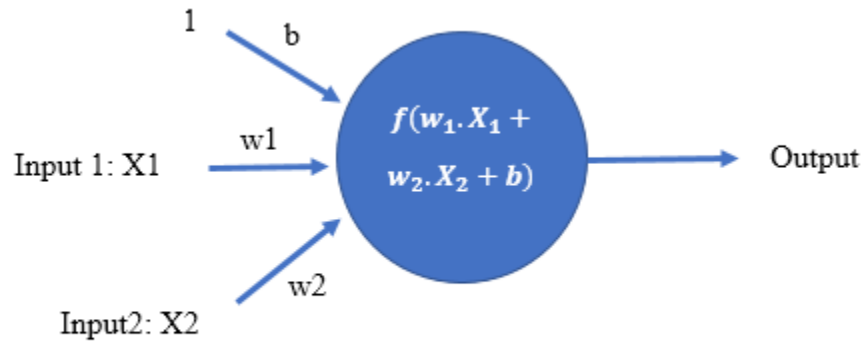
$$w^T S w = \alpha_1 w^T w = \alpha_1 \quad (1 - 36)$$

The last equation clearly indicates that α_1 and w are an eigenvalue and eigenvector of S and $\text{var}(U_1)$ is maximized only if α_1 is the largest eigenvalue of S . As such, the reduced linear subset which maintains the maximum variance expressed by data is formed by d dominant eigenvectors of S , the covariance matrix of X .

1.11 Neural Networks^{59,60}

Artificial Neural Networks (ANNs) are mathematical models mimicking the way the human brain processes the information. The basic component in an ANN is the neuron. Each neuron has inputs, on which it applies a function to compute an output. Depending on where the neuron is in the ANN, the inputs come from other neurons or from an external

source. Each input has a weight (w) which describes its relative importance compared to other inputs. The neuron calculates the output by applying a function f on the weighted sum of its inputs. Figure 1-10 depicts an example of a neuron.



$$\text{output of neuron} = Y = f(w_1 \cdot X_1 + w_2 \cdot X_2 + b)$$

Figure 1–10 A single neuron

As shown in Figure 1-10, the neuron applies the activation function f on the weighted sum of its inputs, X_1 and X_2 and outputs the result. The neuron shown in this figure has a bias input, b , in addition to its actual inputs. The main function of this bias is for shifting the activation function which may be necessary for successful training. To be a good representative for real world applications, the activation function is usually a non-linear function. Some examples of activation functions are Sigmoid, tanh, and ReLU functions shown in Figure 1-11. The Sigmoid functions is described as:

$$\sigma(x) = \frac{1}{(1 + e^{-x})} \quad (1 - 37)$$

As such, the output of Sigmoid is between 0 and 1. The tanh function takes a real-valued input and squashes it to the range $[-1, 1]$. This function can be written as:

$$\tanh(x) = 2\sigma(2x) - 1 \quad (1 - 38)$$

The ReLU stands for Rectified Linear Unit and is defined as:

$$f(x) = \max(0, x) \quad (1 - 39)$$

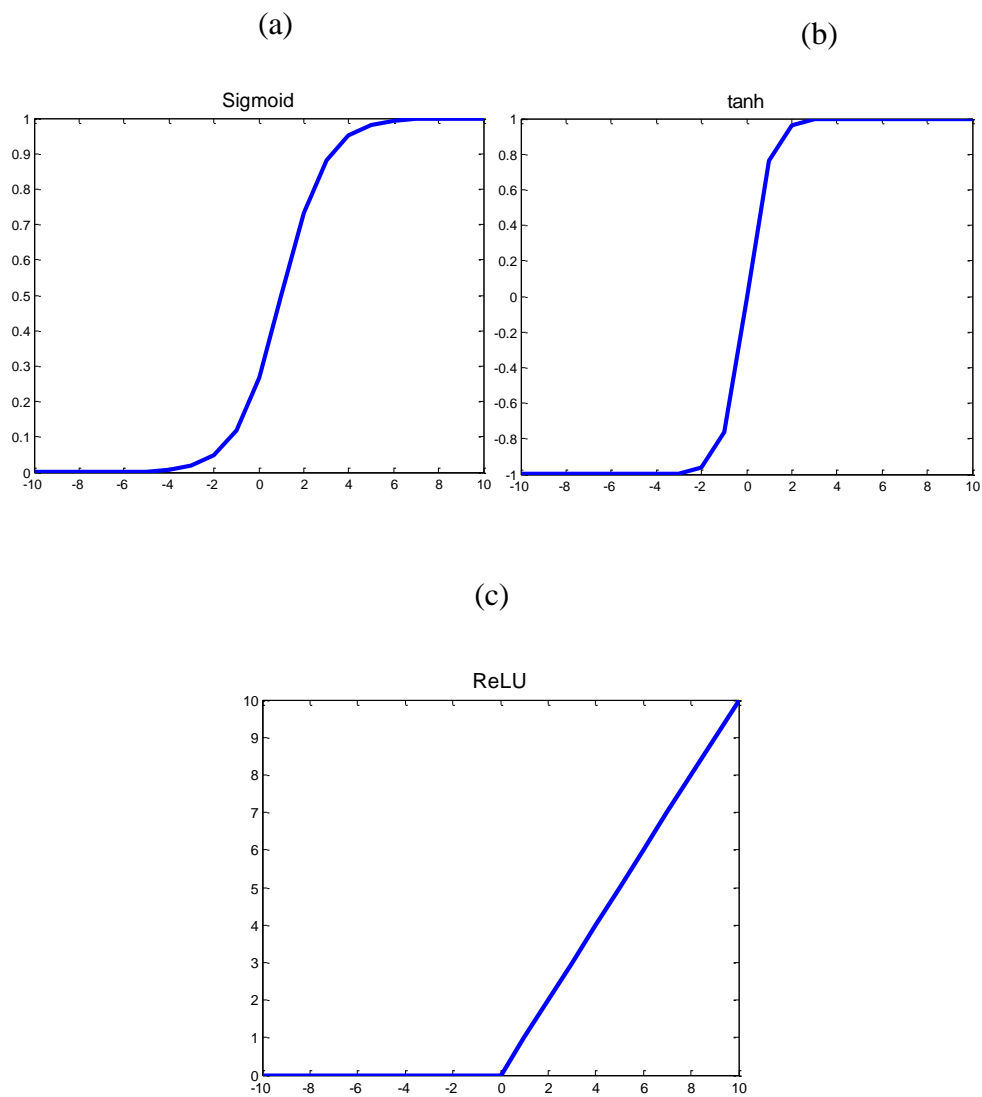


Figure 1–11 The most common neuron activation functions. (a) Sigmoid, (b) tanh, (c) ReLU.

1.11.1 Feedforward neural network

The first and simplest ANN is the feedforward network which has multiple layers, each containing multiple neurons. Figure 1-12 depicts an example of feedforward network. As shown in this figure, nodes from adjacent layers have connections between them.

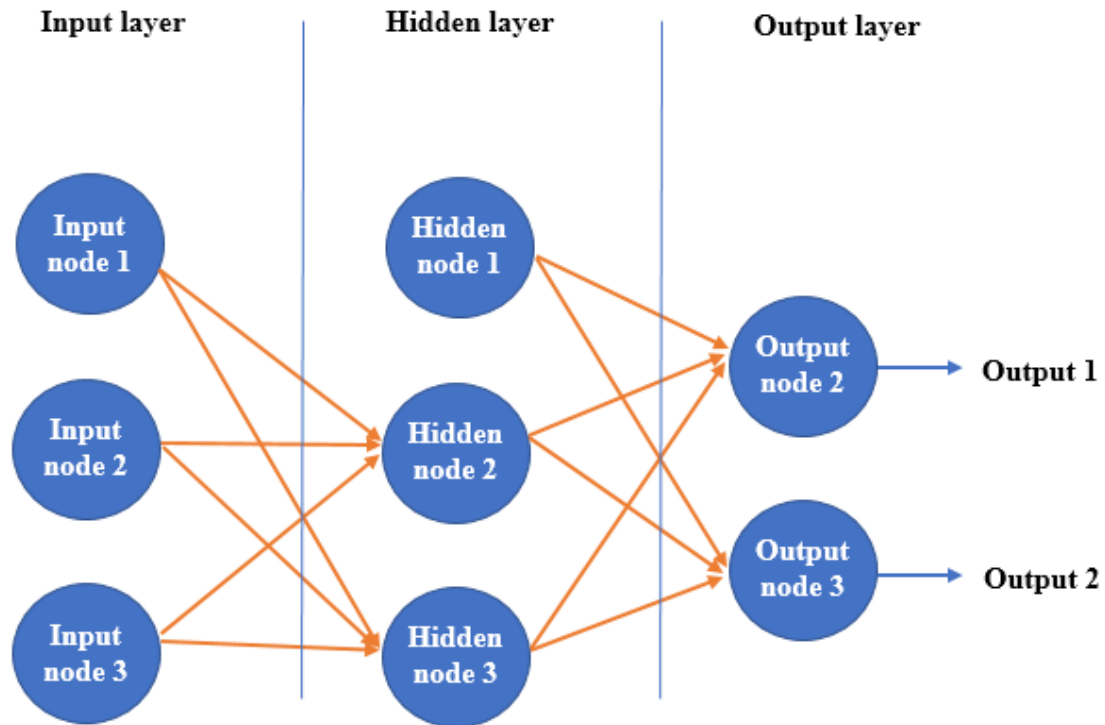


Figure 1–12 An example of feedforward neural network.

Three groups of nodes form the feedforward neural network. The input nodes pass the information from the outside source to the network. These nodes do not perform any computation on the input data. The hidden layer, which is named hidden as it does not have direct connection with the outside world, performs computations on the input data and transfer them to the output layer. A feedforward network can have multiple hidden layers. Similar to the hidden layer, the output layer is responsible for computations. The output layer transfers information from the network to the outside world. In the feedforward network, the information moves only forward, from the input nodes, through the hidden

layer, to the output layer. Single-layer perceptron is the simplest feedforward network which lacks the hidden layer while a Multi-Layer Perceptron (MLP) has one or more hidden layers. The advantage of MLP over a single layer perceptron is that MLP can learn non-linear functions while a single layer perceptron can only learn linear functions.

1.11.2 Training MLP: The Back-Propagation Algorithm

The Multi-Layer Perceptron is trained using a method called the Backpropagation algorithm. This training algorithm uses the gradient descent method to find the network weights which minimize the squared error function. For a sample output neuron, the squared error function is:

$$E = \frac{1}{2}(t - y)^2 \quad (1 - 40)$$

where E is the squared error between t , target output, and y , actual output of the neuron. The coefficient $\frac{1}{2}$ is meant to cancel the exponent when differentiating. The Backpropagation algorithm requires using an arbitrary learning rate which is multiplied to the error. As such, using a constant coefficient does not change the outcome. The output of each neuron j , is defined as:

$$o_j = f(net_j) = f\left(\sum_{k=1}^n w_{kj}o_k\right) \quad (1 - 41)$$

where net_j is the weighted sum of the inputs to the neuron j , n is the number of inputs, w_{ij} is the weight between neurons i and j , and f is the activation function. The inputs to neuron j can be outputs o_k of previous neurons, or if j is in the first layer, the inputs x_k to the network. In general, the activation function f is nonlinear and differentiable. A commonly used activation function is the Sigmoid function described earlier in (1-37), which has a derivative of:

$$\frac{df}{dz}(z) = f(z)(1 - f(z)) \quad (1 - 42)$$

The partial derivative of the error with respect to weight w_{ij} is obtained using the chain rule twice:

$$\frac{\partial E}{\partial w_{ij}} = \frac{\partial E}{\partial o_j} \frac{\partial o_j}{\partial net_j} \frac{\partial net_j}{\partial w_{ij}} \quad (1 - 43)$$

For the third factor in Eq. (1-43), only one term in the sum net_j depends on w_{ij} , so that:

$$\frac{\partial net_j}{\partial w_{ij}} = \frac{\partial}{\partial w_{ij}} \left(\sum_{k=1}^n w_{kj} o_k \right) = o_i \quad (1 - 44)$$

For a neuron in the first hidden layer, o_i is just x_i . To explain why backpropagation requires the activation function to be differentiable, note that the second factor in Eq. (1-43) is the derivative of the output of neuron j with respect to its input which is simply the partial derivative of the activation function f . For Sigmoid function:

$$\frac{\partial o_j}{\partial net_j} = \frac{\partial}{\partial net_j} f(net_j) = f(net_j) (1 - f(net_j)) \quad (1 - 45)$$

The first factor in Eq. (1-43) is straight forward to calculate for the output layer as $o_j = y$ and

$$\frac{\partial}{\partial y} \frac{1}{2} (t - y)^2 = (y - t) \quad (1 - 46)$$

In the case of j being an arbitrary inner layer of the network, finding the derivative E with respect to o_j is less straight forward. To calculate the first factor, E is considered to be a function of the inputs of all neurons $L = u, v, \dots, w$ receiving input from neuron j ,

$$\frac{\partial E(o_j)}{\partial o_j} = \frac{\partial E(net_u, net_v, \dots, net_w)}{\partial o_j} \quad (1 - 47)$$

Now, a recursive expression for $\frac{\partial E(o_j)}{\partial o_j}$ can be obtained by taking the total derivative with respect to o_j :

$$\frac{\partial E}{\partial o_j} = \sum_{l \in L} \left(\frac{\partial E}{\partial net_l} \frac{\partial net_l}{\partial o_j} \right) = \sum_{l \in L} \left(\frac{\partial E}{\partial o_l} \frac{\partial o_l}{\partial net_l} w_{jl} \right) \quad (1 - 48)$$

As such, by having the outputs o_l of the layers which are closer to the output layer, the derivative with respect to o_j can be calculated. This gives a recursive method for calculating the derivative of error with respect to all neurons.

To summarize:

$$\frac{\partial E}{\partial w_{ij}} = \delta_j o_i \quad (1 - 49)$$

with

$$\delta_j = \frac{\partial E}{\partial o_j} \frac{\partial o_j}{\partial net_j} = \begin{cases} (o_j - t_j) o_j (1 - o_j) & \text{if } j \text{ is an output neuron,} \\ \left(\sum_{l \in L} \delta_l w_{jl} \right) o_j (1 - o_j) & \text{if } j \text{ is an inner neuron.} \end{cases}$$

To update the weight w_{ij} , the gradient is multiplied with a learning rate, α , and -1, to calculate the change in weight, Δw_{ij} . The change in weight is then added to the old weight to calculate the new weight:

$$\begin{aligned} \Delta w_{ij} &= -\alpha \frac{\partial E}{\partial w_{ij}} \\ &= \begin{cases} -\alpha o_i(o_j - t_j)o_j(1 - o_j) & \text{if } j \text{ is an output neuron,} \\ -\alpha o_i \left(\sum_{l \in L} \delta_l w_{jl} \right) o_j(1 - o_j) & \text{if } j \text{ is an inner neuron.} \end{cases} \end{aligned} \quad (1 - 50)$$

Note that the negative sign determines the direction of a minimum, not a maximum, of the error function.

1.12 Research Objectives

Hypothesis: A tumor motion tracking system developed based on the lung biomechanical model incorporated into a radiation therapy system can be used to improve lung cancer treatment outcome.

The goal of this thesis is to develop a biomechanics-based real-time tumor tracking algorithm. More specifically, the focus of this thesis is on algorithm development and providing a proof of principle for the feasibility of using a biomechanics-based tumor tracking approach. There are two challenges associated with using biomechanical modeling for real-time tumor tracking. The first challenge is how to update the lung boundary conditions in real-time and the second challenge is associated with FEA speed. This thesis addresses the first challenge. The second challenge can be addressed using GPU programming and model reduction methods which is not within the scope of this thesis. As such, the goal of this thesis is to develop and test a pipeline for tracking lung tumors using the biomechanical modeling approach. The breakdown of the research objectives to achieve this goal is formulated as:

- 1) To develop automatic image segmentation methods for deriving the required information for biomechanical modeling.
- 2) To develop an accurate lung biomechanical model designed specifically for tumor tracking.
- 3) To develop a compact form mathematical model of diaphragm motion required for updating the lung biomechanical model in real-time.

- 4) To develop functions (e.g. Neural Network-based functions) for estimating the lung boundary conditions from chest motion data.

The reader may notice that different number of subjects are used in each study, and in some studies the number of patients is small. First, all these research projects are proof of principle studies rather than being comprehensive clinical studies. While the number of patients used in these studies is sufficient for our goal, further studies should be conducted to assess the algorithm performance on larger data sets. Also, the main reason for having small and different subject numbers is that in each study, we used different criteria to select the patients. For instance, for diaphragm segmentation we needed subjects with CT images covering the entire diaphragm. In the second study, which was on lung biomechanical modeling, we selected subjects with a tumor in the right lung to avoid complications caused by the heart motion. Also, the results of the second study are extremely sensitive to having image artifacts close to the diaphragm. As such, we had to exclude those cases too. In the third study, which was on diaphragm motion modeling, we picked subjects with minimum image artifact close to the diaphragm. Finally, the fourth study uses the same subjects used in the second study plus two more subjects used for assessing the algorithm performance for inter-fraction motion variation prediction.

1.13 Thesis Roadmap

1.13.1 *Chapter 2 - Anatomy-based algorithm for automatic segmentation of the human diaphragm in non-contrast CT images*

A fully automatic algorithm was developed in ITK for segmentation of the full human diaphragm required for biomechanical modeling. ITK is an open-source, cross-platform system that provides developers with an extensive suite of software tools for image analysis. Developed through extreme programming methodologies, ITK employs leading-edge algorithms for registering and segmenting multidimensional data. The algorithm has been tested on nine data sets and the results are favorable. Aside from segmenting the full human diaphragm, the algorithm segments the diaphragm surrounding organs, including the lungs and ribcage which are required for lung biomechanical modeling. As such, our

first research objective was met in this chapter. This chapter is adopted from a research paper with the same name by Elham Karami, Yong Wang, Stewart Gaede, Ting-Yim Lee, and Abbas Samani published in *J. Med. Imag.* 3(4), 046004 (Nov 22, 2016).

1.13.2 *Chapter 3 - In-vivo lung biomechanical model for effective tumor motion tracking in external beam radiation therapy*

A lung biomechanical model was developed for simulating the lung deformation and tracking the tumor motion. The proposed FE model uses a novel approach for modeling the tissue incompressibility parameter and boundary conditions leading to high accuracy in tumor motion/ deformation estimation. This chapter is adopted from a research paper with the same name by Elham Karami, Stewart Gaede, Ting-Yim Lee, and Abbas Samani. It is currently being under review in *Medical Physics Journal*.

1.13.3 *Chapter 4 - Novel PCA-based Model of Human Diaphragm Motion Derived from 4D CT Images for Effective Tumor Motion Management*

In this chapter, a novel PCA-based model is proposed for representing the diaphragm motion in a compact mathematical form required for real-time estimation of diaphragm motion from chest motion data. The model was developed using 4D-CT data sets obtained from 10 cancer patients. The results indicate favorable accuracy, paving the way towards real-time estimation of lung boundary conditions from chest motion data. This chapter is adopted from a research paper with the same name by Elham Karami, Stewart Gaede, Ting-Yim Lee, and Abbas Samani. It is being under review in *J. Med. Imag.*

1.13.4 *Chapter 5 - A Neural Network Approach for Biomechanics-based Tracking of Lung Tumors during External Beam Radiation Therapy*

In this chapter, a NN-based approach is proposed for estimating the diaphragm motion and trans-pulmonary pressure from chest motion data. The performance of NNs for addressing the intra-fraction variations was validated by testing their performance on three subjects. In addition, the model performance for predicting the inter-fraction variations of

respiratory motion was tested on two subjects. This chapter is adopted from a research paper with the same name by Elham Karami, Stewart Gaede, Ting-Yim Lee, and Abbas Samani. It is being under review in *Journal of Expert Systems with Applications*.

1.13.5 Chapter 6 – Conclusions and future work

In this final chapter, an overview of the overall findings and conclusions of the thesis are summarized while the limitations of the algorithms are discussed. This section concludes by suggesting future directions and studies which can further build upon this work.

1.14 References

1. Torre LA, Bray F, Siegel RL, Ferlay J, Lortet-tieulent J, Jemal A. Global Cancer Statistics, 2012. *CA a cancer J Clin*. 2015;65(2):87-108. doi:10.3322/caac.21262.
2. Statistics Canada. Canadian Cancer Statistics. *Can Cancer Soc*. 2016;2016.
3. American Cancer Society. Lung cancer (Non-small cell). <http://www.cancer.org/cancer/lungcancer-non-smallcell/detailedguide/non-small-cell-lung-cancer-what-is-non-small-cell-lung-cancer> Accessed January 8, 2014. 2013. <http://www.cancer.org/acs/groups/cid/documents/webcontent/003115-pdf.pdf>.
4. American Cancer Society. Cancer Facts & Figures 2016. *Cancer Facts Fig 2016*. 2016:1-9. doi:10.1097/01.NNR.0000289503.22414.79.
5. Sobin LH, Gospodarowicz MK, Wittekind C. *TNM Classification of Malignant Tumours*. Vol 10.; 2009.
6. American Cancer Society. Cancer Treatment & Survivorship Facts and Figures 2014-2015. *Atlanta Am Cancer Soc*. 2014:44. doi:10.3322/caac.21235.
7. Shirvani SM, Jiang J, Chang JY, et al. Comparative Effectiveness of 5 Treatment Strategies for Early-Stage Non-Small Cell Lung Cancer in the Elderly. *Int J Radiat Oncol*. 2012;84(5):1060-1070. doi:10.1016/j.ijrobp.2012.07.2354.
8. PDQ Adult Treatment Editorial Board. *Non-Small Cell Lung Cancer Treatment*

(PDQ®): Health Professional Version.; 2002.

<http://www.ncbi.nlm.nih.gov/pubmed/26389347>
<http://www.ncbi.nlm.nih.gov/pubmed/26389304>.

9. Quoix E, Ramlau R, Westeel V, et al. Therapeutic vaccination with TG4010 and first-line chemotherapy in advanced non-small-cell lung cancer: a controlled phase 2B trial. *Lancet Oncol*. 2011;12(12):1125-1133.
<http://view.ncbi.nlm.nih.gov/pubmed/22019520>.
10. Lyman JT. Complication probability as assessed from Dose-Volume Histograms. *Radiat Res Suppl*. 1985;8(2):S13-S19. doi:10.2307/3583506.
11. Palma D, Visser O, Lagerwaard FJ, Belderbos J, Slotman BJ, Senan S. Impact of introducing stereotactic lung radiotherapy for elderly patients with stage I non-small-cell lung cancer: A population-based time-trend analysis. *J Clin Oncol*. 2010;28(35):5153-5159. doi:10.1200/JCO.2010.30.0731.
12. Rana S, Simpson H, Larson G, Zheng Y. Dosimetric impact of number of treatment fields in uniform scanning proton therapy planning of lung cancer. *J Med Phys*. 2014;39(4):212. doi:10.4103/0971-6203.144483.
13. Williams PL, Bannister LH, Berry MM, et al. Gray's anatomy. *Soames, RW*. 1995;p:612. doi:10.1002/bjs.1800761258.
14. Hall JE, Guyton AC. *Guyton and Hall Textbook of Medical Physiology*. Vol 53.; 2011. doi:10.1017/CBO9781107415324.004.
15. Glide-Hurst CK, Chetty IJ. Improving radiotherapy planning, delivery accuracy, and normal tissue sparing using cutting edge technologies. *J Thorac Dis*. 2014;6(4):303-318. doi:10.3978/j.issn.2072-1439.2013.11.10.
16. Keall PJ, Mageras GS, Balter JM, et al. *The Management of Respiratory Motion in Radiation Oncology Report of AAPM Task Group 76*. Vol 33.; 2006. doi:10.1118/1.2349696.
17. Cui Y, Dy JG, Sharp GC, Alexander B, Jiang SB. Robust fluoroscopic respiratory

- gating for lung cancer radiotherapy without implanted fiducial markers. *Phys Med Biol*. 2007;52(3):741-755. doi:10.1088/0031-9155/52/3/015.
18. Ritchie CJ, Hsieh J, Gard MF, Godwin JD, Kim Y, Crawford CR. Predictive respiratory gating: a new method to reduce motion artifacts on CT scans. *Radiology*. 1994;190(3):847-852. doi:10.1148/radiology.190.3.8115638.
 19. Keall PJ, Kini VR, Vedam SS, Mohan R. Potential radiotherapy improvements with respiratory gating. *Australas Phys Eng Sci Med*. 2002;25(1):1-6. doi:10.1007/BF03178368.
 20. Starkschall G, Forster KM, Kitamura K, Cardenas A, Tucker SL, Stevens CW. Correlation of gross tumor volume excursion with potential benefits of respiratory gating. *Int J Radiat Oncol Biol Phys*. 2004;60(4):1291-1297. doi:10.1016/j.ijrobp.2004.07.707.
 21. Hara R, Itami J, Kondo T, et al. Stereotactic single high dose irradiation of lung tumors under respiratory gating. *Radiother Oncol*. 2002;63(2):159-163. doi:10.1016/S0167-8140(02)00063-4.
 22. Shirato H, Shimizu S, Kunieda T, et al. Physical aspects of a real-time tumor-tracking system for gated radiotherapy. *Int J Radiat Oncol Biol Phys*. 2000;48(4):1187-1195. doi:10.1016/S0360-3016(00)00748-3.
 23. Berbeco RI, Nishioka S, Shirato H, Chen GTY, Jiang SB. Residual motion of lung tumours in gated radiotherapy with external respiratory surrogates. *Phys Med Biol*. 2005;50(16):3655-3667. doi:10.1088/0031-9155/50/16/001.
 24. Hanley J, Debois MM, Mah D, et al. Deep inspiration breath-hold technique for lung tumors: The potential value of target immobilization and reduced lung density in dose escalation. *Int J Radiat Oncol Biol Phys*. 1999;45(3):603-611. doi:10.1016/S0360-3016(99)00154-6.
 25. Rosenzweig KE, Hanley J, Mah D, et al. The deep inspiration breath-hold technique in the treatment of inoperable non-small-cell lung cancer. *Int J Radiat*

- Oncol Biol Phys.* 2000;48(1):81-87. doi:10.1016/S0360-3016(00)00583-6.
26. Boda-Heggemann J, Knopf A-C, Simeonova-Chergou A, et al. Deep Inspiration Breath Hold—Based Radiation Therapy: A Clinical Review. *Int J Radiat Oncol Biol Phys.* 2016;94(3):478-492. doi:10.1016/j.ijrobp.2015.11.049.
 27. Boda-Heggemann J, Frauenfeld A, Weiss C, et al. Clinical outcome of hypofractionated breath-hold image-guided SABR of primary lung tumors and lung metastases. *Radiat Oncol.* 2014;9(1):10. doi:10.1186/1748-717X-9-10.
 28. Murphy MJ. Tracking Moving Organs in Real Time. *Semin Radiat Oncol.* 2004;14(1):91-100. doi:10.1053/j.semradonc.2003.10.005.
 29. Chen Q-S, Weinhaus MS, Deibel FC, Ciezki JP, Macklis RM. Fluoroscopic study of tumor motion due to breathing: Facilitating precise radiation therapy for lung cancer patients. *Med Phys.* 2001;28(9):1850. doi:10.1118/1.1398037.
 30. Ozhasoglu C, Murphy MJ. Issues in respiratory motion compensation during external-beam radiotherapy. *Int J Radiat Oncol Biol Phys.* 2002;52(5):1389-1399. doi:10.1016/S0360-3016(01)02789-4.
 31. Murphy MJ, Isaakson M, Jalden J. Adaptive filtering to predict lung tumor motion during free breathing. *CARS 2002 Comput Assist Radiol Surg.* 2002:539-544. doi:10.1007/978-3-642-56168-9.
 32. Schweikard A, Glosser G, Bodduluri M, Murphy MJ, Adler JR. Robotic motion compensation for respiratory movement during radiosurgery. *Comput Aided Surg.* 2000;5(4):263-277. doi:10.1002/1097-0150(2000)5:4<263::AID-IGS5>3.0.CO;2-2.
 33. Wu J, Ruan D, Cho B, et al. Electromagnetic detection and real-time DMLC adaptation to target rotation during radiotherapy. *Int J Radiat Oncol Biol Phys.* 2012;82(3). doi:10.1016/j.ijrobp.2011.06.1958.
 34. Keall PJ, Colvill E, O'Brien R, et al. The first clinical implementation of electromagnetic transponder-guided MLC tracking. *Med Phys.* 2014;41(2):20702.

doi:10.1118/1.4862509.

35. Keall PJ, Sawant A, Cho B, et al. Electromagnetic-guided dynamic multileaf collimator tracking enables motion management for intensity-modulated arc therapy. *Int J Radiat Oncol Biol Phys*. 2011;79(1):312-320. doi:10.1016/j.ijrobp.2010.03.011.
36. Balter JM, Wright JN, Newell LJ, et al. Accuracy of a wireless localization system for radiotherapy. *Int J Radiat Oncol Biol Phys*. 2005;61(3):933-937. doi:10.1016/j.ijrobp.2004.11.009.
37. Imura M, Yamazaki K, Shirato H, et al. Insertion and fixation of fiducial markers for setup and tracking of lung tumors in radiotherapy. *Int J Radiat Oncol Biol Phys*. 2005;63(5):1442-1447. doi:10.1016/j.ijrobp.2005.04.024.
38. Ahn S, Yi B, Suh Y, et al. A feasibility study on the prediction of tumour location in the lung from skin motion. *Br J Radiol*. 2004;77(919):588-596. doi:10.1259/bjr/64800801.
39. Hoisak JDP, Sixel KE, Tirona R, Cheung PCF, Pignol JP. Correlation of lung tumor motion with external surrogate indicators of respiration. *Int J Radiat Oncol Biol Phys*. 2004;60(4):1298-1306. doi:10.1016/j.ijrobp.2004.07.681.
40. Tsunashima Y, Sakae T, Shioyama Y, et al. Correlation between the respiratory waveform measured using a respiratory sensor and 3D tumor motion in gated radiotherapy. *Int J Radiat Oncol Biol Phys*. 2004;60(3):951-958. doi:10.1016/j.ijrobp.2004.06.026.
41. Wilms M, Werner R, Ehrhardt J, Schmidt-Richberg A, Schlemmer H-P, Handels H. Multivariate regression approaches for surrogate-based diffeomorphic estimation of respiratory motion in radiation therapy. *Phys Med Biol*. 2014;59(5):1147-1164. doi:10.1088/0031-9155/59/5/1147.
42. Weiss E, Wijesooriya K, Dill SV, Keall PJ. Tumor and normal tissue motion in the thorax during respiration: Analysis of volumetric and positional variations using

- 4D CT. *Int J Radiat Oncol Biol Phys*. 2007;67(1):296-307.
doi:10.1016/j.ijrobp.2006.09.009.
43. Decarlo D, Kaye J, Metaxas D, et al. Integrating Anatomy and Physiology for Behavior Modeling Integrating Anatomy and Physiology for Behavior Modeling Integrating Anatomy and Physiology for Behavior Modeling. *NI*. 1995.
<http://repository.upenn.edu/hms%5Cnhttp://repository.upenn.edu/hms/76>.
44. Zhang T, Orton NP, Mackie TR, Paliwal BR. Technical note: A novel boundary condition using contact elements for finite element based deformable image registration. *Med Phys*. 2004;31(9):2412-2415. doi:10.1118/1.1774131.
45. Villard PF, Beuve M, Shariat B, Baudet V, Jaillet F. Simulation of lung behaviour with finite elements : Influence of bio-mechanical parameters. In: *Proceedings - Third International Conference on Medical Information Visualisation - BioMedical Visualisation, MediVis 2005*. Vol 2005. ; 2005:9-14.
doi:10.1109/MEDIVIS.2005.15.
46. Eom J, Shi C, Xu XG, De S. Modeling respiratory motion for cancer radiation therapy based on patient-specific 4D CT data. In: *Lecture Notes in Computer Science (Including Subseries Lecture Notes in Artificial Intelligence and Lecture Notes in Bioinformatics)*. Vol 5762 LNCS. ; 2009:348-355. doi:10.1007/978-3-642-04271-3_43.
47. Werner R, Ehrhardt J, Schmidt R, Handels H. Patient-specific finite element modeling of respiratory lung motion using 4D CT image data. *Med Phys*. 2009;36(5):1500-1511. doi:10.1118/1.3101820.
48. Al-Mayah A, Moseley J, Velec M, Brock KK. Sliding characteristic and material compressibility of human lung: parametric study and verification. *Med Phys*. 2009;36(10):4625-4633. doi:10.1118/1.3218761.
49. Al-Mayah A, Moseley J, Velec M, Hunter S, Brock K. Deformable image registration of heterogeneous human lung incorporating the bronchial tree. *Med Phys*. 2010;37(9):4560-4571. doi:10.1118/1.3471020.

50. Al-Mayah A, Moseley J, Brock KK. Contact surface and material nonlinearity modeling of human lungs. *Phys Med Biol*. 2008;53(1):305-317. doi:10.1088/0031-9155/53/1/022.
51. Al-Mayah A, Moseley J, Velec M, Brock K. Effect of Friction and Material Compressibility on Deformable Modeling of Human Lung. In: *Biomedical Simulation SE - 11*. Vol 5104. ; 2008:98-106. doi:10.1007/978-3-540-70521-5_11.
52. Fuerst B, Mansi T, Carnis F, et al. Patient-Specific Biomechanical Model for the Prediction of Lung Motion From 4-D CT Images. *IEEE Trans Med Imaging*. 2015;34(2):599-607.
53. Isaksson M, Jalden J, Murphy MJ. On using an adaptive neural network to predict lung tumor motion during respiration for radiotherapy applications. *Med Phys*. 2005;32(12):3801-3809. doi:10.1118/1.2134958.
54. Samet H, Tamminen MK. Efficient Component Labeling of Images of Arbitrary Dimension Represented by Linear Bintree. *IEEE Trans Pattern Anal Mach Intell*. 1988;10(4):579-586. doi:10.1109/34.3918.
55. Adams R, Bischof L. Seeded region growing. *IEEE Trans Pattern Anal Mach Intell*. 1994;16(6):641-647. doi:10.1109/34.295913.
56. Holzapfel G. Nonlinear solid mechanics: A continuum approach for engineering. *Work*. 2000;First Edit:455. doi:10.1023/A:1020843529530.
57. Pearson K. On lines and planes of closest fit to systems of points in space. *London, Edinburgh, Dublin Philos Mag J Sci*. 1901;2(1):559-572. doi:10.1080/14786440109462720.
58. Hotelling H. Analysis of a complex of statistical variables into principal components. *J Educ Psychol*. 1933;24(6):417-441. doi:10.1037/h0071325.
59. Gurney K. *An Introduction to Neural Networks*. Vol 14.; 1997. doi:10.1016/S0925-2312(96)00046-X.
60. Lippmann RP. An Introduction to Computing with Neural Nets. *IEEE ASSP Mag*.

1987;4(2):4-22. doi:10.1109/MASSP.1987.1165576.

Chapter 2 « Anatomy-based algorithm for automatic segmentation of human diaphragm in non-contrast CT images »

2.1 Introduction

The diaphragm is a muscular and tendinous septum which has two important roles of separating the thorax from the abdominal organs and serving as the primary muscle of respiration. Accurate delineation of the diaphragm in medical images is required in a number of biomedical and clinical applications. For instance, it is used in anatomical and functional assessment of the diaphragm¹⁻⁴. Segmentation of the diaphragm in medical images can also simplify segmentations of other abdominal organs such as the liver⁵. Mechanical modeling has recently emerged as an attractive approach for computer assisted medical intervention. Examples of such applications where the diaphragm geometry is required for modeling include lung radiation therapy and liver intervention⁶⁻¹⁰. Diaphragm segmentation is not straight-forward as routinely acquired thoracic non-contrast CT images have low contrast such that the diaphragm image intensity distribution is similar to that of the surrounding organs such as the heart, liver and spleen.

While there is a plethora of segmentation algorithms in the literature, most algorithms fall into one of three approaches: edge based, region-based and classification-based. None of these approaches or their combinations are suitable for diaphragm segmentation due to its small thickness, heterogeneity and lack of contrast with surrounding organs. As such, most reported diaphragm segmentation methods in the literature use modeling with *a priori* knowledge of the diaphragm's anatomy to delineate its surface in non-contrast CT images. One of the first diaphragm segmentation algorithms was proposed by Beichel et al¹¹ where they employed a 3D version of the Active Appearance Model (AAM) proposed earlier by Cootes et al.¹² to segment the left and right domes of the diaphragm. Another algorithm

was proposed by Zhou et al.¹³ where they modelled the diaphragm as a thin plate spline which passes through the bottom surface of the lungs. A similar approach to that of Zhou et al. was proposed by Rangayyan et al.¹⁴ where they modelled the diaphragm domes as quadratic surfaces. The results obtained by this group are more accurate as they used Active Contours¹⁵ to pull the initial approximate diaphragm surface towards its actual surface in the image.

Recently, a method was proposed by Yalamanchili et al.¹⁶ where they modelled the diaphragm as a directed graph and solved the segmentation problem by determining the optimal surface in a volumetric graph. While applications such as biomechanical modeling require the entire diaphragm as well as accurate diaphragm boundary conditions, the only group who attempted to segment the entire diaphragm was Rangayyan et al. However, as Rangayyan et al. stated in their discussion, their algorithm overestimates the lumbar part of the diaphragm and the details of diaphragm attachments to the ribcage and spine are missing in the final result.

In this paper, a fully automatic algorithm is presented for segmentation of the entire diaphragm. This algorithm is a substantially refined and more accurate version of the algorithm we presented recently¹⁷. In the previous algorithm, the feasibility of full diaphragm segmentation was demonstrated by applying a conceptual version of the proposed algorithm on one case. In this study, the enhanced algorithm was applied to 9 diaphragm cases and statistics of Hausdorff distance, Mean Distance to the Closest Point (MDCP), Average Symmetric Absolute Surface Distance (ASASD) and Symmetric RMS Surface Distance (SRMSSD) are presented. The main idea of the proposed method is that although the diaphragm is not clearly visible in non-contrast CT images, it has contact surfaces with its surrounding structures which can be segmented reasonably accurately in these images. As such, the entire diaphragm can be segmented by finding its contact surfaces with the surrounding structures followed by applying a B-spline approximation method to connect them.

Section 2.2 provides necessary information about the human diaphragm anatomy which was directly used in the algorithm. Section 2.3 describes the segmentation method while Section 2.4 presents segmentation results obtained in this study. Section 2.5 summarizes

the findings, strengths and limitations of the proposed algorithm and finally conclusions are presented in Section 2.6.

2.2 Diaphragm Anatomy

Given that the proposed segmentation algorithm relies on anatomical information of the diaphragm and its surrounding structures, this section describes relevant anatomical features of the human diaphragm. The diaphragm is a dome-shaped sheath which separates the thorax from the abdomen by serving as the floor of the former and roof of the latter. Figure 2-1 (a) is an inferior view of the diaphragm with its attachments to the surrounding structures. As shown in this figure, the periphery of the diaphragm consists of muscular fibers which originate from the posterior surface of the xiphoid process, 6th to 12th ribs, the costal cartilage, and the lumbar vertebra. The central portion of the diaphragm which is attached to the pericardium is tendinous. The diaphragm has several openings, one of which is located at its posterior part to allow the descending aorta to pass from the thoracic through to the abdominal cavities¹⁸. In fact, the diaphragm is attached to the lumbar vertebrae by means of two diaphragm pillars that wrap around the aorta as shown in Figure 2-1 (a). Figure 2-1 (b) illustrates an axial CT image acquired from a lung cancer patient. In this image, the aorta and diaphragm's pillars are shown with arrow heads. Figure 2-1 (c) illustrates a coronal view of the diaphragm where the diaphragm domes are seen in contact with the bottom surface of the lungs while the diaphragm's central tendon is attached to the pericardium. This figure also illustrates the circumference of the diaphragm originating from the ribs, while its lateral sides are located adjacent to the 6th to 12th ribs. The relative positions of the lungs, heart and lower 7 ribs with respect to the diaphragm are depicted in Figure 2-1 (d) where a coronal slice of a human chest CT scan is shown.

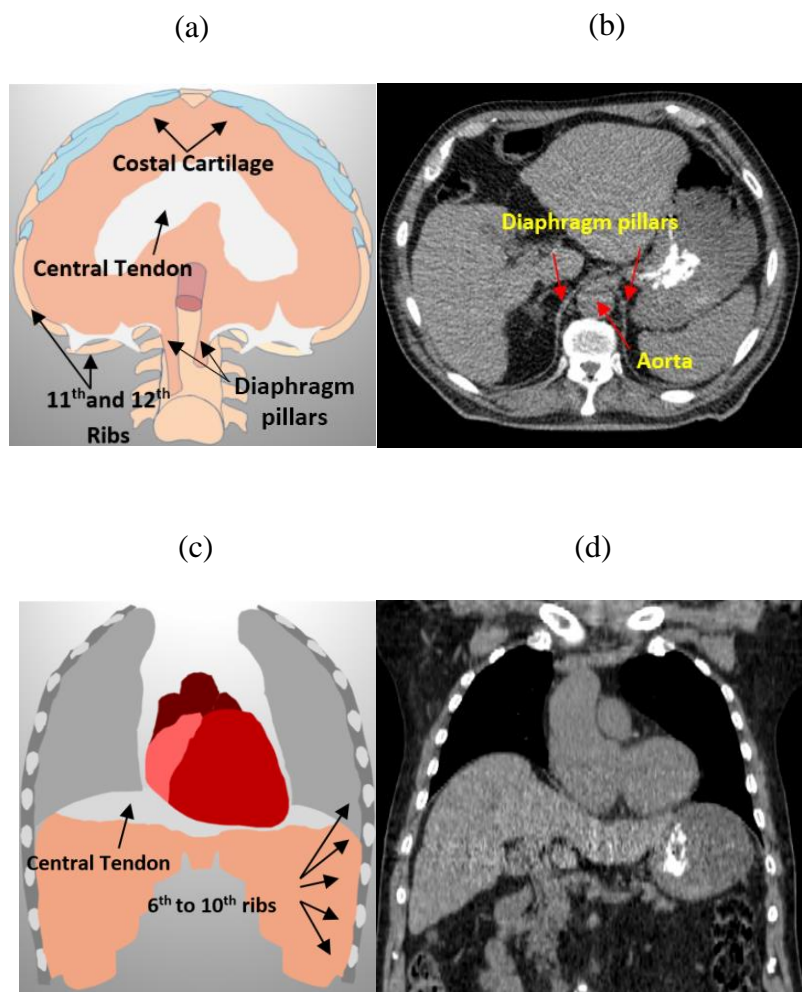


Figure 2–1 (a) A schematic view of the human diaphragm where surrounding structures (e.g. ribs and aorta) are shown, (b) an axial CT image showing the aorta and diaphragm pillars, (c) a schematic view of the human diaphragm and (d) a coronal CT image showing the relative positions of the thoracic organs and abdominal organs.

It is notable that the relative position of the diaphragm to its surrounding structures does not change significantly during respiration. As such, it is expected that unlike with the Active Appearance Model approach¹¹, the shape variations of the diaphragm during respiration do not affect the accuracy of this proposed algorithm, rendering it suitable for segmenting the diaphragm in all phases of respiration to assess its function.

2.3 Methods

2.3.1 Data Acquisition

The 3D CT images used in this study correspond to the end exhalation phase of 4D CT data sets acquired from the thorax and abdomen of 9 cancer patients. The patients were scanned using a 16-slice Philips Brilliance Big Bore CT scanner (Philips Medical Systems, Cleveland, USA) operating in helical mode. The scanning parameters are: 120 kVp and 400 mAs/slice for tube potential and current, respectively. The pitch of the couch depends on the patient's breathing period and it was set to ~ 0.1 . The intraslice pixel size of the data varied from 0.98mm to 1.29mm while slice thickness was 3mm. The 4D CT images were sorted into 10 respiratory phases using the Real-time Position ManagementTM (RPM) system. In this study, efforts were made to include patients with various anatomies and disease stages to investigate the robustness of the algorithm. For example, some patients had lung and abdominal tumors located close to the diaphragm while some others had severe lung diseases such as advanced COPD. The next section describes the segmentation algorithm in detail.

2.3.2 Diaphragm Segmentation Algorithm

A step by step approach is employed in the proposed algorithm to segment the entire diaphragm. Figure 2-2 illustrates an overview of the segmentation process. As shown in this figure, the segmentation procedure begins by segmenting the diaphragm's surrounding organs. This is followed by segmenting each organ's contact surface with the diaphragm. Finally, the entire diaphragm's surface is obtained by assembling the delineated contact surfaces using multi-level B-spline approximation method.

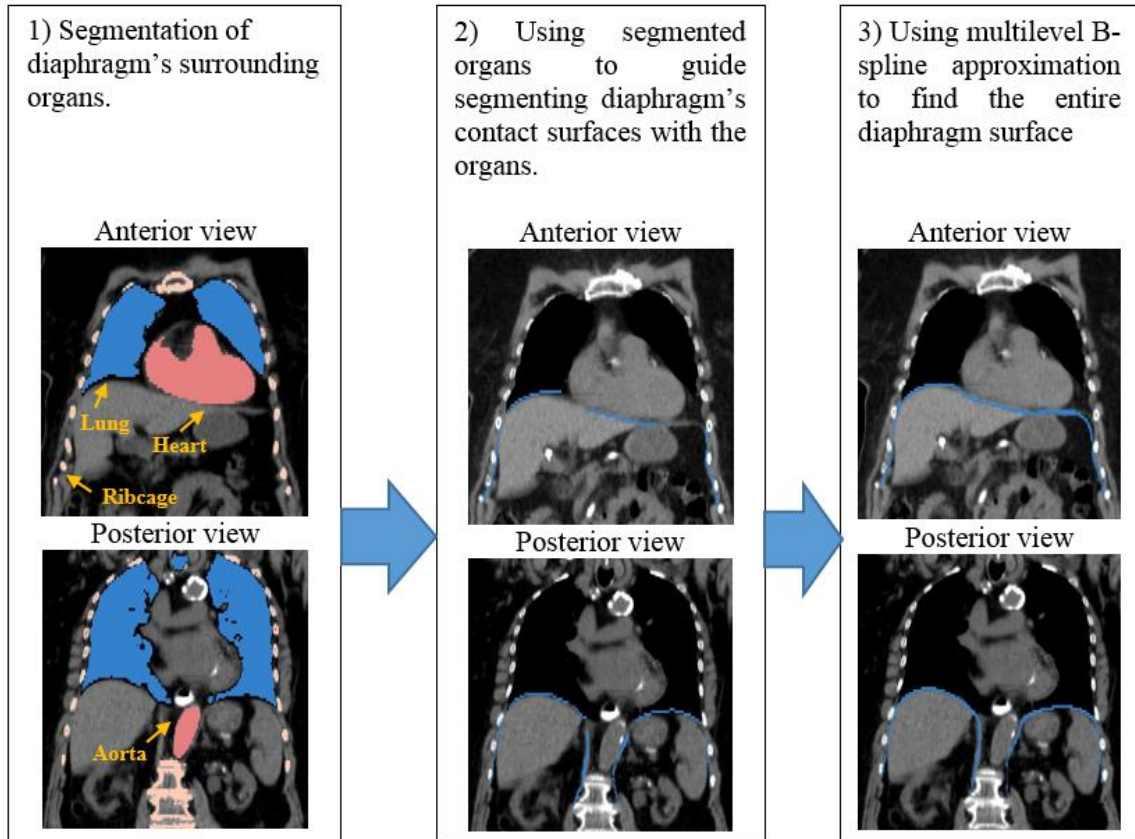


Figure 2-2 Block diagram of the proposed segmentation method.

2.3.2.1 Image denoising

Before beginning the segmentation process, all CT images used in this study were first filtered by a curvature flow filter which was proposed by Malladi et al.¹⁹. The advantage of using this filter over other denoising filters is that the boundaries remain sharp and do not become blurred. In fact, the smoothing occurs only within a region, which is very important in the context of the proposed segmentation method. The main idea of this image denoising method follows the level sets concept of viewing the pixel values as topographic maps. The very small contours in the image, which correspond to spikes of noise, can be removed by letting each contour undergo motion by a curvature obtained from solving the following anisotropic diffusion equation:

$$I_t = F(\kappa)|\nabla I|. \quad (2 - 1)$$

where I is the image, κ is the curvature and F is the speed function.

2.3.2.2 Segmentation of the ribcage and lungs

As described in Section 2.2, the circumference of the diaphragm runs along the 6th rib through to the 12th rib as well as the costal cartilage. As such, the entire ribcage has to be segmented to find its contact surfaces with the diaphragm. For this purpose, after removing noise from the CT images, the rib cage was roughly segmented by thresholding the image for values greater than 120 HU to capture all the bones and cartilage in the image. This threshold value was obtained from careful assessment of the image histograms of all 9 cases to find a threshold value for separating other soft tissue from the bone and costal cartilage. Next, connected component analysis was used to choose the largest component of the resulting image which corresponds to the rib cage. In order to segment the lungs, the CT images were thresholded at values between -950 HU and -300 HU. It is noteworthy that although the average density of lung tissue is about -700 HU and is never denser than -500 HU, we used a broader density range obtained from the image histograms to include the fibrotic tissue. Next, the lungs were found by searching for the largest connected component of the image which is located inside the ribcage. The result includes the left and right lungs as well as the bronchial tree. Since the separation of the left and right lungs is necessary for the proposed diaphragm segmentation algorithm, the bronchial tree must be segmented and then subtracted from the output obtained in the previous stage. Several algorithms have been proposed for bronchial tree segmentation. Most of these algorithms use an extended version of the region growing segmentation method to delineate the pulmonary airways²⁰⁻²⁴. In the proposed algorithm, the main aim of bronchial tree segmentation is to separate the left and right lungs while fine details of the bronchial tree are not necessary for diaphragm segmentation. As such, the original region growing algorithm was used to segment the bronchial tree. In order to initialize the region growing algorithm, the seed point was detected automatically by searching the CT axial slices one by one, starting from the 1st axial slice. Figure 2-3 (a) illustrates the intersection of an arbitrary axial slice of the CT image with the trachea being segmented. As shown in Figure 2-3 (b), the oval area of the trachea is usually present in the CT axial slices located above the lung apex. Accordingly, the initial seed point for the region growing algorithm was

detected by exploring the area of intersection to find a voxel with CT number smaller than -950 HU. The -950 HU was used instead of the air CT number, -1000 HU, to account for partial volume averaging. After separation of the bronchial tree and lungs, if the left and right lungs remain connected even following bronchial tree removal, dynamic programming can be used to separate the lungs from each other²⁵. However, in all the cases used in this study, the left and right lungs were successfully separated after bronchial tree removal.

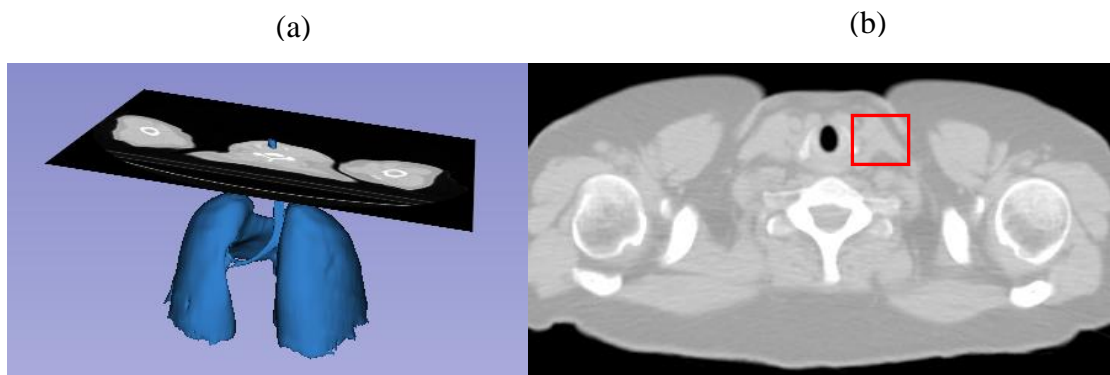
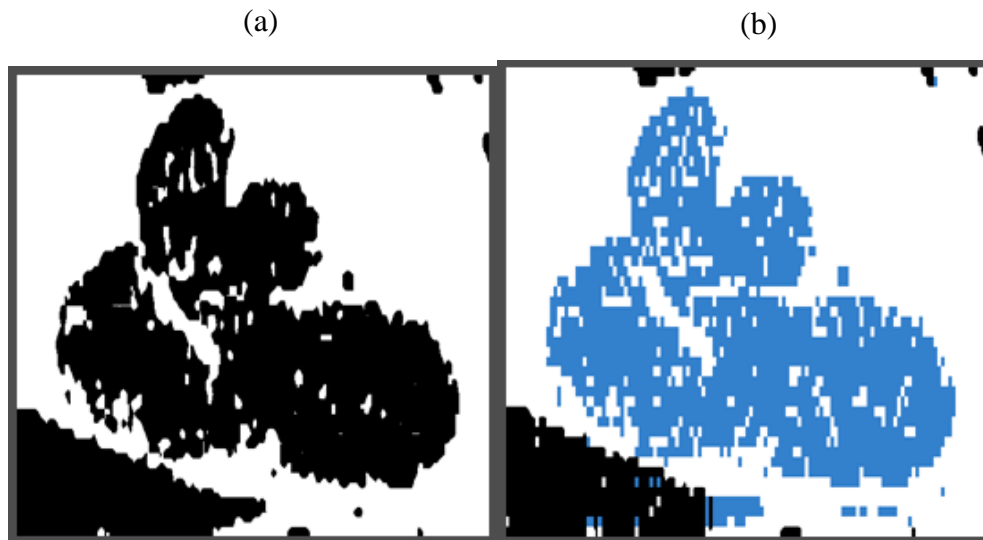


Figure 2-3 (a) The intersection area between the first axial slice of the 3D CT volume and the trachea being segmented by image thresholding used to find the initial seed point for bronchial tree segmentation. (b) The red box depicts the trachea (oval area) which is usually present in the first axial slice of the CT image.

2.3.2.3 Heart segmentation

As part of this study, we developed a fast and robust method for heart segmentation which is described in this section. Given that the heart is located between the lungs in coronal slices, it can be located using the segmented lungs. After locating the sub image which contains the heart, it is thresholded for values smaller than 35 HU to segment the heart's surrounding tissue. This threshold value corresponds to the maximum of the sub image histogram which is ~35 HU for all 9 cases. The resulting thresholded sub image, which is shown in Figure 2-4 (a), is a binary image in which the heart appears like a cavity. In the next step, zero voxels in each of the resulting coronal binary images are labeled as "contained" or "uncontained" voxels. A "contained" voxel is a voxel which is bounded by at least 4 non-zero voxels, otherwise it is labelled as "uncontained". It is noteworthy that using the aforementioned criteria for labeling the voxels, a voxel which is labeled as

“contained” is not necessarily inside the heart. The result of this labeling step is shown in Figure 2-4 (b) where the “contained” voxels are shown in blue while the “uncontained” voxels remain black. Finally, the heart is segmented by finding the largest connected component of the “contained” voxels in order to eliminate “contained” voxels outside the heart. The resulting surface is then smoothed by morphological image closing. The connected components of the “contained” voxels are shown with different colors in Figure 2-4 (c) while the segmented heart is shown in Figure 2-4 (d). The heart boundary obtained through the proposed segmentation algorithm may not always be smooth. Nevertheless, the diaphragm segmentation algorithm remains effective as the segmented heart is used indirectly to segment the heart’s contact surface with the diaphragm.



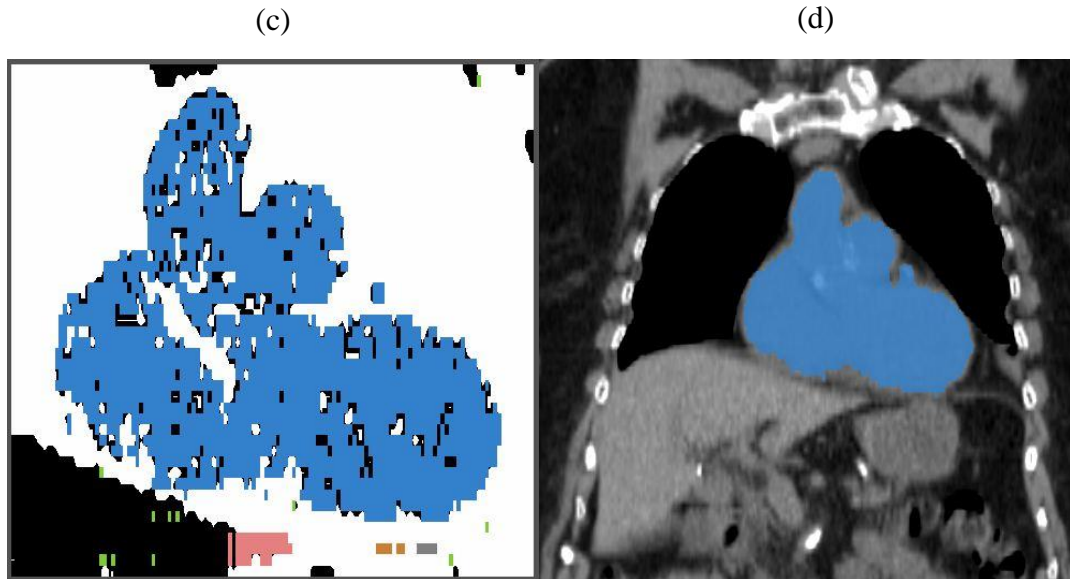


Figure 2-4 (a) A coronal sub-image containing the heart which has been thresholded for values smaller than 35 HU, (b) The zero voxels in the thresholded binary sub-image are labeled as “contained” (blue) and “uncontained” (black) voxels, (c) The color labeled connected components of the “contained” voxels, and (d) Segmented heart overlaid on the CT image.

2.3.2.4 Delineation of descending aorta

According to Figures 2-1 (a) and 2-1 (b), the diaphragm is attached to the lumbar spine by means of two tendinous pillars which wrap around the aorta. In order to segment this part of the diaphragm, the descending aorta was segmented and used to find the position of the diaphragm's lumbar part. The aorta segmentation has been tackled by many groups such as Behrens et al. and Avila-Montes et al. who used Hough transform for this purpose^{26,27}. Since segmentation of the entire aorta is not necessary in this context, the position of the lumbar spine, which is the spine portion below the lungs, was used to find the approximate location of the descending aorta. For this purpose, a volume around the spine which, according to the human anatomy includes the aorta, was extracted from the CT image. Next, Hough transform was used to find the aorta in each axial slice of the extracted volume.

2.3.2.5 *Segmenting the diaphragm contact surfaces with adjacent anatomical structures*

In order to segment the diaphragm's contact surfaces with its adjacent structures, first, all the segmented anatomical structures were dilated with a structuring element of size 1. Segmentation of the contact surfaces between these structures and the diaphragm is described in the following subsections.

2.3.2.5.1 *Lung*

As shown in Figures 2-1 (c), the diaphragm is in contact with the bottom surface of the lungs. As such, the diaphragm domes were segmented by developing an algorithm which uses the coronal slices of the CT image to find the arc shaped curves at the bottom surface of the lungs in each slice. For each lung, the algorithm begins with reading the coordinates of the voxels from one end of the lung's bottom surface. Based on the shape of the lung's bottom surface in the coronal slices, the algorithm first finds 5 consecutive voxels which have ascending height by marching towards the other end of the bottom surface. Once found, they are stored as the first diaphragm voxels in that coronal slice. Finding more such voxels is continued as long as the arc's peak is not reached. Once the height of a specific voxel starts to decline, the criteria for choosing a voxel as the diaphragm's voxel changes to having descending height. The application of this algorithm to the lung's most inferior voxels is illustrated in Figure 2-5.



Figure 2–5 The diaphragm's contact surfaces with both lungs obtained from applying an arc detection algorithm on the most inferior voxels of both lungs.

2.3.2.5.2 Heart

In order to find the heart-diaphragm contact surface, a narrow box around the bottom part of the heart was considered and Canny edge detection method was used to segment the diaphragm edges in this area. The size of the box is adjusted automatically for each coronal slice by first finding the most left, right and inferior voxels of the heart in the coronal slice. The coordinates of the box vertices are; $(L+10, B-5)$, $(L+10, B+5)$, $(R-10, B+5)$ and $(R-10, B-5)$, where L is the most left, R is the most right and B is the most inferior voxel in each coronal slice. The box coordinates and Canny filter parameters were obtained empirically by testing all 9 cases and averaging between them. The Canny filter parameters were set to: Lower Threshold = 8, Upper Threshold=10 and Variance=10. After applying Canny edge detection to the area within the box, only the closest detected edge to the heart is selected as the diaphragm's contact surface with the heart. The result is shown in Figures 2-6 (a) and 2-6 (b).

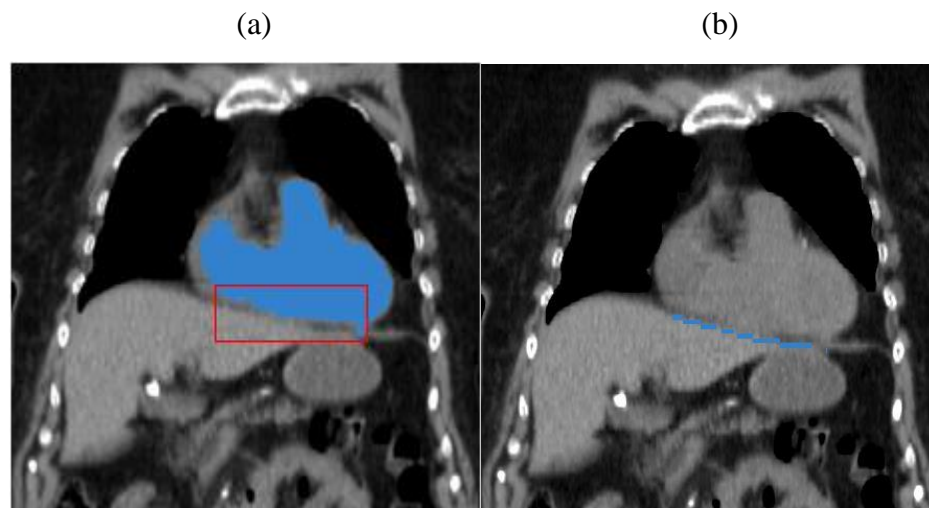


Figure 2-6 (a) A sub-image (within the shown box) containing the heart's contact surface with the diaphragm, and (b) The segmented heart's contact surface with the diaphragm obtained from applying the Canny edge detection algorithm on the selected sub-image.

2.3.2.5.3 Ribs, lumbar spine, and descending aorta

After segmentation of the ribcage and descending aorta, we used the same concept described in Sec. 2.3.2.5.2 for heart segmentation to segment the contact surfaces between the diaphragm and these organs. For that purpose, we first used morphological image closing to combine the ribcage and aorta as shown in Figure 2-7 (a). Next, the image voxels were labeled as “contained” and “uncontained” similar to what was done for the heart segmentation, thereby, allowing the boundary between the “contained” voxels and closed ribcage shown in Figure 2-7 (a) to be found. Finally, the inferior part of the obtained boundary, which is located below the lungs, was found and selected as the contact surface between the ribcage, aorta and diaphragm. The result is shown in Figure 2-7 (b).

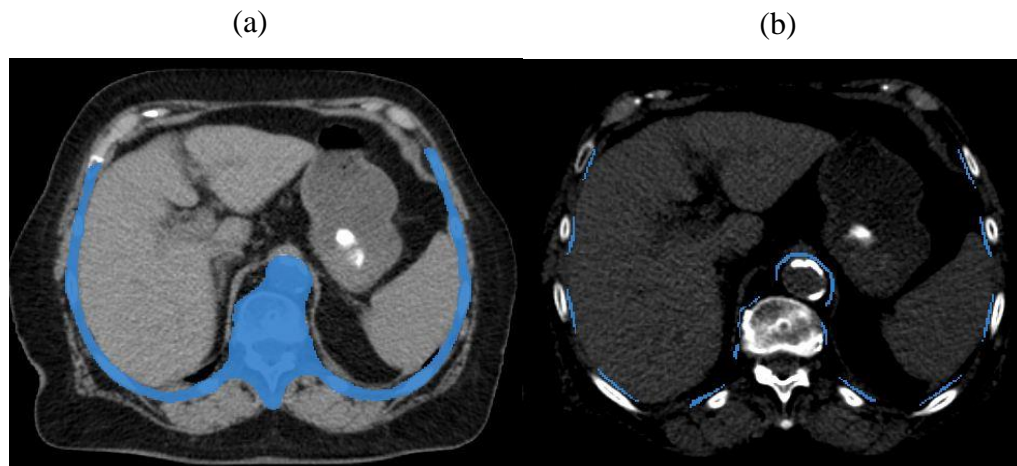


Figure 2–7 (a) Segmented ribcage and aorta after performing morphological image closing overlaid on the CT image and (b) Axial section of the contact surface between the diaphragm, ribs, spine, and aorta.

2.3.2.5.4 Multilevel B-spline

For interpolation between the diaphragm fragments obtained to approximate its entire surface, the B-spline approximation technique was used. However, it is known that a trade-off exists between the surface smoothness and segmentation accuracy. As such, the multilevel B-spline approximation proposed by Lee et al. was used for approximating the diaphragmatic surface in order to circumvent the aforementioned trade-off²⁸. The multilevel B-spline technique is based on the B-spline method of function

fitting/approximation to a set of scattered data represented by $P = \{(x_c, y_c, z_c)\}$. The function $z \cong f(x, y)$ which approximates P can be formulated as a uniform bicubic B-spline function which is defined by a control lattice Φ overlaid on a 2D plane as follows.

$$f(x, y) = \sum_{k=0}^3 \sum_{l=0}^3 B_k(s)B_l(t)\phi_{(i+k)(j+l)} , \quad (2 - 2)$$

Where $i = [x] - 1, j = [y] - 1, s = x - [x], l = y - [y]$. B_k and B_l are uniform cubic B-spline functions. As such, function f can be derived by solving for ϕ_{ij} that best approximates the data in P . These control points can be determined by using a least squares based approach, leading to:

$$\phi_{kl} = \frac{B_k(s)B_l(t)z_c}{\sum_{a=0}^3 \sum_{b=0}^3 (B_a(s)^2 B_b(t)^2)} , \quad (2 - 3)$$

The multilevel B-spline approximation is a hierarchical version of B-spline approximation technique. In this method, a hierarchy of control point lattices, $\Phi_0, \Phi_1, \dots, \Phi_h$ are used to find the approximation function f where 0 and h correspond to the coarsest and finest lattices, respectively. The approximation process begins with applying the B-spline approximation technique on the coarsest grid to find the general shape of the object which is further refined in following steps. The function f_0 obtained from the first step leaves a deviation of $\Delta^1 Z_c = z_c - f_0(x_c, y_c)$ for each point (x_c, y_c, z_c) in P . In the following step, the finer grid Φ_1 is used to find the function f_1 which approximates the deviation $\Delta^1 Z_c$. As such, $f_0 + f_1$ results in a smaller deviation for each point. Repeating this algorithm results in a more accurate approximation of P .

The accuracy of the output depends on the size of the finest mesh or the largest level used in the multilevel B-spline approximation method. In this study, the diaphragm portions segmented in the previous steps were interpolated using B-spline interpolation method with initial grid size of 4 and level 6, leading to favorable segmentation results.

The final step in this diaphragm segmentation algorithm is to obtain the end points of diaphragm's attachments to the spine. It is known that the diaphragm's pillars are attached to the third lumbar vertebra¹⁸. As such, an algorithm was developed to find the location of the third vertebra in the CT image by finding the location of the transverse processes of the

third vertebra. For this purpose, first the start point of the right 12th rib, where it is attached to the spine, was found. Hence, a narrow volume with $40\text{mm} \times 60\text{mm}$ cross section located below and at the right side of this point was inspected from top to bottom to find the third connected component. The location of the third lumbar vertebra was used to determine the circumference of the diaphragm close to the spine.

The proposed algorithm was implemented using ITK. The desktop used in this study was a core i7 intel, 2GHz. Parallel programming and multithreading was not used at this stage.

2.4 Results

Qualitative assessment: To validate the algorithm, all the images were manually segmented by an experienced radiologist. Figures 2-8, 2-9 and 2-10 illustrate the results obtained for three patients. The top row of each figure shows the automatically delineated (blue) sections of the diaphragm overlaid on their manually delineated counterparts (white). Figures 2-8 (a &b), 2-9 (a &b) and 2-10 (a &b) illustrate automatically delineated coronal sections of the diaphragm overlaid on their manually delineated counterparts while Figures 2-8 (c), 2-9 (c) and 2-10 (c) depict the same results for an axial slice of the diaphragm. The results were evaluated by comparing the automatically segmented contours with those segmented manually and independently by the radiologist. In general, there is a very good agreement between the automatic and manually segmented contours. The strong agreement exists close to the lungs, ribcage and aorta. As it is expected, the errors mainly occur close to the heart and coastal cartilage due to the difficulties in segmentation of these organs. However, only a small portion of the diaphragm is in contact with the heart and coastal cartilage. As such, we expect that the overall accuracy is not affected by these errors.

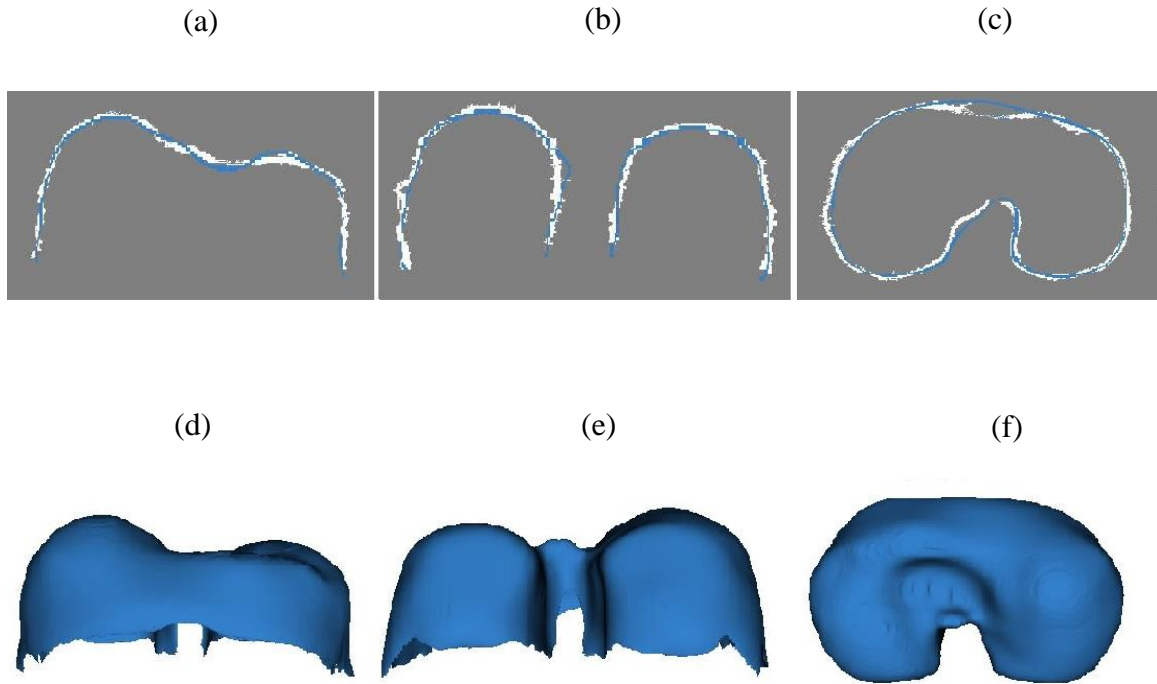
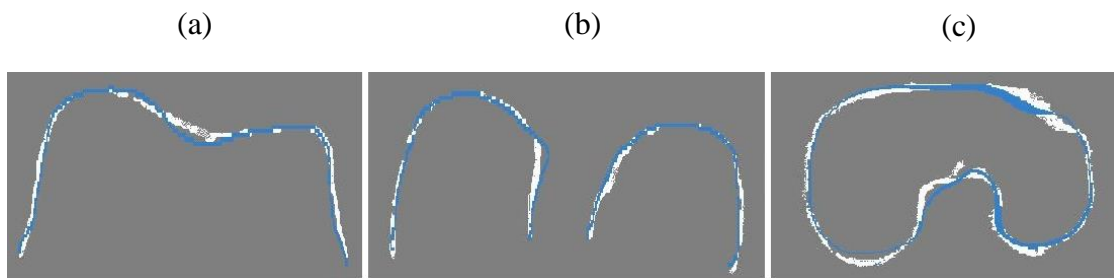


Figure 2–8 The results obtained for subject #1. The 1st row depicts automatically delineated (blue) sections of the diaphragm overlaid on their manually delineated counterpart (white). (a) and (b) are coronal and (c) is an axial view. The 2nd row depicts 3D construction of the diaphragm surface. (d) front, (e) back and (f) top views.



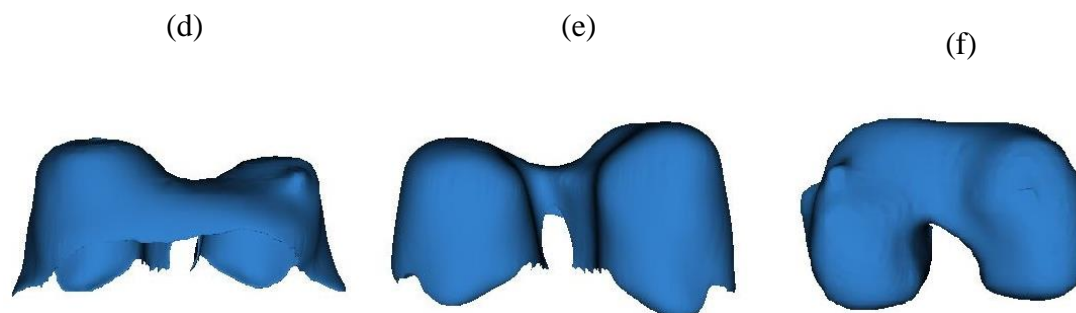


Figure 2–9 The results obtained for subject #2. The 1st row depicts automatically delineated (blue) sections of the diaphragm overlaid on their manually delineated counterpart (white). (a) and (b) are coronal and (c) is an axial view. The 2nd row depicts 3D construction of the diaphragm surface. (d) front, (e) back and (f) top views.

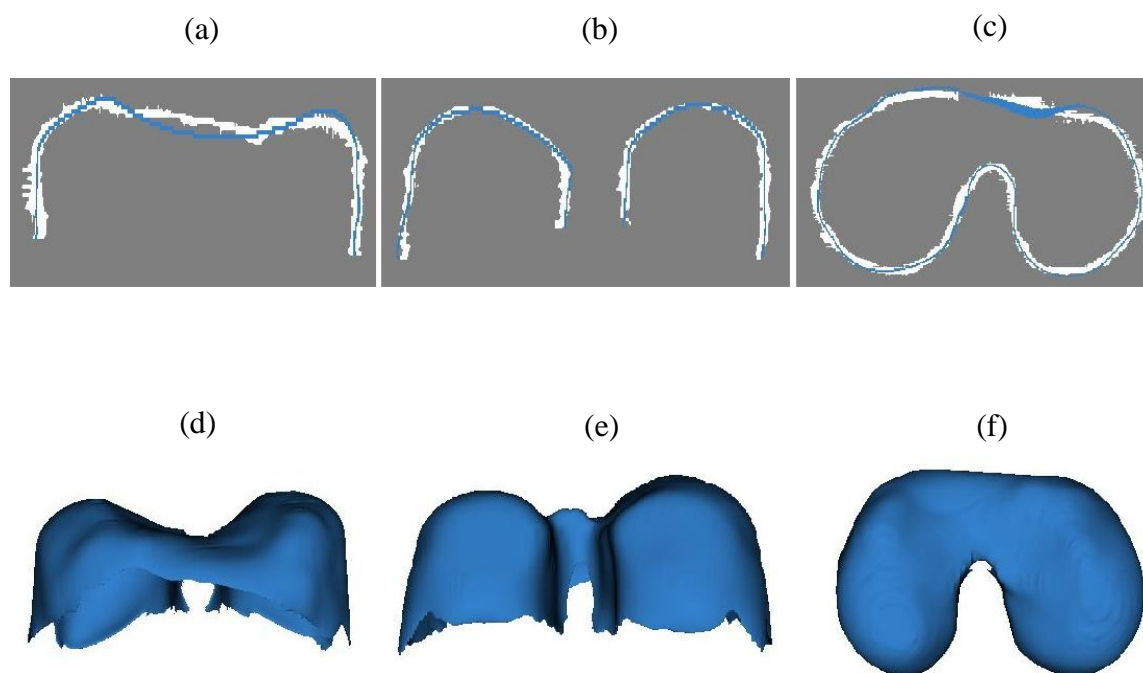


Figure 2–10 The results obtained for subject #3. The 1st row depicts automatically delineated (blue) sections of the diaphragm overlaid on their manually delineated counterpart (white). (a) and (b) are coronal and (c) is an axial view. The 2nd row depicts 3D construction of the diaphragm surface. (d) front, (e) back and (f) top views.

In Figures 2-8, 2-9 and 2-10, the bottom row of each figure illustrates different views of the 3D surface of the patient's diaphragm constructed using the automatic segmentation technique. The Model Maker module in 3D slicer was used to visualize the 3D surfaces. The model maker module is a pipeline of algorithms that start from the segmented image, creates a binary label map from the segmented image, generates a marching cubes model and runs triangle reduction and triangle smoothing algorithms.

Quantitative assessment: To assess the proposed technique's accuracy, results of the automatic segmentation of the 9 patients were compared to their manually segmented counterparts. For this comparison, four different measures were used. The Housdorff distance, mean distance to the closest point (MDCP), Average Symmetric Absolute Surface Distance (ASASD) and Symmetric RMS Surface Distance (SRMSSD). Results obtained from this comparison are summarized in Table 1. The Housdorff distance measure was calculated for the entire diaphragm surface and for its superior portion. The superior portion surface is the portion of the diaphragm that is in contact with the inferior surfaces of the lungs. The latter Housdorff distance was calculated in order to facilitate comparison with the diaphragm automatic segmentation techniques which segment only the diaphragm's upper surface. The table shows that the average MDCP is 2.55 mm, the average ASASD is 2.06 mm, the average SRMSSD is 3.51 mm and finally, the average Housdorff distance for the entire diaphragm and upper surfaces are 23.42 mm and 18.72 mm, respectively.

Subject	MDCP for entire diaphragm surface (mm)	Housdorff Distance for entire diaphragm surface (mm)	Housdorff Distance for Diaphragm's superior surface segmentation (mm)	Average Symmetric Absolute Surface Distance (mm)	Symmetric RMS Surface Distance (mm)
P #1	3.01	23.98	18.03	2.51	4.19
P #2	2.27	22.12	20.10	1.99	3.26
P #3	2.73	24.07	19.01	1.88	3.08
P #4	2.01	24.27	14.33	1.78	3.02

P #5	2.88	22.44	21.21	2.33	3.98
P #6	3.03	24.11	20.61	2.40	3.95
P #7	2.52	23.90	19.92	2.12	3.80
P #8	2.04	23.01	17.00	1.64	3.01
P #9	2.43	22.86	18.23	1.93	3.30
Mean± STD	2.55±0.39	23.42 ± 0.81	18.72 ±2.13	2.06±0.30	3.51±0.47
Range	[2.01, 3.03]	[22.12, 24.27]	[14.33, 21.21]	[1.64, 2.51]	[3.01,4.19]

Table 2-1 Results summarizing the comparison between the automatic and manual segmentation of the diaphragm of 9 patients using the mean distance to the closest point (MDCP), Housdorff distance, Average Symmetric Absolute Surface Distance (ASASD) and Symmetric RMS Surface Distance (SRMSSD).

2.5 Discussion

A fully automatic anatomy-based algorithm was proposed for segmentation of the entire diaphragm in non-contrast CT images which are the most common images used in the clinic. The challenges associated with the diaphragm segmentation, such as its similar tissue density distribution to its surrounding organs, are dealt with by using *a priori* anatomical knowledge about human diaphragm. By relying more on the diaphragm's anatomy and less on its appearance in CT images, the proposed algorithm is robust to noise-level and image contrast. An example of anatomical information utilized in the algorithm pertains to the fact that a large portion of the diaphragm is in contact with the lungs and ribcage. The lungs and ribcage have sufficient contrast with their surrounding regions in CT images, rendering their segmentation less sensitive to noise level. Besides segmenting the entire diaphragm and using the most accessible clinical images, the proposed algorithm has two important features; (1) it is fast as it typically takes ~28 minutes using a core i7 desktop to segment a full diaphragm while manual segmentation by an expert took 5 hours on average; (2) The algorithm is easy to implement; while it can be used by non-experts to segment the diaphragm for various applications including biomechanical modeling or function analysis. The proposed technique has a limitation pertaining to segmentation of the sternal part of the diaphragm where the diaphragm is in contact with the costal cartilage and the heart. The reason is that segmentation of the costal cartilage and heart is challenging

due to their similar tissue density distribution to the surrounding anatomical structures. We developed a reasonably accurate segmentation technique for the heart segmentation. However, the accuracy of segmentation in that region is lower. Another limitation pertains to a small group of subjects who have anatomical abnormalities. To address these limitations, more rigorous algorithms should be used in the first step for segmenting the diaphragm's surrounding organs which may increase the computation time. Concerning the first limitation, since only a small portion of the diaphragm is in contact with the heart and costal cartilage, accuracy in these regions does not affect the overall accuracy significantly. As for the second limitation, the step by step nature of the proposed algorithm allows the replacement of initial segmentation steps with more rigorous algorithms. However, as it increases the computation time and the algorithm's complexity, while only a small group of subjects may benefit from that, developing a separate algorithm for such subjects is justified.

The proposed algorithm might have a limitation regarding any kind of disease which affects the diaphragm's anatomy or the anatomy of its surrounding organs. In our data set, there are cases where the anatomy of ribcage or aorta has been altered but the results are still accurate as the diaphragm's anatomy has changed in a similar way. We believe that as long as the diaphragm is still in contact with its surrounding organs and those organs can be segmented with the proposed segmentation methods, the proposed algorithm can be used to segment the diaphragm effectively.

The quantitative results are listed in Table 2-1. There are four other groups who have conducted studies on diaphragm segmentation. While the four methods proposed by those groups are suitable for the applications they were designed for, none of them meets the segmentation requirements for applications which involve the diaphragm's mechanical boundary conditions (e.g. biomechanical modeling of the diaphragm). The algorithm proposed by Beichel et al. has two limitations. First, it was designed for segmenting the diaphragm's dome surface only and not the entire diaphragm. Second, their algorithm is based on Active Appearance Models (AAM) which means it is sensitive to diaphragm shape variations during breathing. The test data set they used for validating their algorithm consists of 6 original and 2 computer generated data sets. Signed error between all voxels

of the reference surface (ground truth) and the closest voxels of the model dome surface was used to assess the segmentation accuracy. They reported an average signed error of $-0.16 \pm 2.95 \text{ mm}$ for their complete data set. To facilitate comparison with this work, we calculated the average signed error of our data set which led to a value of $0.18 \pm 0.08 \text{ mm}$ that compares well with the value of $-0.16 \pm 2.95 \text{ mm}$. It is noteworthy that our results correspond to the full diaphragm scenario while their results pertain to the diaphragm's upper surface only.

Unlike Beichel et al., the algorithms proposed by Zhou et al. and Yalamanchili et al. are not sensitive to diaphragm shape variations. Both algorithms use the lung's bottom surface to find the diaphragm's upper surface. The first algorithm takes advantage of the Thin Plate Spline interpolation while the second algorithm uses a graph-based method to approximate the diaphragm's upper surface from the lung's bottom surface. While both algorithms work well for diaphragm's upper surface segmentation, again they are not suitable for applications where the entire diaphragm including its inferior boundaries are required (e.g. diaphragm biomechanical modeling application). Yalamanchili et al. applied their algorithm on 7 patients and reported an average Housdorff distance of $18.339 \pm 3.655 \text{ mm}$ which is comparable with the Housdorff distance we have obtained for the superior portion of our segmentation, $18.72 \pm 2.13 \text{ mm}$. Zhou et al. performed a step by step validation scheme. In the first step, they used a threshold value to divide the results to two groups of "good" and "poor". In the second step, the average absolute shortest Euclidian distance was used to assess the results for 30 subjects who were labeled as "good" in the 1st step. They reported an average error of 2.97 voxels (1.8 mm) for the 30 patients they selected from the "good" group. We believe that direct comparison between our results and the results reported by Zhou et al. is not possible because they removed the poor results from their study. Although we did not exclude the poor results from our data set, the mean ASASD of our results is 2.06 mm which compares well with 1.8 mm, considering that we segmented the entire diaphragm and not just its superior surface.

The results presented by Rangayyan et al. are closer to what is required for diaphragm biomechanical modeling. However, as Rangayyan et al. state in their discussion, their

algorithm overestimates the lumbar part of the diaphragm, where it is close to the spine. This overestimation results in a different diaphragm shape compared to its real shape, which can affect the accuracy of a respective diaphragm's biomechanical model. In addition, the results obtained by our group are more accurate than those reported by Rangayyan et al. (MDCP=2.55 mm vs. MDCP=5.85 mm). It is noteworthy that their segmentation goal is different from our segmentation goal and what they have achieved satisfies their goal which is abdominal tumor segmentation. However, their results are not satisfactory for diaphragm biomechanical modeling.

2.6 Conclusion

Segmentation with sufficient morphological details obtainable from the proposed segmentation technique is a prerequisite for many biomedical applications. The major application of the entire diaphragm segmentation is to develop accurate computational biomechanical models of the diaphragm. Accurately segmented diaphragm can be easily turned into a computational finite element mesh while its outline can be used to delineate necessary boundary conditions of the model. In addition, the diaphragm computational models can be used in various applications ranging from in-depth understanding of the diaphragm's physiology and developing effective diagnostic techniques of relevant respiratory diseases to computer assisted clinical procedures such as lung cancer radiotherapy and liver intervention. In depth understanding of the diaphragm's physiology can be achieved by biomechanical modelling of the diaphragm to quantify its contraction forces and assess their variation throughout respiration cycle under normal and pathological conditions. Lung cancer radiotherapy can also benefit greatly from accurate biomechanical modelling of the diaphragm as a major driver of lung tumor motion during the respiration cycle. In this case, the model can be integrated with the lung's biomechanical model to facilitate accurate prediction of the tumor motion, paving the way for computer assisted motion compensation in the radiotherapy procedure. In addition, considering that the diaphragm is an important landmark separating the thorax from the abdomen, segmenting its surface can simplify localization and segmentation of the other abdominal and thorax organs such as the liver.

The results obtained in this study indicate that the proposed algorithm is capable of accurate delineation of the entire diaphragm, paving the way for accurate biomechanical modeling of the diaphragm necessary for many clinical applications.

2.7 References

1. Nason LK, Walker CM, McNeeley MF, Burivong W, Fligner CL, Godwin JD. Imaging of the diaphragm: anatomy and function. *Radiographics*. 2012;32:E51-70. doi:10.1148/rg.322115127.
2. Pato MPM, Santos NJG, Areias P, et al. Finite element studies of the mechanical behaviour of the diaphragm in normal and pathological cases. *Comput Methods Biomech Biomed Engin*. 2011;14(6):505-513.
3. Kharma N. Dysfunction of the diaphragm: imaging as a diagnostic tool. *Curr Opin Pulm Med*. 2013;19:394-398. doi:10.1097/MCP.0b013e3283621b49.
4. Gethin-Jones TL, Noble VE, Morse CR. Quantification of diaphragm function using ultrasound: evaluation of a novel technique. *Ultrasound Med Biol*. 2010;36:1965-1969. doi:10.1016/j.ultrasmedbio.2010.08.003.
5. Zhou X, Kitagawa T, Okuo K, et al. Construction of a probabilistic atlas for automated liver segmentation in non-contrast torso CT images. *Int Congr Ser*. 2005;1281:1169-1174.
6. Fuerst B, Mansi T, Carnis F, et al. Patient-Specific Biomechanical Model for the Prediction of Lung Motion From 4-D CT Images. *IEEE Trans Med Imaging*. 2015;34(2):599-607.
7. Yang J, Cai J, Wang H, et al. Is diaphragm motion a good surrogate for liver tumor motion? *Int J Radiat Oncol Biol Phys*. 2014;90:952-958. doi:10.1016/j.ijrobp.2014.07.028.
8. Villard PF, Vidal FP, Ap Cenydd L, et al. Interventional radiology virtual simulator for liver biopsy. *Int J Comput Assist Radiol Surg*. 2014;9:255-267. doi:10.1007/s11548-013-0929-0.

9. Vedam S, Docef a., Fix M, Murphy M, Keall P. Dosimetric impact of geometric errors due to respiratory motion prediction on dynamic multileaf collimator-based four-dimensional radiation delivery. *Med Phys*. 2005;32:1607. doi:10.1118/1.1915017.
10. Tada T, Hosono M, Fujioka T, Fukuda H, Nakajima T, Inoue Y. Monitoring of respiratory movement of the diaphragm for gated radiotherapy. *Radiat Med*. 2005;23:10-13. <http://www.ncbi.nlm.nih.gov/pubmed/15786746>.
11. Beichel R, Gotschuli G, Sorantin E, Leberl FW, Sonka M. Diaphragm dome surface segmentation in CT data sets: a 3D active appearance model approach. In: *Medical Imaging 2002: Image Processing*. Vol 4684. ; 2002:475-484. doi:10.1117/12.467190.
12. Cootes TF, Edwards GJ, Taylor CJ. Active appearance models. *IEEE Trans Pattern Anal Mach Intell*. 2001;23. doi:10.1109/34.927467.
13. Zhou X, Ninomiya H, Hara T, et al. Automated estimation of the upper surface of the diaphragm in 3-D CT images. *IEEE Trans Biomed Eng*. 2008. doi:10.1109/TBME.2007.899337.
14. Rangayyan RM, Vu RH, Boag GS. Automatic delineation of the diaphragm in computed tomographic images. *J Digit Imaging*. 2008. doi:10.1007/s10278-007-9091-y.
15. Xu C, Prince JL. Snakes, shapes, and gradient vector flow. *IEEE Trans Image Process*. 1998;7:359-369. doi:10.1109/83.661186.
16. Yalamanchili R, Chittajallu D, Balanca P, et al. Automatic segmentation of the diaphragm in non-contrast CT images. In: *2010 7th IEEE International Symposium on Biomedical Imaging: From Nano to Macro, ISBI 2010 - Proceedings*. ; 2010. doi:10.1109/ISBI.2010.5490132.
17. Karami E, Gaede S, Lee T-Y, Samani A. Fully automatic algorithm for segmenting full human diaphragm in non-contrast CT Images. *Proc SPIE Med Imaging*.

- 2015;9417:941709. doi:10.1117/12.2082634.
18. Williams PL, Bannister LH, Berry MM, et al. Gray's anatomy. *Soames, RW*. 1995;p:612. doi:10.1002/bjs.1800761258.
 19. Malladi R, Sethian JA. Image processing via level set curvature flow. *Proc Natl Acad Sci U S A*. 1995;92(15):7046-7050.
 20. Fabijańska A. Two-pass region growing algorithm for segmenting airway tree from MDCT chest scans. *Comput Med Imaging Graph*. 2009;33:537-546. doi:10.1016/j.compmedimag.2009.04.012.
 21. Aykac D, Hoffman EA, McLennan G, Reinhardt JM. Segmentation and analysis of the human airway tree from three-dimensional X-ray CT images. *IEEE Trans Med Imaging*. 2003;22(8):940-950.
 22. Sonka M, Park W, Huffman E a. Rule-based detection of intrathoracic airway trees. *IEEE Trans Med Imaging*. 1996;15:314-326. doi:10.1109/42.500140.
 23. Tschirren J, Huffman E a., McLennan G, Sonka M. Intrathoracic airway trees: Segmentation and airway morphology analysis from low-dose CT scans. *IEEE Trans Med Imaging*. 2005;24:1529-1539. doi:10.1109/TMI.2005.857654.
 24. Singh H, Crawford M, Curtin J, Zwiggelaar R. Automated 3D Segmentation of the Lung Airway Tree Using Gain-Based Region Growing Approach. *Med image Comput Comput Interv*. 2004:975-982. doi:10.1007/978-3-540-30136-3_118.
 25. Hu S, Hoffman EA, Reinhardt JM. Automatic lung segmentation for accurate quantitation of volumetric X-ray CT images. *IEEE Trans Med Imaging*. 2001;20(6):490-498.
 26. Behrens T, Rohr K, Stiehl HS. Robust segmentation of tubular structures in 3-D medical images by parametric object detection and tracking. *Syst Man, Cybern Part B Cybern IEEE Trans*. 2003;33:554-561. doi:10.1109/TSMCB.2003.814305.
 27. Avila-Montes OC, Kurkure U, Nakazato R, Berman DS, Dey D, Kakadiaris I a. Segmentation of the thoracic aorta in noncontrast cardiac CT images. *IEEE J*

Biomed Heal Informatics. 2013;17:936-949. doi:10.1109/JBHI.2013.2269292.

28. Lee S, Wolberg G, Shin SY. Scattered data interpolation with multilevel b-splines. *IEEE Trans Vis Comput Graph*. 1997;3(3):228-244.

Chapter 3 « In-vivo lung biomechanical model for effective tumor motion tracking in external beam radiation therapy »

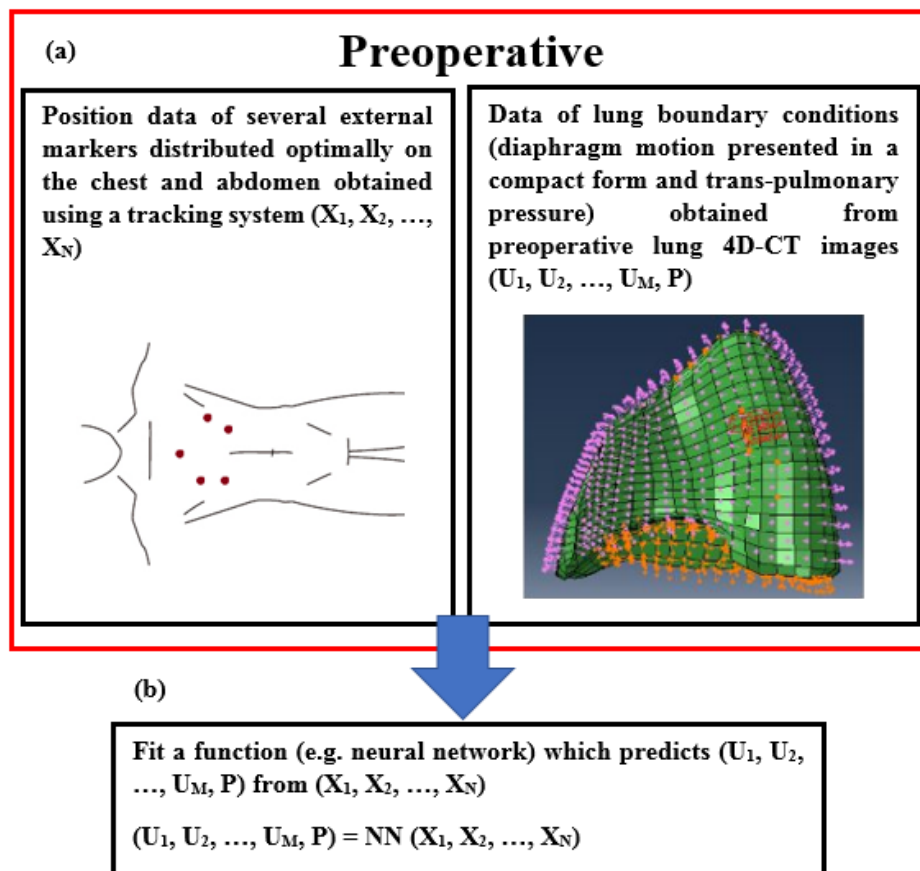
3.1 Introduction

Lung cancer is the leading cause of cancer death in both men and women. While EBRT is used extensively in treating lung cancer, it is associated with many difficulties due to respiration induced tumor motion. Among various methods proposed for tumor motion compensation, real-time tumor tracking has become popular as it can potentially lead to high normal tissue sparing, short treatment sessions and satisfactory outcome. Real-time tumor tracking methods are divided into two groups of direct and indirect tracking methods. Direct tracking methods include real-time imaging of the tumor¹ or implanted fiducial markers in the tumor^{2,3}, as well as tracking of signals produced by an active or passive device fixed at or around the tumor⁴⁻⁶. Indirect tumor tracking methods use surrogate breathing signals to track the tumor^{1,7-9}.

Currently, X-ray fluoroscopy is the modality of choice for real-time imaging of the tumor. This method not only leads to high radiation dose but also suffers from a lack of necessary image contrast as most lung tumors are not visible as a high-contrast region in fluoroscopic images. To have higher image contrast for tracking lung tumors in fluoroscopy images, artificial markers are implanted in the patient's body and used as a surrogate to the tumor. This method is invasive and requires imaging, resulting in high radiation dose. Another group of tracking methods suggest using implantable radiofrequency coils and electromagnetic detectors to track the tumor^{4-6,10,11} which is again invasive. The last group of methods suggest using external breathing signals instead of imaging. For these methods to work well, it is required to have a strong and robust correlation between the external signal and 3D tumor position. However, the physiology of respiratory motion implies that the correlation between the external signal and the internal organ is not stationary¹²⁻¹⁴.

Among the aforementioned tumor tracking methods, indirect tracking using external breathing signals is the least invasive method. However, a number of studies, which use

the motion of a single chest/abdomen marker as surrogate to tumor motion, indicate that the correlation between the chest/abdomen motion and tumor motion is not strong^{13,14}. This indicates that this lack of desirable correlation stem from the fact that the chest and abdominal surface motion cannot be fully characterized with one single marker. As such, the main challenge associated with indirect tracking methods is to establish a strong and robust correlation between the external signal and tumor motion. In addition, a recent study¹⁵ indicates that the size of the GTV (Gross Tumor Volume) can vary by up to 62.5% during breathing as a result of tumor deformation, leading to another important challenge. Therefore, an ideal tumor tracking method should be capable of predicting tumor deformation as well as its motion. In this study, we present a novel framework for tumor tracking which uses the indirect tumor tracking approach. This approach utilizes external breathing signals, in conjunction with a lung biomechanical model. The block diagram of the proposed tumor tracking method, which summarizes the method, is shown in Figure 3-1.



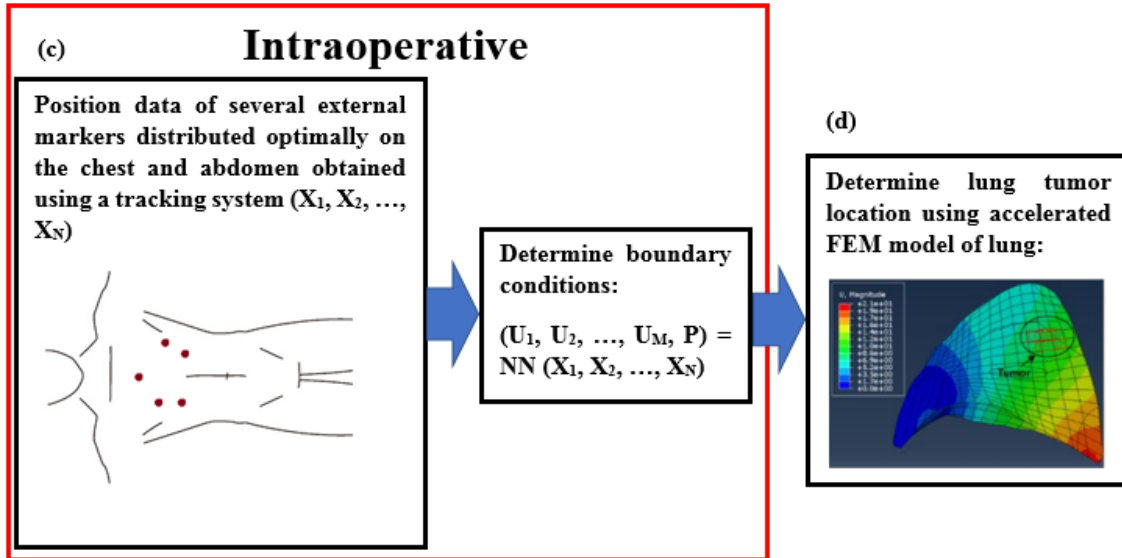


Figure 3–1 A block diagram of lung tumor tracking algorithm which involves a pre-treatment and an intra-treatment step. (a) Pre-treatment tracking of chest surface motion and image based estimation of the lung boundary conditions. The lung BCs include lung-diaphragm contact surface displacements shown in orange and lung trans-pulmonary pressure shown in purple. (b) Building a correlation model (e.g. using neural network (NN) between chest surface motion data and lung boundary conditions. The NN training requires the diaphragm to be presented in a compact form. (c) Intra-treatment chest surface motion tracking and predicting the boundary conditions in real-time. (d) Calculating lung tumor position and deformation using an accelerated lung biomechanical model.

As shown in Figure 3-1, we use a lung biomechanical model to predict the tumor motion and deformation using the real-time lung boundary conditions obtained from the chest motion data. In our proposed lung FE model, the lung boundary conditions include the diaphragm motion and trans-pulmonary pressure. The latter is the difference between intra-alveolar and intra-pleural pressures and it is calculated through optimization. Many research groups have tackled lung biomechanical modeling^{16–25}. While existing lung biomechanical models are fairly accurate, most of them cannot be incorporated effectively into a lung model based tumor tracking algorithm. Apart from the lung biomechanical model proposed by Fuerst et al., other lung biomechanical models suggest using a contact surface which limits the lung expansion to the segmented chest cavity at end inhale phase. Such a modeling approach is highly involved computationally while it is difficult to model different breathing patterns, hence precluding its real-time applicability. In this study, one

of the goals we pursued is to improve the technique proposed by Fuerst et al. by incorporating existing physiological knowledge about pressure gradients and using more realistic material properties, e.g. incompressibility parameters, which can be employed effectively in lung model based tumor tracking algorithms. Our proposed lung biomechanical model requires the real-time position of the diaphragm and trans-pulmonary pressure values as boundary conditions. As shown in Figure 3-1, those BCs can be obtained from a Neural Network which inputs the chest motion data and outputs the lung boundary conditions.

In contrast to indirect heuristic mathematical methods of lung tumor motion prediction, which rely solely on a data fitting to a mathematical model²⁶, the proposed method is a hybrid method of heuristic data fitting in conjunction with a tissue deformation, physics based model. The first component of the data fitting model is an NN used to predict the lung BCs from input chest surface motion data. To ensure robustness of this NN, an optimal number of markers leading to highest correlation between chest surface motion data and tumor motion can be determined and used instead of a single marker. The second component is the lung biomechanical model which inputs the BCs obtained from the NN to output the tumor position and geometry. This hybrid approach is believed to be more effective than using a solely heuristic model (e.g. NN) to calculate tumor position and geometry directly from the chest wall surface motion data. The reason is that the NN in the latter scenario is expected to be highly complex while being prone to data overfitting. Using an accurate lung biomechanical model in the proposed system has two advantages: 1) accuracy of tumor motion tracking will be high and 2) tumor geometry variations during respiration can be taken into account, paving the way for more accurate radiation dose distribution calculation. In this paper, our focus is the last block of Figure 3-1, which is the lung biomechanical model designed specifically for tumor tracking. The main feature of this lung biomechanical model is that it is capable of being incorporated into the described lung tumor tracking algorithm. Another interesting feature of this model is that the lung tissue incompressibility is set to be variable through respiration phases. This is more consistent with having significantly variable air content within the lung tissue throughout respiration. Finally, we took a new approach in modeling the pressure distribution and

calculated the pressure values through optimization, leading to more accurate modeling results.

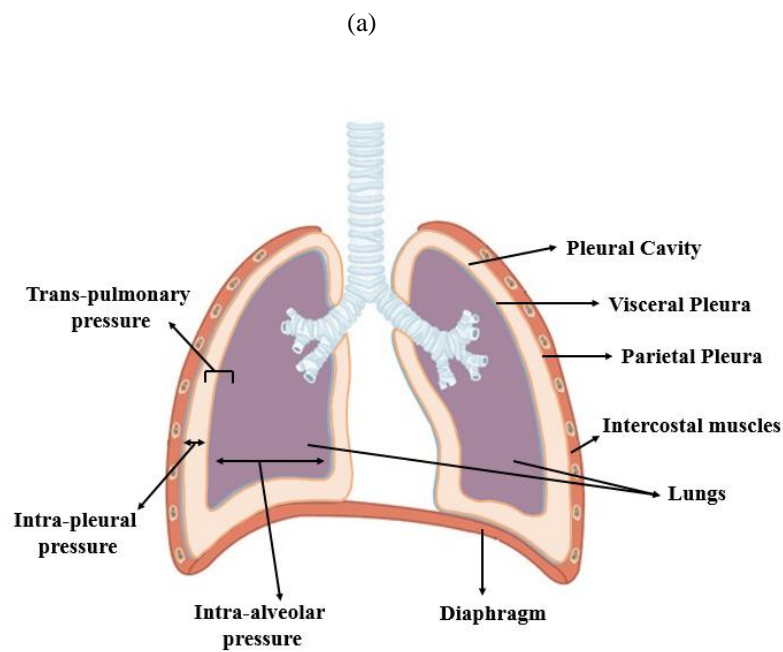
3.2 Materials & Methods

3.2.1 *Physiology of breathing*

Figure 3-2 (a) depicts a schematic of the respiratory system where the lungs, pleural cavity, trachea, and respiratory muscles are illustrated. Before inspiration, the respiratory muscles are relaxed and the intra-alveolar pressure is equal to the atmospheric pressure. The inspiration phase begins by contraction of the main respiratory muscles, i.e. diaphragm and external intercostals, and expansion of the chest cavity. The diaphragm is known to cause 75% of the thoracic cavity enlargement during inspiration while the external intercostals contraction enlarges the thoracic cavity in the lateral and AP directions. As the thoracic cavity expands, the intrapleural pressure drops and the lungs expand. This lung expansion leads to reduction of alveolar pressure; hence air flows in.

At the end of inspiration, the inspiratory muscles reach relaxation state, the diaphragm returns to its dome shape and the rib cage falls due to gravity after relaxation of external intercostals. As the chest wall and stretched lungs recoil, the volume decreases, the pressure increases; hence the air flows out.

As shown in Figure 3-2 (a), the net pressure applied to the lung is the trans-pulmonary pressure which is the difference between the alveolar pressure and intrapleural pressure. It is noteworthy that the spatial distribution of trans-pulmonary pressure is not uniform²⁷.



(b)

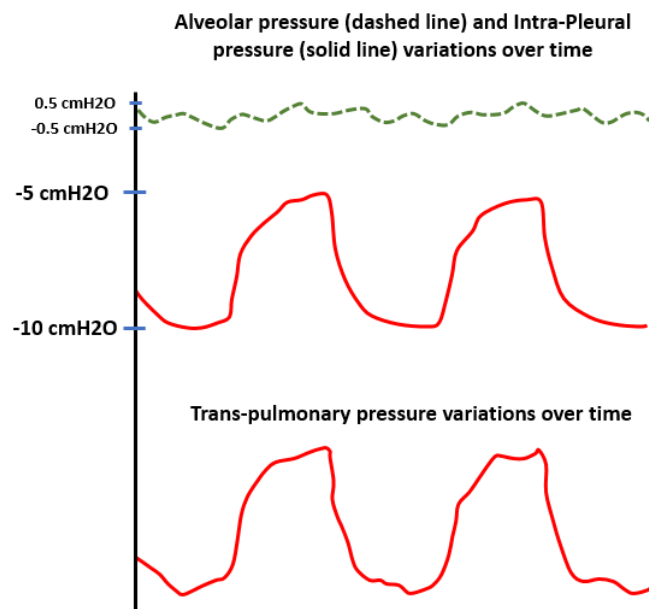


Figure 3–2 (a) The alveolar, pleural, and trans-pulmonary pressures. (b) Changes in the amplitude of intra-alveolar, intra-pleural, and trans-pulmonary pressures during respiratory cycle.

Figure 3-2 (b) depicts the temporal variations of the intra-alveolar and intra-pleural pressures during the respiratory cycle. The diaphragm and ribcage motion cause the temporal and spatial variations of the trans-pulmonary pressure. As such, to have a more accurate loading in our model, we consider the loading caused by the diaphragm and ribcage separately. As discussed earlier, data required for developing the model are acquired from 4D CT data sets. Here in this section, we explain the procedures used to obtain this data from 4D CT data.

3.2.2 Data acquisition

In this study, 4D CT images of three lung cancer patients were used to develop the lung FE models. Data acquisition has been described in Sec. 2.3.1.

3.2.3 Lung geometry and finite element mesh

The first step in developing the tumor tracking algorithm proposed in Figure 3-1, is segmenting the lungs, diaphragm, and the tumor for the end exhalation phase of respiration. To segment the lungs and diaphragm, we used a fully automatic algorithm proposed in Karami et al.²⁸ The lungs are segmented using a 3-step algorithm. The first two steps are thresholding steps to first segment the ribcage and next the lower respiratory tract. In the last step, the bronchial tree is removed from the lungs, using the region growing algorithm, and the lung surface is smoothed using morphological image closing. The diaphragm segmentation procedure is described in detail in Karami et al.²⁸ The segmented lung is used for developing the FE model and the segmented diaphragm is used for defining the boundary conditions at the lung's bottom surface. The tumor was segmented manually by an expert radiologist. Since the main objective of this study is tumor tracking, the model was developed only for the tumor-bearing lung, which was the right lung for all the subjects. However, the model can be easily developed for including the other lung too.

After segmentation, IA-FEMesh software package was used to mesh the lung using hexahedral elements as they are C^2 continuous; hence have better performance than tetrahedral elements. The lung mesh for one subject is shown in Figures 3-3 (a) and (b), and the tumor elements are highlighted.

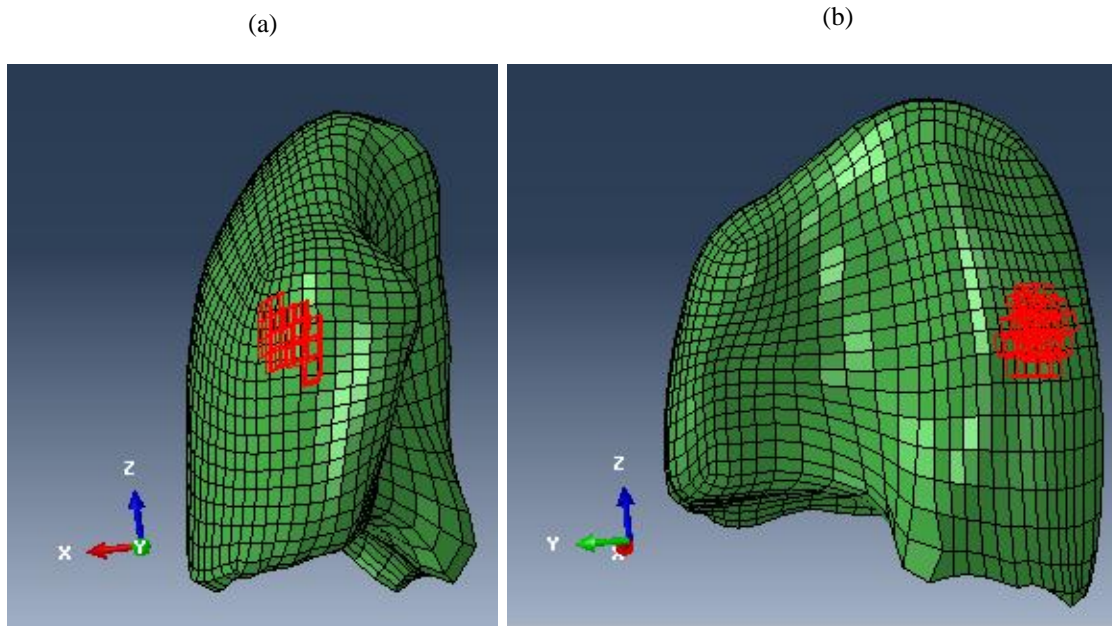


Figure 3–3 (a) Coronal and (b) sagittal views of the lung mesh with tumor elements depicted as red.

3.2.4 Tissue mechanical properties

Based on the results published by Shirzadi et al.²⁹, the Marlow hyperelastic model with variable Poisson's ratio during breathing is a suitable model for lung tissue. To use the Marlow hyperelastic model we used the experimental data published by Zeng et al³⁰ and the Poisson's ratio was obtained through an inverse optimization framework, which is described in detail in Sec. 2.5.2.

3.2.5 Boundary conditions

The most important factor in developing a lung biomechanical model for EBRT is how to model the loading so it can be updated in real-time. As described in Sec. 2.1, the lung deforms due to two different mechanisms; (1) diaphragm motion; and (2) ribcage motion. Although both mechanisms result in trans-pulmonary pressure variations, we model each source of deformation separately to obtain more accurate and patient specific models. In this paper, we demonstrate how each loading can be obtained from 4D CT data and incorporated into the lung FE model. A recent study¹⁵ indicated that the trachea can move up to 10 mm. As such, unlike some previous studies²⁹ the lung-trachea interface was free to move. Instead, a few lung FE surface nodes located close to the lung apex were fixed to

ensure model stability. The location of fixed nodes was obtained by monitoring the lung surface motion in 4D CT images.

3.2.6 Diaphragm

To obtain the diaphragm motion, after segmenting the bottom surface of the lung which is in contact with the diaphragm, The Free Form Deformation (FFD) registration method was used to obtain the displacements of the segmented surface at each phase of respiration. The diaphragm displacement field obtained from non-rigid registration is mapped onto the lung FE nodes representing the lung bottom surface shown in Figure 3-4 (a). To map the diaphragm displacement field onto the lung mesh bottom surface nodes, we used nearest neighbor interpolation method. Finally, in accordance with the pleural fluid function of providing mechanical coupling between the lung and chest wall, the mapped displacement values were assigned as prescribed displacement boundary conditions in the lung FE model^{21,23}.

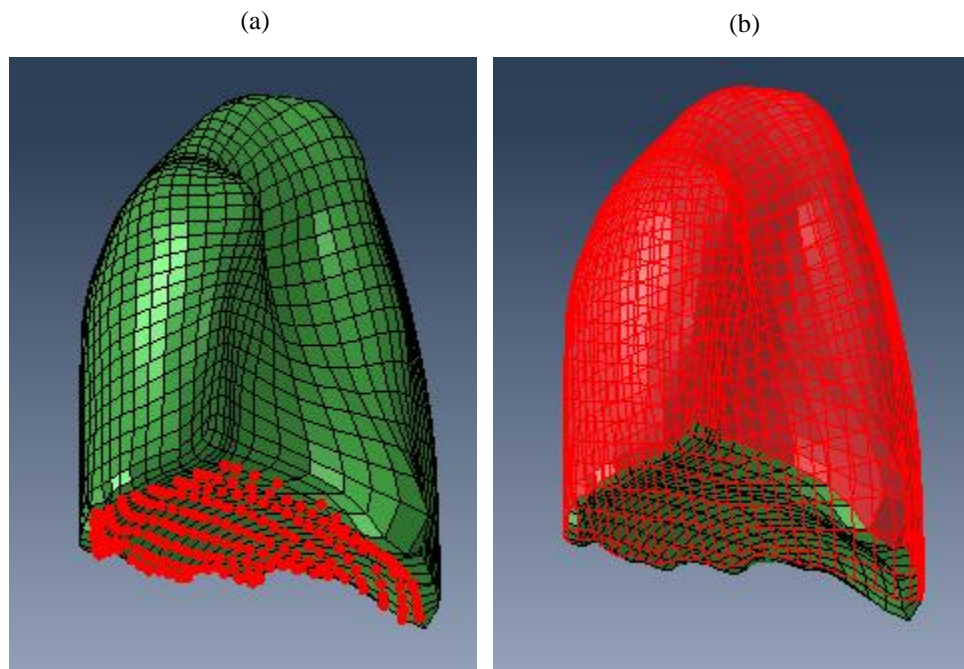


Figure 3–4 (a) Diaphragm nodes. (b) The trans-pulmonary pressure is applied on the lung surface shown in red.

3.2.7 The trans-pulmonary pressure

As described in Sec. 2.1 the net pressure applied on the lung surface is the trans-pulmonary pressure. To model the trans-pulmonary pressure created by the ribcage motion, we applied negative pressure on the surface highlighted in red as shown in Figure 3-4 (b). As stated in Sec. 2.1, the pressure distribution is non-uniform while its temporal variation is non-linear^{27,31,32}. As such, we used the results published by Tawhaj et al.³³ together with an optimization framework to model the pressure. According to Tawhaj et al., when the subject is in the supine position the pressure has a gradient in the anterior- posterior direction. After defining the pressure spatial distribution with a linearly increasing function in the AP direction, the magnitude of pressure and its temporal variations were obtained through optimization. For this purpose, we first defined the following cost function:

$$C(p, v) = \lambda \left(1 - \frac{A \cap B}{A} \right) + \gamma \psi_t \quad (3 - 1)$$

Where p is the pressure magnitude, v is the Poisson's ratio, A is the actual lung geometry, B is the simulated geometry of the lung obtained from FEA, ψ_t is the curvature of the optimized pressure curve at time t which is used for regularization purposes and λ and γ are weight factors. To obtain the A and B volumes, the actual and simulated CT images were first masked to segment the full right lung. Next, the masked images were thresholded for values smaller than -500 HU. The results are shown in Figure 3-6 for end inhale to end exhale images. Using this approach, major lung features such as major airways and the tumor are present in the segmented image leading to a more accurate pressure optimization.



Figure 3–5 The lung was segmented, excluding dense features such as tumor and major blood vessels and airways, to be used for optimization. The left image corresponds to end inhale phase and the right image corresponds to end exhale phase while the 3 images in the middle represent phases in between.

The breathing cycle is not symmetric, and exhalation usually takes longer than inhalation. In the 4D CT images used in this study, phase #1 to phase #6 correspond to exhalation phase, while the 6th time point (phase) corresponds to the end exhalation phase of respiration. The exhalation phase of respiration consists of 5 time points while the inhalation phase consists of 4 time points. Similar to the approach we took earlier in Shirzadi et al.²⁹, the exhalation phase images, e.g. phase #1 to phase #6, were used to obtain the pressure and Poisson's ratio values while the inhalation images, e.g. phase #6 to phase #10, were used for validation. The optimization procedure is shown in Figure 3-7. It is noteworthy that in the optimization framework depicted in Figure 3-7, the optimized pressure curve is the difference between the trans-pulmonary pressure at end exhalation phase and other phases of respiration. In other words, the pressure values are not the absolute values of pressure, but rather pressure values relative to end exhalation phase.

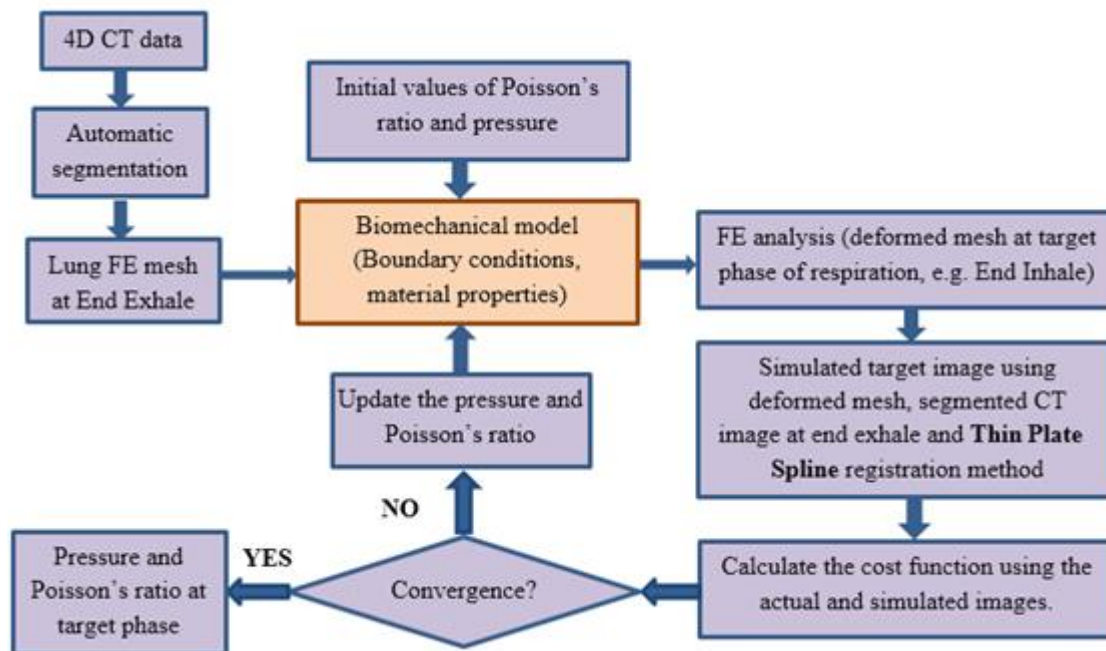


Figure 3–6 Block diagram of the proposed optimization framework for patient specific calculation of trans-pulmonary pressure and Poisson's ratio values. The optimization requires the lung FE mesh at end exhale, and the diaphragm displacement values obtained from registration. Initial values of trans-pulmonary pressure magnitude and Poisson's ratio are assigned to the model and the deformed lung mesh corresponding to the target phase is obtained. The deformed mesh is used in conjunction with Thin Plate Spline registration method to create the simulated image and calculate the cost.

3.2.8 Validation

To validate the model, the pressure and Poisson's ratio curves pertaining to exhalation and inhalation phases were assumed to be symmetrical for the entire respiratory cycle. As such, the optimized pressure values for exhalation phase were used to predict the tumor motion for the inhalation phase of respiration. We validated the model both qualitatively and quantitatively. To perform quantitative validation, a total of 40 landmarks were used where 20, 10 and 10 landmarks were selected in the middle of the lungs, close to the lung surface and close to the tumor, respectively. The landmarks were selected on the inhalation phase images including phase 6, 7, 8, 9 and 10. Phase 6 and 10 correspond to end exhalation and end inhalation phases of respiration. Following landmark selection, the GTV and the lung

surface were segmented for all those phases of respiration. The GTV was segmented by an expert radiologist while the lung surface was segmented automatically. The average 3D position error per landmark, the average Hausdorff distance between the actual and simulated lung surfaces and the Dice similarity coefficient between the actual and simulated tumor volumes are reported in the results section.

3.2.9 Implementation

The segmentation algorithms were developed using C++ and ITK. The lung FE model was developed using IA-FEMesh and ABAQUS software package and the rest of the algorithm, including the inverse optimization framework were developed in MATLAB.

3.3 Results

3.3.1 Qualitative validation

The optimized pressure and Poisson's ratio variations over respiration phases for the 3 patients are shown in Figure 3-8. It is noteworthy that, the trans-pulmonary pressure temporal variations agree qualitatively well with the data reported in the literature³². Similar to the data published in the literature^{27,32,34}, the pressure is high at the beginning of exhalation phase, it declines and plateaus until it rises again in the inhalation phase. In addition, the first half of the curve has a positive curvature while the second half, from time point #6 to #10, has a negative curvature which is in agreement with information published in the literature. As shown in Figure 3-8 (a), and according to the results published by Chiumello et al.³², the pressure is approximately symmetrical. As such, the symmetry assumption is valid. Also, the Poisson's ratio variations agree well with data published earlier in Shirzadi et al.²⁹, confirming our hypothesis. As expected and reported earlier in Shirzadi et al., the Poisson's ratio can be modelled with a quadratic function and its values are smaller when the lung's air content is higher, i.e. end inhalation phase.

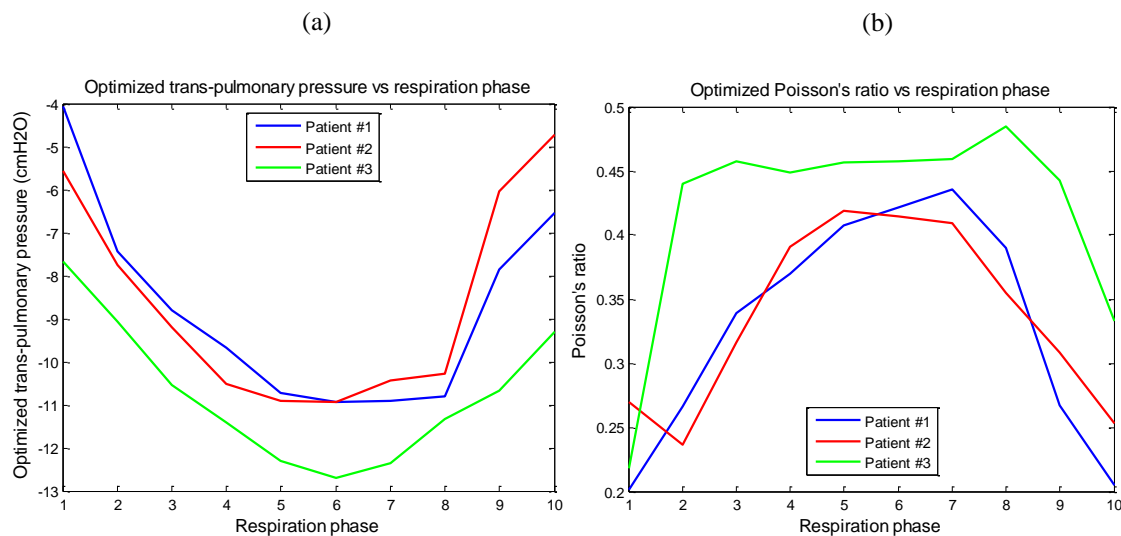
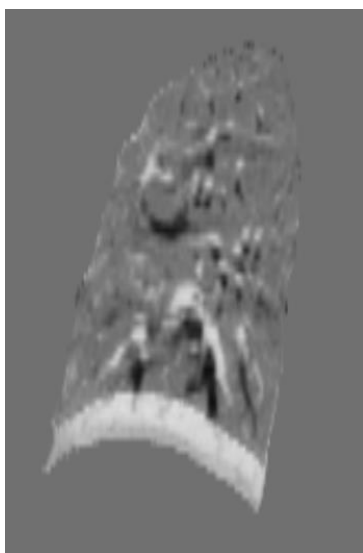


Figure 3–7 Optimized values of (a) trans-pulmonary pressure and (b) Poisson's ratio values vs. respiration phase. Phases 1, 6 and 10 represent start exhalation, end exhalation and end inhalation, respectively.

In the validation step, we ignored the second half of the curves shown in Figure 3-8, which are obtained by optimization, and instead used the mirrored version of their corresponding first half to predict the lung deformation during the second half of the respiratory cycle. More specifically, in our data sets, the end exhalation phase corresponds to time point #6. As such, for building the model, the simulation was performed between time point #6 and the other 5 time points, moving backward. To validate the model, the optimized parameters obtained in the previous step were used to simulate the lung deformation between time point #6 and phase 7 to 10, moving forward. Next, the deformed mesh obtained from FEM was used in conjunction with the Thin Plate Spline registration method to simulate the lung images shown in Figure 3-9. The left column of this figure depicts the image difference between actual end exhalation and end inhalation CT images while the right column illustrates the image difference between actual and simulated end inhalation CT images for all 3 patients.

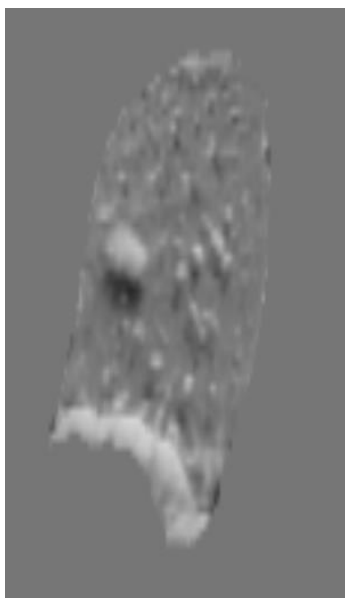
(a)



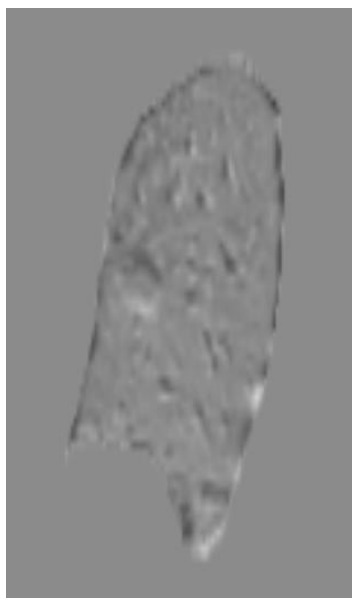
(d)



(b)



(e)



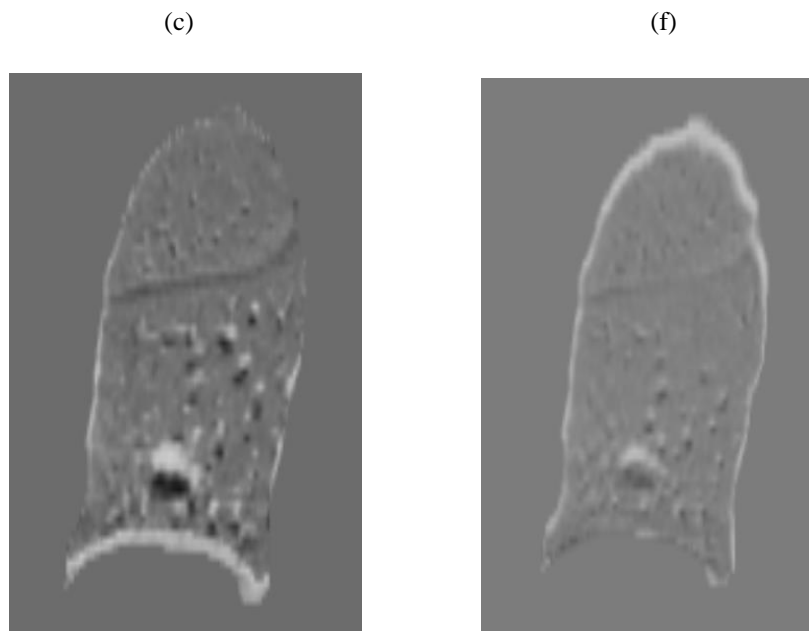


Figure 3–8 CT image difference between actual “end exhalation” and “end inhalation” CT images (a), (b), (c) and difference between actual and simulated “end inhalation” CT images (d), (e), (f) for the 3 subjects.

3.3.2 Quantitative validation

To validate the model quantitatively, we first calculated the Dice similarity coefficient between the actual and simulated GTVs. The tumor tracking results for exhalation and inhalation phases of respiration are reported in Tables 3-1 and 3-2. Table 3-1 presents the tracking results for exhalation phase of respiration which was used for developing the model. Table 3-2 presents the tumor tracking results for inhalation phase of respiration which was used for validating the model. These results suggest that the Dice similarity coefficient between the actual and simulated tumor volumes ranges between 0.78 to 0.94 while the average Dice similarity coefficient for all patients over all phases of respiration is 0.86 ± 0.05 .

Phase number	1	2	3	4	5
Patient #1	0.80	0.90	0.87	0.90	0.90

Patient #2	0.90	0.88	0.86	0.90	0.93
Patient #3	0.83	0.86	0.85	0.90	0.94
Mean \pm SD	0.84 \pm 0.05	0.88 \pm 0.02	0.86 \pm 0.01	0.90 \pm 0	0.92 \pm 0.02

Table 3-1 The Dice similarity coefficient values between actual and simulated GTVs (optimization step). The simulation has been performed between time point #6 (end exhalation phase) and the other 5 time points moving backward.

Phase number	7	8	9	10
Patient #1	0.90	0.88	0.79	0.82
Patient #2	0.93	0.78	0.81	0.79
Patient #3	0.93	0.85	0.80	0.84
Mean \pm SD	0.92 \pm 0.02	0.84 \pm 0.05	0.80 \pm 0.01	0.82 \pm 0.03

Table 3-2 The Dice similarity coefficient values between actual and simulated GTVs (validation step). The simulation has been performed between time point #6 (end exhalation phase) and the other 4 time points moving forward.

The next quantitative validation step was performed by calculating the average error per landmarks 3D position and the average distance between the actual and simulated lung surfaces for all phases of inhalation phase of respiration. The results are shown in Figure 3-10. These results indicate that the mean absolute error in the landmarks' 3D position and the average Hausdorff surface-to-surface distance are 1.74 \pm 0.77 (mm) and 1.60 \pm 0.17 (mm), respectively which are favorable.

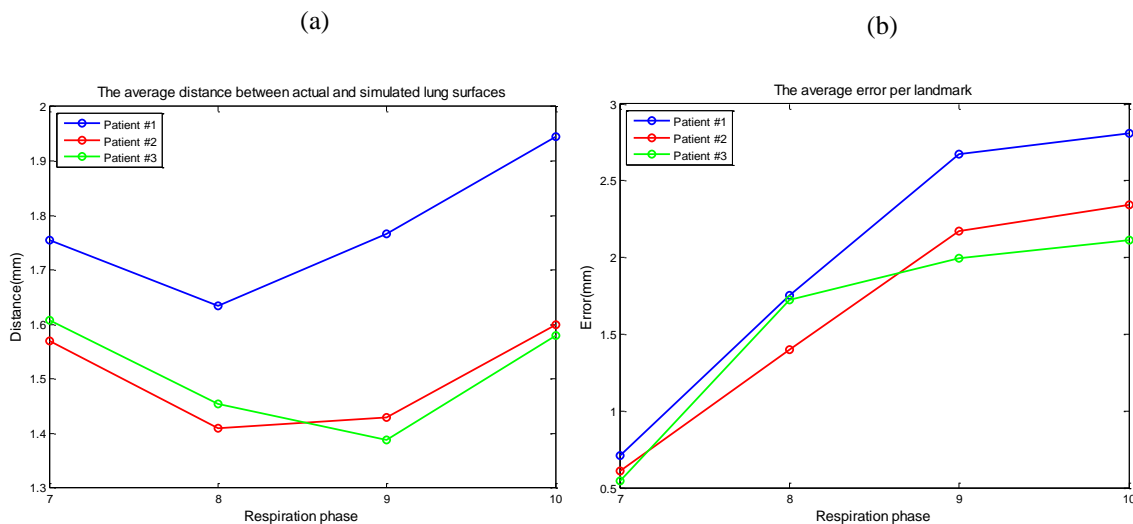


Figure 3–9 (a) Mean absolute error per landmark’s 3D position versus respiration phase. (b) Mean distance between actual and simulated lung surfaces versus respiration phase.

3.4 Discussion and Conclusions

A biomechanical model was proposed specifically for lung tumor tracking during EBRT. One unique feature of this model is using patient specific loading and material properties data which were obtained from 4D CT imaging data processed within an optimization framework. The primary objectives of developing the proposed model include 1) improving the accuracy of existing lung FE models, and 2) rendering the model adaptable for real-time tumor tracking by defining the diaphragm and trans-pulmonary pressure loading data such that they can be determined based on measurable chest surface motion data. The latter is highly essential as the goal of developing the proposed model is to utilize it in lung tumor tracking system being developed in our research laboratory for effective lung cancer EBRT. The lung biomechanical model serves as a core component of the system which determines the tumor location and its geometry throughout respiration before this data is fed to a robotic system driving a linear accelerator which changes the radiation beam orientation consistent with the tumor motion to achieve optimal EBRT outcome. The proposed lung biomechanics model involves two types of loading. The diaphragm motion related loading defined as prescribed displacement boundary conditions and the trans-

pulmonary pressure arising from chest muscle contraction and relaxation. These loading components were determined before treatment using 4D CT image data using optimization. The trans-pulmonary pressure curves obtained through optimization agree well with the pressure measurements reported in the literature. Another important feature of the proposed lung biomechanics model is its treatment of the incompressibility of the lung tissue. The model considers variable tissue incompressibility characterized by Poisson's ratio through various respiration phases. This is essential for studying the lung mechanics under breathing physiological conditions as the air content within the tissue varies substantially from the end exhalation phase (Phase 6 in Figure 3-8), where tissue incompressibility is maximum, to the end inhalation phase (Phase 10 in Figure 3-8), where tissue incompressibility is minimum. Poisson's ratio variations illustrated in Figure 3-8 are consistent with expected trend. In this work, the Poisson's ratio was assumed to be uniform throughout the lung volume. While this may be a good assumption in healthy lungs, a level of deviation from this uniformity assumption is expected with lung cancer patients or patients who have other lung disease such as Chronic Obstructive Pulmonary Disease (COPD). Especially in the latter, the Poisson's ratio is expected to be significantly heterogeneous. In such cases, the Poisson's ratio has to be treated as such, leading to a multi parameter optimization algorithm which can be solved to provide diagnostic information in addition to data pertaining to the lung tissue mechanical properties. The proposed model can also be used for modeling the left lung, however, the effects of heart motion should be considered. This can be accomplished by incorporating a heart motion model. Among other advantages of using the biomechanics approach for tumor tracking is its ability to compute the variable lung tumor geometry throughout respiration. This can be highly advantageous as the variable volume data can be used in conjunction with an advanced radiation dose distribution algorithm which takes into account tumor volume geometry variation during the course of EBRT. Results obtained from the proposed model indicate that the mean Dice similarity coefficient between the actual GTVs and their simulated counterparts ranges from 0.80 to 0.92. This range demonstrates reasonable accuracy of the proposed model in predicting the tumor volume geometry variation during respiration. This accuracy can be improved further by fine tuning the lung and tumor tissue hyperelastic properties, however,

this is not within the scope of the present work. Further quantitative assessment of the model was carried out by tracking the position of landmarks chosen within the lung volume including areas close to the tumor. Over all phases of respiration, the mean absolute error in the landmarks' 3D position is 1.74 ± 0.77 mm. The same was also carried out to assess the accuracy of the lung variable surfaces obtained through the proposed model. In the latter, the average Hausdorff surface-to-surface distance was calculated at 1.60 ± 0.17 mm. Biomechanical modeling of the lung has been tackled by a few other groups including Werner et al.²⁰, Al-Mayah et al.^{21,23,24}, and Villard et al.¹⁸, which use image-derived boundary conditions and contact modeling, and a recent study which uses an optimization framework to obtain the boundary conditions, i.e. pressure values²⁵. The mean absolute error per landmark reported by these groups ranges between 2.1 mm and 3.4 mm. These results are favorable and encourage conducting further studies for testing the proposed algorithm on larger data sets. As indicated earlier, one source of error in our model is the tissue mechanical properties which is expected to be heterogeneous in patients who suffer from lung disease. Despite assuming homogeneous tissue and assigning lung tissue hyperelastic parameters which are not patient specific, the quantitative results obtained in this study are quite favorable. In addition, strong agreement between the patterns of variation for optimized pressure curves and the experimental data reported in the literature³⁵, indicate that the proposed model can potentially be used for studying the physiology of breathing in normal and diseased subjects. Future work aimed at further development of the lung tumor tracking system using the proposed lung biomechanical model will involve demonstrating that both the diaphragm motion and pressure values can be obtained from chest surface motion data with high accuracy. In fact, our preliminary data generated for this purpose are very encouraging. As such, the proposed lung biomechanical model can be used during EBRT while its parameters can be updated from chest surface motion data, paving the way for effective tumor tracking necessary to optimize the EBRT outcome.

3.5 References

1. Murphy MJ. Tracking Moving Organs in Real Time. *Semin Radiat Oncol.* 2004;14(1):91-100. doi:10.1053/j.semradonc.2003.10.005.

2. Shirato H, Shimizu S, Kunieda T, et al. Physical aspects of a real-time tumor-tracking system for gated radiotherapy. *Int J Radiat Oncol Biol Phys*. 2000;48(4):1187-1195. doi:10.1016/S0360-3016(00)00748-3.
3. Chen Q-S, Weinhaus MS, Deibel FC, Ciezki JP, Macklis RM. Fluoroscopic study of tumor motion due to breathing: Facilitating precise radiation therapy for lung cancer patients. *Med Phys*. 2001;28(9):1850. doi:10.1118/1.1398037.
4. Keall PJ, Sawant A, Cho B, et al. Electromagnetic-guided dynamic multileaf collimator tracking enables motion management for intensity-modulated arc therapy. *Int J Radiat Oncol Biol Phys*. 2011;79(1):312-320. doi:10.1016/j.ijrobp.2010.03.011.
5. Keall PJ, Colvill E, O'Brien R, et al. The first clinical implementation of electromagnetic transponder-guided MLC tracking. *Med Phys*. 2014;41(2):20702. doi:10.1118/1.4862509.
6. Wu J, Ruan D, Cho B, et al. Electromagnetic detection and real-time DMMLC adaptation to target rotation during radiotherapy. *Int J Radiat Oncol Biol Phys*. 2012;82(3). doi:10.1016/j.ijrobp.2011.06.1958.
7. Sharp GC, Jiang SB, Shimizu S, Shirato H. Prediction of respiratory tumour motion for real-time image-guided radiotherapy. *Phys Med Biol*. 2004;49(3):425-440. doi:10.1088/0031-9155/49/3/006.
8. Schweikard A, Glosser G, Bodduluri M, Murphy MJ, Adler JR. Robotic motion compensation for respiratory movement during radiosurgery. *Comput Aided Surg*. 2000;5(4):263-277. doi:10.1002/1097-0150(2000)5:4<263::AID-IGS5>3.0.CO;2-2.
9. Achim Schweikard HS. Respiration tracking in radiosurgery. *Med Phys*. 2004;31(10):2738-2741. doi:10.1118/1.1774132.
10. Seiler PG, Blattmann H, Kirsch S, Muench RK, Schilling C. A novel tracking technique for the continuous precise measurement of tumour positions in

- conformal radiotherapy. *Phys Med Biol*. 2000;45(9):N103--10. doi:10.1088/0031-9155/45/9/402.
11. Balter JM, Wright JN, Newell LJ, et al. Accuracy of a wireless localization system for radiotherapy. *Int J Radiat Oncol Biol Phys*. 2005;61(3):933-937. doi:10.1016/j.ijrobp.2004.11.009.
 12. Bruce EN. Temporal variations in the pattern of breathing. *J Appl Physiol*. 1996;80:1079-1087.
 13. Ahn S, Yi B, Suh Y, et al. A feasibility study on the prediction of tumour location in the lung from skin motion. *Br J Radiol*. 2004;77(919):588-596. doi:10.1259/bjr/64800801.
 14. Tsunashima Y, Sakae T, Shioyama Y, et al. Correlation between the respiratory waveform measured using a respiratory sensor and 3D tumor motion in gated radiotherapy. *Int J Radiat Oncol Biol Phys*. 2004;60(3):951-958. doi:10.1016/j.ijrobp.2004.06.026.
 15. Weiss E, Wijesooriya K, Dill SV, Keall PJ. Tumor and normal tissue motion in the thorax during respiration: Analysis of volumetric and positional variations using 4D CT. *Int J Radiat Oncol Biol Phys*. 2007;67(1):296-307. doi:10.1016/j.ijrobp.2006.09.009.
 16. Decarlo D, Kaye J, Metaxas D, et al. Integrating Anatomy and Physiology for Behavior Modeling Integrating Anatomy and Physiology for Behavior Modeling Integrating Anatomy and Physiology for Behavior Modeling. *NI*. 1995. <http://repository.upenn.edu/hms%5Cnhttp://repository.upenn.edu/hms/76>.
 17. Zhang T, Orton NP, Mackie TR, Paliwal BR. Technical note: A novel boundary condition using contact elements for finite element based deformable image registration. *Med Phys*. 2004;31(9):2412-2415. doi:10.1118/1.1774131.
 18. Villard PF, Beuve M, Shariat B, Baudet V, Jaillet F. Simulation of lung behaviour with finite elements : Influence of bio-mechanical parameters. In: *Proceedings -*

Third International Conference on Medical Information Visualisation - BioMedical Visualisation, MediVis 2005. Vol 2005. ; 2005:9-14.
doi:10.1109/MEDIVIS.2005.15.

19. Eom J, Shi C, Xu XG, De S. Modeling respiratory motion for cancer radiation therapy based on patient-specific 4DCT data. In: *Lecture Notes in Computer Science (Including Subseries Lecture Notes in Artificial Intelligence and Lecture Notes in Bioinformatics)*. Vol 5762 LNCS. ; 2009:348-355. doi:10.1007/978-3-642-04271-3_43.
20. Werner R, Ehrhardt J, Schmidt R, Handels H. Patient-specific finite element modeling of respiratory lung motion using 4D CT image data. *Med Phys*. 2009;36(5):1500-1511. doi:10.1118/1.3101820.
21. Al-Mayah A, Moseley J, Velec M, Brock KK. Sliding characteristic and material compressibility of human lung: parametric study and verification. *Med Phys*. 2009;36(10):4625-4633. doi:10.1118/1.3218761.
22. Al-Mayah A, Moseley J, Velec M, Hunter S, Brock K. Deformable image registration of heterogeneous human lung incorporating the bronchial tree. *Med Phys*. 2010;37(9):4560-4571. doi:10.1118/1.3471020.
23. Al-Mayah A, Moseley J, Brock KK. Contact surface and material nonlinearity modeling of human lungs. *Phys Med Biol*. 2008;53(1):305-317. doi:10.1088/0031-9155/53/1/022.
24. Al-Mayah A, Moseley J, Velec M, Brock K. Effect of Friction and Material Compressibility on Deformable Modeling of Human Lung. In: *Biomedical Simulation SE - 11*. Vol 5104. ; 2008:98-106. doi:10.1007/978-3-540-70521-5_11.
25. Fuerst B, Mansi T, Carnis F, et al. Patient-Specific Biomechanical Model for the Prediction of Lung Motion From 4-D CT Images. *IEEE Trans Med Imaging*. 2015;34(2):599-607.
26. Isaksson M, Jalden J, Murphy MJ. On using an adaptive neural network to predict

- lung tumor motion during respiration for radiotherapy applications. *Med Phys*. 2005;32(12):3801-3809. doi:10.1118/1.2134958.
27. Hall JE, Guyton AC. *Guyton and Hall Textbook of Medical Physiology*. Vol 53.; 2011. doi:10.1017/CBO9781107415324.004.
 28. Karami E, Wang Y, Gaede S, Lee T-Y, Samani A. Anatomy-based algorithm for automatic segmentation of human diaphragm in noncontrast computed tomography images. *J Med Imaging*. 2016;3(4):46004. doi:10.1117/1.JMI.3.4.046004.
 29. Shirzadi Z, Sadeghi-Naini A, Samani A. Toward in vivo lung's tissue incompressibility characterization for tumor motion modeling in radiation therapy. *Med Phys*. 2013;40(5):51902. doi:10.1118/1.4798461.
 30. Zeng YJ, Yager D, Fung YC. Measurement of the mechanical properties of the human lung tissue. *J Biomech Eng*. 1987;109(2):169-174. doi:10.1115/1.3138661.
 31. Arnal J-M, Novotni D. Transpulmonary pressure measurement. *Crit Care Med*. 2014;44(1):R1. doi:10.1056/NEJMoa1011205.
 32. Chiumello D, Cressoni M, Colombo A, et al. The assessment of transpulmonary pressure in mechanically ventilated ARDS patients. *Intensive Care Med*. 2014;40(11):1670-1678. doi:10.1007/s00134-014-3415-4.
 33. Tawhai MH, Nash MP, Lin C-L, Hoffman E a. Supine and prone differences in regional lung density and pleural pressure gradients in the human lung with constant shape. *J Appl Physiol*. 2009;107:912-920. doi:10.1152/jappphysiol.00324.2009.
 34. Anderson J, Goplen C, Murray L, et al. Human respiratory mechanics demonstration model. *Adv Physiol Educ*. 2009;33(1):53-59. doi:10.1152/advan.90177.2008.
 35. Hall JE, Guyton AC. *Guyton and Hall Physiology Review*.; 2011. doi:10.1016/B978-1-4160-5452-8.00020-2.

Chapter 4 « Novel PCA-based Model of Human Diaphragm Motion Derived from 4D CT Images for Effective Tumor Motion Management »

4.1 Introduction

Image guided procedures aimed at diagnosis or medical intervention in the abdomen and thorax (e.g. lung External Beam Radiation Therapy (EBRT)) are very challenging, as they tend to involve moving anatomical targets (e.g. tumor) due to respiration. If the motion of such targets is known, data pertaining to this motion can be fed to robotic actuators and/or a multileaf collimator (MLC) that drive the therapy or diagnosis machine such that the intended anatomical feature is always targeted. Respiratory motion often lacks repeatability at different breath cycles, precluding the possibility of tumor motion prediction based solely on pre-treatment motion characterization. Moreover, in a medical intervention, it is often not feasible to utilize real-time image guidance for tumor tracking. For example, in medical interventional procedures involving the lung, CT imaging is the modality of choice. This modality cannot be used intraoperatively to avoid excessive radiation dose. Another technique was recently introduced which utilizes electromagnetic guidance for tumor tracking¹⁻³. While proven to be effective, this technique involves using beacon transponders placed through a needle or surgical procedure inside the tumor. An alternate effective and non-invasive solution to this problem is using expert systems to estimate the anatomical target motion/deformation during treatment, before it can be fed to the robotic actuators and/or MLC system. Such systems can be developed using motion computational modeling. These models attempt to estimate internal anatomical target motion/deformation intraoperatively using a surrogate measurable signal. They are developed using data measured before treatment and their corresponding target motion/deformation output data. Using these two sets of data, a machine learning or

physics based expert system can be developed to be used intraoperatively. The known output parameters are typically obtained from pre-treatment imaging data acquired at different phases of breathing cycle, while surrogate signal (input) parameters are obtained from data acquired at corresponding phases of the breathing cycle. The latter data are acquired using MR navigation, optical or electromagnetic tracking, spirometry, or real-time imaging. Various motion models are available in the literature where their differences pertain to the imaging modality and corresponding imaging data used in conjunction with the model, type of surrogate signal and modeling method. To develop an expert system that can be used intraoperatively as a function that inputs surrogate signal and outputs the internal target motion parameter, one of the two mathematical or biomechanical model approaches can be employed. Typically, in the mathematical model approach, mathematical functions are used to find the anatomical target motion as a function of the surrogate signal. Examples of such functions are polynomials⁴⁻¹⁰, B-splines¹¹⁻¹⁵ or Neural Networks^{16,17}. A comprehensive review on mathematical motion models in this context is presented by McClelland et al.¹⁸.

In contrast to the mathematical models, in the biomechanical model approach the underlying physics of tissue deformation is utilized for the anatomical target motion estimation. Biomechanical models used in this approach require data pertaining to tissue mechanical properties, lung geometry and loading. The latter includes forces exerted by the diaphragm to the bottom surface of the lungs in addition to thoracic pressure. One effective method used with this approach is the Finite Element Method (FEM) which has been used extensively for biomechanical simulation of the respiratory system¹⁹⁻²⁶. While biomechanical models offer great capability for motion modeling, little research has been conducted towards their utility in real-time lung tumor tracking.

Fundamental to any anatomical target respiratory motion is the diaphragm motion characteristics. As such, it is necessary that the diaphragm motion be characterized effectively before incorporation in the expert system. To achieve a compact mathematical form of the diaphragm motion, which is necessary for developing an effective expert system, we use principal component analysis (PCA). Given the diaphragm motion is complex, hence it requires characterization of the motion of many points on its surface for

proper discretized motion representation. Such a large data size cannot be easily expressed as a function of a small number of surrogate signals unless this data is represented in a compact way. In this context, PCA is a powerful tool to mathematically represent the data using a few parameters without significant loss of information. In 2009, McQuaid et al. presented a PCA-based diaphragm motion model obtained from gated CT images to correct the motion in PET images^{27,28}. Compared to the work of McQuaid et al., the proposed method is more rigorous in terms of positioning anatomical landmarks and obtaining their respective motion data. The proposed method is developed such that not only anatomical differences among subjects are accounted for but the motion can be characterized in all dimensions. It is noteworthy that the application of the PCA model is not limited to the proposed lung tumor tracking algorithm. In fact, most of the mathematical respiratory motion models use the diaphragm motion as surrogate to motion of various internal targets^{8,14,29–37}. For instance, Shechter et al.³⁸, Xu et al.³⁹ and Zhang et al.³⁷ obtain the model input signal, e.g. respiratory phase, from SI position of a single landmark located on the diaphragm visible in 2D ultrasonic, fluoroscopic and 4D CT images, respectively. Shechter et al. and Xu et al. used the diaphragm SI position as a surrogate to tumor motion while Zhang et al. used such a signal to obtain the respiratory phase. It is noteworthy that although the SI motions of a single landmark on the diaphragm can be used to find the respiratory phase, given the diaphragm's complex motion, it does not provide sufficient information to characterize the diaphragm motion. Hence it is inadequate for biomechanical or mathematical models aimed at mapping the chest surface motion into anatomical target motion. As such, for both groups of respiratory motion models using an optimal number of diaphragm landmarks is essential for accurate target motion management.

4.2 Materials and methods

4.2.1 Overview of expert system for lung tumor tracking

The expert system is being developed for lung tumor motion tracking in EBRT with highly effective tumor motion management. It is driven by a patient-specific lung biomechanical model developed using FEM which can estimate the current position/deformation of the

lung tumor throughout respiration. Unlike other systems, which can provide position estimates only, the system is designed to estimate both position and deformation. The latter makes it possible to estimate the tumor shape in real-time, paving the way for yet more effective radiation therapy by potentially using a combination of a robotic system to drive the Linear Accelerator for tumor tracking in addition to dynamic MLC for dynamic conformal radiotherapy. The lung geometry can be acquired using pretreatment CT image data. For real-time lung tumor position estimation, there are two main challenges in using such a model, namely, determining the lung boundary conditions and performing FE computations both in real-time. To address the second challenge, GPU programming or model reduction methods can be used. For real-time boundary conditions determination, we propose the framework illustrated in the block diagram of Figure 4-1. The essence of this framework is using the motion characteristics of an optimal number of external markers distributed optimally on the patient's chest as a surrogate for the boundary conditions. According to data presented by Vedam et al. and unpublished data generated in our laboratory, the diaphragm motion and pleural pressure are correlated with the chest surface motion⁴⁰. This implies that, in principle, by real-time tracking of the chest surface motion, the diaphragm motion can be also tracked by finding a proper function (e.g. neural network) that maps the chest surface motion parameters to the diaphragm motion. To develop such a function which can effectively input the chest surface motion data and output the diaphragm motion/deformation in real-time, an essential prerequisite is that the diaphragm motion be presented mathematically in a compact form. Developing and rigorously evaluating such a compact mathematical form using PCA is the focus of this work which is described in the following sections. Having such a mapping function, in turn, makes it possible to use highly efficient lung biomechanical models (e.g. developed using GPU) in conjunction with the mapping function for real-time tumor tracking during EBRT.

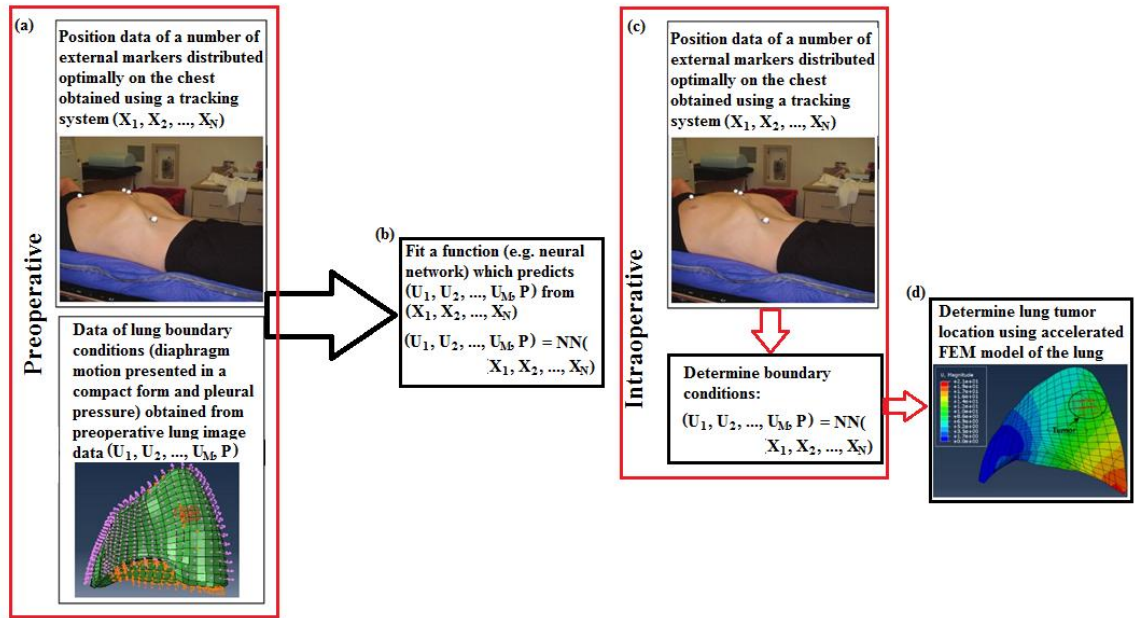


Figure 4–1 A block diagram of lung tumor tracking system. It involves four steps of (a) pre-treatment chest surface motion tracking and image based estimation of the lung boundary conditions. These boundary conditions include prescribed displacement boundary conditions of lung bottom surface which is equal to diaphragm surface displacements shown in orange and lung pleural pressure shown in purple. (b) Fitting a function (e.g. using neural network (NN) which maps chest surface data to lung boundary conditions. This fitting requires the diaphragm to be presented in a compact form. (c) Intra-treatment chest surface data acquisition and mapping to boundary conditions in real-time. (d) Calculating lung tumor position using an accelerated lung biomechanical model.

4.2.2 Data acquisition

In this study, 4D CT images of 10 subjects, each including 10 respiratory phases, were used to develop the PCA model. Five out of ten subjects were lung cancer patients. These patients were scanned using a 16-slice Philips Brilliance Big Bore CT scanner (Philips Medical Systems, Cleveland, USA) operating in helical mode. The scanning parameters are: 120 kVp and 400 mAs/slice for tube potential and current, respectively. The pitch of the couch depended on the patient's breathing period and was set to around 0.1. The intraslice pixel size of the data was set to vary from 0.98 mm to 1.29 mm while the slice thickness was set to 3 mm. The projection data were sorted using the Real-time Position ManagementTM (RPM) system (Varian Medical Systems, Inc., Palo Alto, CA, USA). The

rest of the data were obtained from POPI and DIR-LAB on-line data sets ^{15,41,42}. To avoid errors resulting from low image quality, we selected five subjects with minimum diaphragmatic motion artifacts from the two on-line data sets.

4.2.3 Image segmentation and registration

The modeling method proposed in this investigation consists of four steps: image segmentation, registration, and diaphragm gridding followed by PCA. Recently, we proposed an automatic diaphragm segmentation algorithm which can be used to segment the entire diaphragm⁴³. Given that the primary application of the proposed diaphragm motion model is lung biomechanical modeling and tumor tracking, we only model the diaphragm's dome which is in contact with the lung. Furthermore, since in our data sets the tumor was chosen to be in the right lung, in this study we developed the motion model for the diaphragm's right dome. As such, the diaphragm's right dome was segmented using Karami et al. diaphragm segmentation algorithm. Next, non-rigid registration using Free Form Deformation (FFD)⁴⁴ was used to track the diaphragm motion during breathing. Hereafter, displacements obtained from the FFD registration will be referred to as "true" displacements.

4.2.4 Landmark set selection using trans-finite interpolation

To use PCA for motion modeling, sufficient numbers of landmarks are required to be selected consistently on the segmented diaphragms of all subjects involved in the study. Ideally, distinct anatomical landmarks should be used for spatial characterization of the diaphragm. However, a sufficiently large number of such landmarks are not visible in the diaphragm's CT image. Due to anatomical differences between subjects, regular grids are not suitable for obtaining the landmarks in a consistent way. Therefore, we used trans-finite interpolation (TFI) to obtain a consistent landmark set to discretize the diaphragm dome. TFI involves two domains: the computational domain denoted by C and the physical domain denoted by P . As depicted in Figure 4-2, the computational domain is a regular grid of points where the points are mapped to the physical domain node set using blending functions given in Eq. 1 as follows. Details of this technique are well explained by Knupp and Steinberg ⁴⁵.

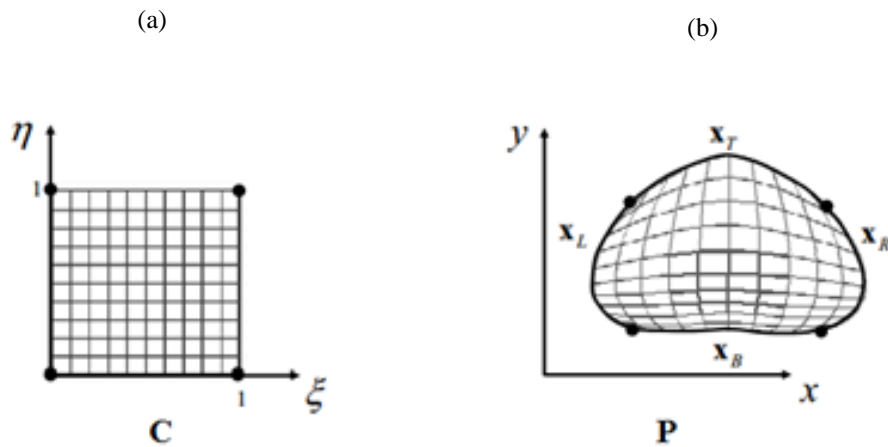


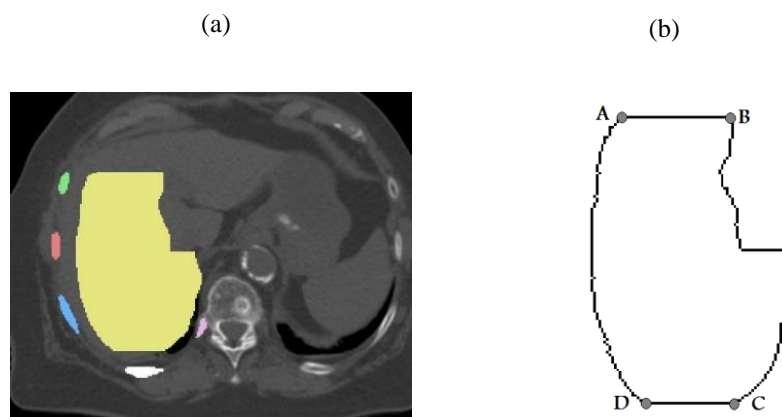
Figure 4-2 TFI domain meshing technique: (a) A 2D computational domain and (b) An example of a corresponding 2D physical domain.

$$\begin{aligned}
 \mathbf{X}(\xi, \eta) &= \begin{bmatrix} x(\xi, \eta) \\ y(\xi, \eta) \end{bmatrix} \\
 &= (1 - \eta)\mathbf{X}_B + \eta\mathbf{X}_R + (1 - \xi)\mathbf{X}_T + \xi\mathbf{X}_R - \xi\eta\mathbf{X}_{TR} - \xi(1 - \eta)\mathbf{X}_{BR} - \eta(1 - \xi)\mathbf{X}_{TL} \\
 &\quad - (1 - \xi)(1 - \eta)\mathbf{X}_{BL}
 \end{aligned} \tag{4-1}$$

In this equation, $(\xi, \eta) \in [0, 1]$ denote coordinates of points in C the computational domain and $\mathbf{X}_L, \mathbf{X}_R, \mathbf{X}_B$ and \mathbf{X}_T are left, right, bottom and top boundaries and $\mathbf{X}_{BL}, \mathbf{X}_{BR}, \mathbf{X}_{TL}$ and \mathbf{X}_{TR} are their intersection points, respectively in the physical domain. Using this equation, the closed shape P can be discretized by defining a $N \times N$ computational grid $X_c = (i/(N-1), j/(N-1))$, $i, j, k = 0, 1, \dots, N-1$ and mapping it into a set of points defining the physical domain P .

To sample the diaphragm dome surfaces consistently among the subjects using TFI, we first obtained their 2D projections on the axial plane as shown in Figure 4-3 (a). As displayed in Figure 4-3 (b), the four points A, B, C and D were used to represent the physical domain corner points and divide the domain boundary into $\mathbf{X}_B, \mathbf{X}_L, \mathbf{X}_T$ and \mathbf{X}_R

segments required for the TFI method. Also, to further account for anatomical differences between the patients and to ensure landmarks consistency in all the subjects, the relative position of the diaphragm to the ribs was considered in the process of sampling. For this purpose, as shown in Figure 4-3 (a), the 2D projection for each subject was overlaid on an axial slice of the subject's corresponding CT image, which encompassed the spine and the 11th rib. Next, the 7th to 11th ribs were segmented in the same axial slice and the centroid of these ribs were connected to the centroid of the dome by lines as illustrated in Figure 4-3 (c). Hence, the distinct diaphragm vertices a , b , c , d and e which are shown in Figure 4-3 (c) were identified. In addition to these vertices, point f can be easily identified as an additional vertex; hence points a , b , c , d , e and f in addition to the corner points A, B, C and D will form the primary distinct vertices on the 2D projected area outline. To achieve a denser landmark sampling, more vertices were identified on the outline systematically by finding points to bridge the segments Aa, ab, bc, cD, Dd, dC, Ce, ef, fB and BA. These points were found by further segmenting each segment using equal angles with the centroid \mathbf{o} as the angle vertex. For example, the outline segment ab was further segmented by dividing the angle $\angle \mathbf{aob}$ into equal angular intervals. With this outline discretization scheme, X_B and X_T segments were presented by 6 vertices while X_L and X_R segments were presented by 16 vertices. These points were used in Eq. (1) to generate the internal landmark points in the diaphragm's 2D projected area. The output set of landmarks of one right diaphragm is illustrated in Figure 4-3 (d).



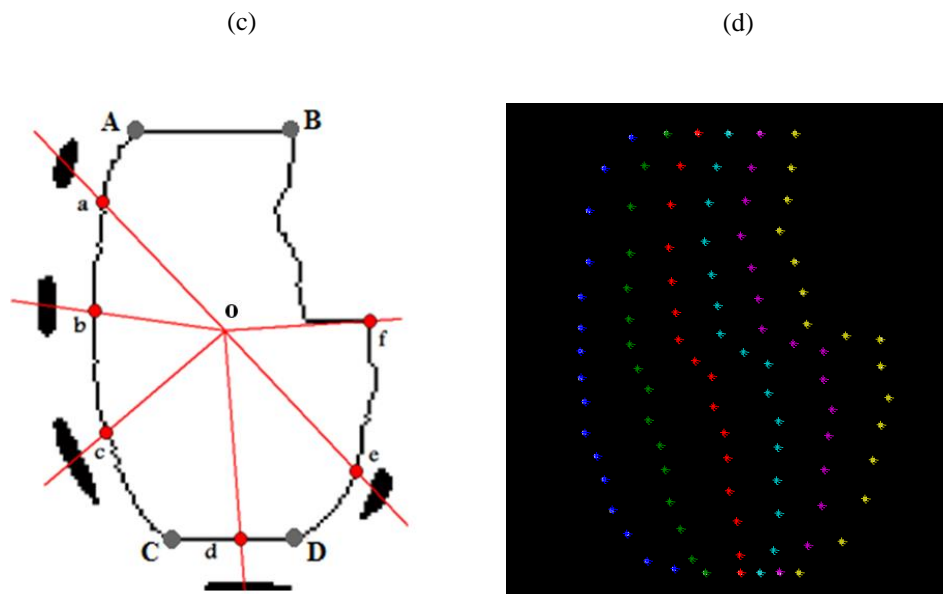


Figure 4–3 (a) 2D projection of the diaphragm's dome in an axial plane intersecting with segmented 7th to 11th ribs, (b) Four corners points, A,B, C and D were used to partition the boundary of the dome, (c) Using the 7th to 11th ribs to obtain additional anatomical landmarks for TFI and (d) The final TFI grid with $6 \times 16 = 96$ landmarks.

The total number of TFI-generated landmarks for each subject was $6 \times 16 = 96$. To prepare the data for principal component analysis, both magnitude and duration of respiratory motion were normalized between 0 and 1 for all the subjects. This normalization was necessary for landmark consistency, both spatially and temporally. For each subject, a 6×16 matrix corresponding to each displacement component was formed for each phase of respiration. With 10 subjects involved in this study, $10 \times 3 = 30$ such matrices were formed for each phase of respiration to contain displacement data in the 3 directions of superior-inferior (SI), anterior-posterior (AP) and right-left (RL).

4.2.5 Principal component analysis

The next step for efficient modeling of the diaphragm motion is to use PCA. PCA is a statistical procedure that can be used for mathematically presenting a set of observations in a compact form. This is accomplished by obtaining the principal components which contain the fundamental information of the observations' common features. Given an

observation matrix X of dimension $N \times P$ where each row represents a different data point (x), using PCA each data point x can be approximated by ⁴⁶:

$$x = \bar{x} + Qb, \quad (4 - 2)$$

where $Q = (q_1, q_2, \dots, q_M)$ is the matrix of the first M ($M < P$) eigenvectors of the covariance matrix of X and $b = (b_1, b_2, \dots, b_M)^T$ is a vector of weights. To obtain the compact form of the diaphragm motion, PCA was performed on displacement matrices of each respiratory phase for SI, AP and RL directions.

4.2.6 Validation

4.2.6.1 True and PCA model based displacements agreement

To evaluate the performance of the diaphragm PCA model, we first used the leave-out one method, where 9 out of 10 subjects were used to train the PCA model and the 10th subject was used for performance validation. This was repeated for all the 10 subjects. After performing the leave-out one method and obtaining the model generated displacement fields for all the 10 subjects, the average error per landmark was calculated for each patient in LR, AP and SI directions. In addition to calculating the average error per landmark, the overall agreement between the model generated displacement fields and their true counterparts were assessed by plotting the Bland-Altman plot for all the subjects.

4.2.6.2 PCA model based displacements error propagation in lung biomechanical model

Since the primary objective of this study is geared towards lung biomechanical modeling, the diaphragm PCA model was incorporated into a previously developed lung FE model ^{47,48}. The lung FE model proposed by Karami et al. is a model developed based on 4D CT images of lung cancer patients⁴⁸. In that FE model, the boundary conditions are diaphragm motion and pleural pressure. To test the performance of the proposed PCA model and assess its corresponding error propagation in biomechanical modeling, lung FE models of three lung cancer patients (H1, H2 and P2) were developed. For each lung FE model, the tumor displacement was calculated at the end inhalation phase relative to the end exhalation phase of respiration as a reference, using the true diaphragm displacement values or PCA model-generated displacement values as prescribed boundary conditions. These

displacements were compared to their displacement counterparts obtained from the true diaphragm displacements used as boundary conditions.

4.3 RESULTS

The segmentation result of one of the cases is shown in Figure 4-4 where two views of a segmented right dome of the diaphragm are illustrated. This figure illustrates coronal and sagittal views of the diaphragm overlaid on their respective CT images where the diaphragm and bottom surface of the lung are in close contact, indicating the good quality of segmentation.

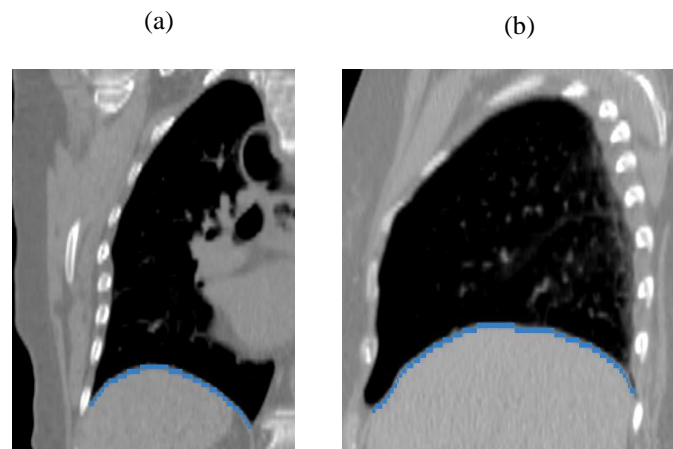


Figure 4–4 Segmentation results for a diaphragm’s right dome, (a) Coronal view and (b) Sagittal view.

4.3.1 Actual and PCA model based displacements comparison

PCA analysis indicated that the diaphragmatic motion in each direction can be represented highly accurately using only the 7 largest eigen vectors as they include 98%, 97% and 96% of the data information for the SI, AP and LR directions, respectively. To evaluate the model performance, the “true” and model-generated displacement fields were calculated for all the subjects using leave-out one method. To illustrate the errors between the “true” and model-generated landmark positions, three groups of landmarks were selected for two randomly selected subjects. The motion patterns and errors for other subjects follow a similar trend. The three selected groups of landmarks are marked in Figure 4-5 with circles.

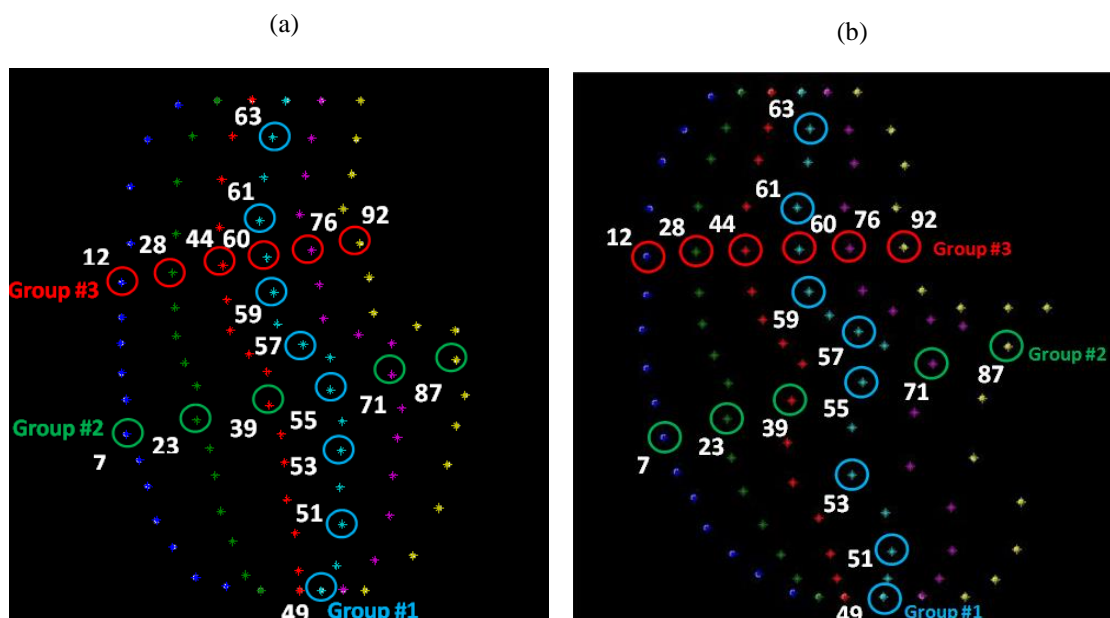
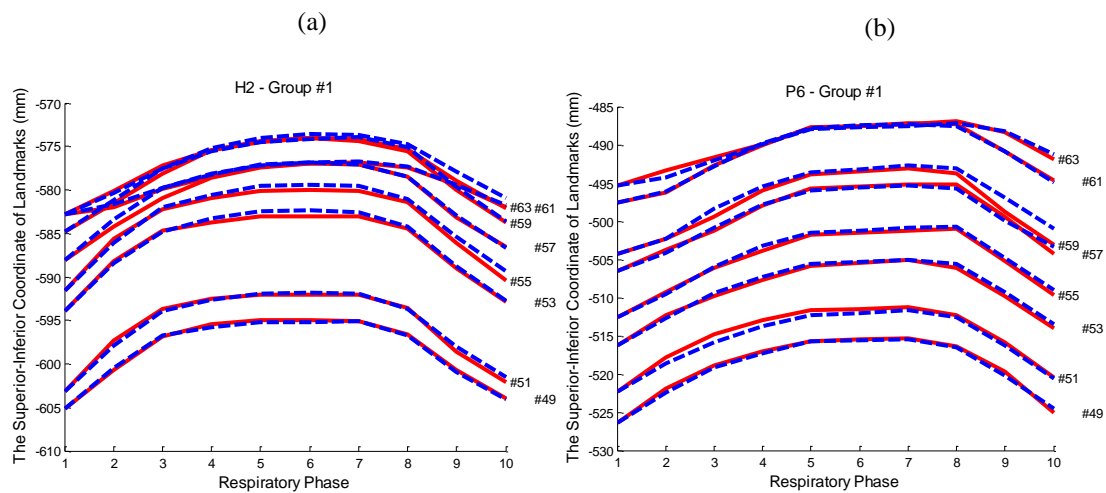


Figure 4–5 Landmark selection for (a) patient H2 and (b) patient P6. Points shown with ‘+’ are generated by the TFI method. A subset of these points (shown with ‘o’) are selected for results comparison.



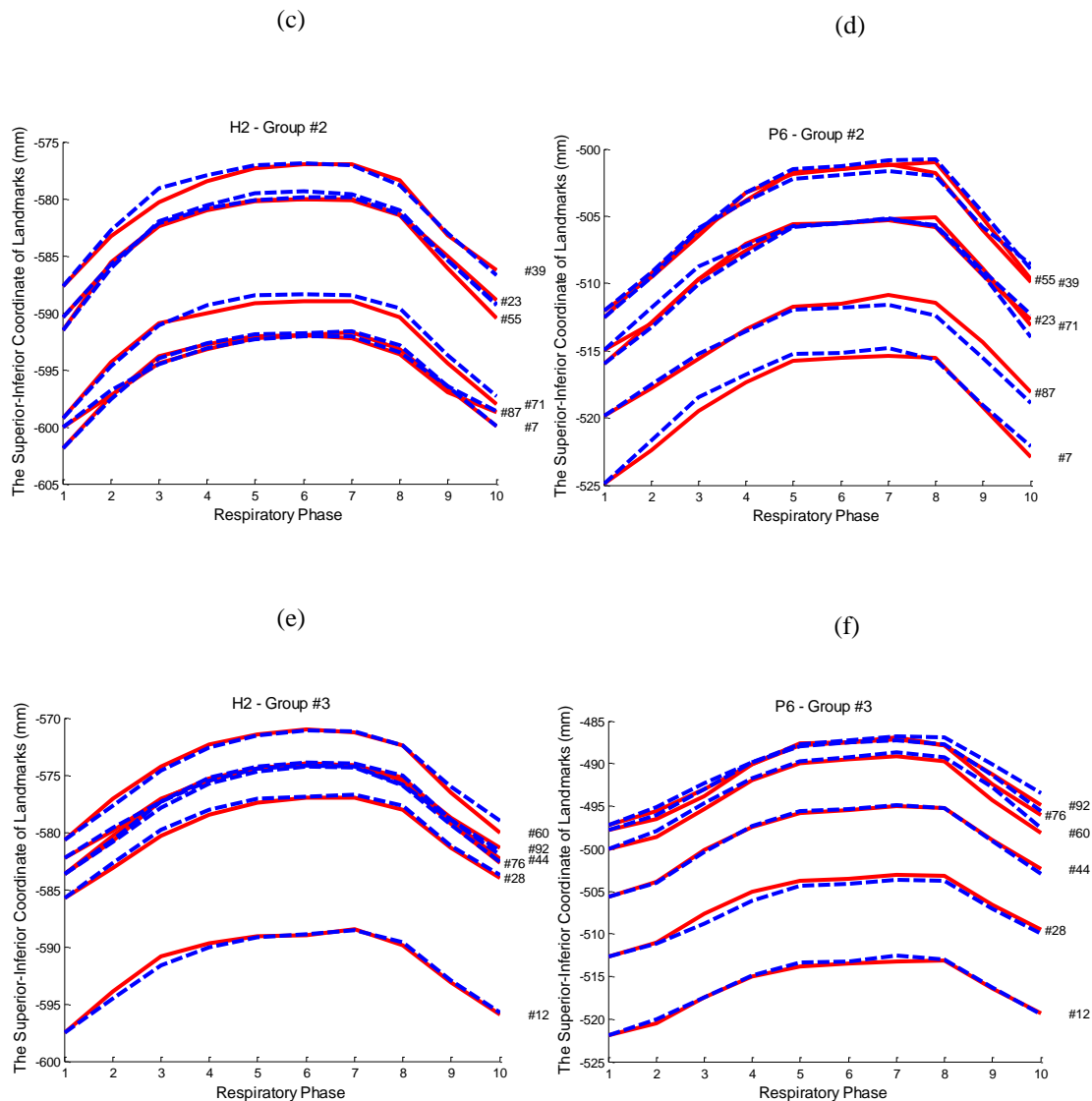
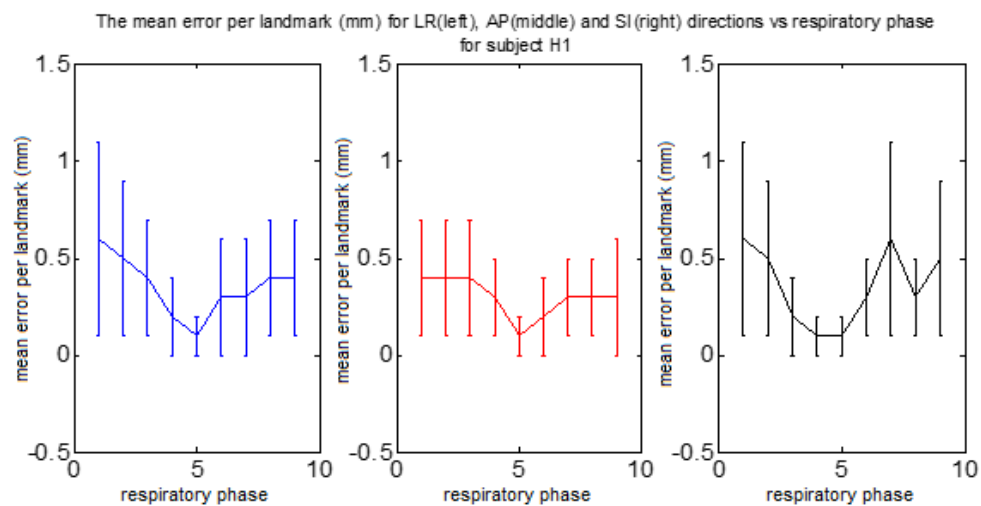


Figure 4-6 “True” (solid line) and model generated (dashed line) SI positions of Group #1 (a and b), Group #2 (c and d) and Group #3 (e and f) of landmarks.

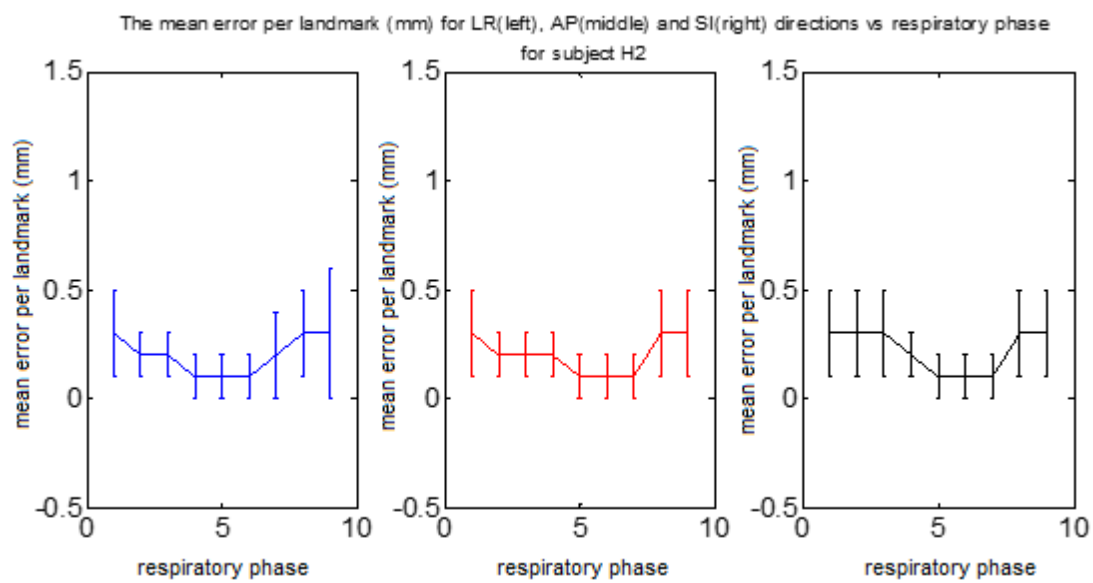
The first group of landmarks represent an AP profile along the diaphragm while the second and third group of landmarks represent two LR profiles along the diaphragm. These landmarks were used to assess the model performance for different locations on the diaphragm. The “true” and model-generated positions of the selected landmarks are shown in Figure 4-6. While the displacements shown in Figure 4-6 are in the SI direction, results of motion patterns in other directions (not shown) show a similar trend. As shown in this

figure, not only the “true” and model-generated landmark positions match very well, but also there are no significant error differences among different locations on the diaphragm. As shown in Figure 4-6, the errors mainly occur close to the end inhalation phase, i.e. beginning and end of the displacement curves. This may be attributed to the smoothing nature of PCA and the fact that the two ends of the curves are less smooth compared to the middle part. Our observations from all subjects indicate that another important source of error is anatomical differences between patients which lead to minor inconsistencies in gridding the diaphragm dome using the TFI technique. As shown in Figure 4-5, while overall the TFI technique provides consistent landmarks especially in the axial plane, some of the landmarks lack strong spatial consistency in the SI direction. Examples of such landmarks are landmarks #60, #76 and #92 marked in Figure 4-5 (a) and 4-5 (b). Figures 4-6 (e) and 4-6 (f) which show the relative SI positions of these landmarks confirm that the selected landmarks for patients P6 and H2 are not highly consistent. For instance, landmark#92 is located inferior to landmark #60 for patient H2 while it is located slightly superior to landmark #60 for patient P6. Because of this inconsistency, qualitative comparison of results shown in Figures 4-6 (e) and 4-6 (f) show that errors associated with landmarks #60 and #92 are higher compared to other landmarks as their respective “true” and model-generated displacement curves are further apart. The same argument can be made about landmarks #55 and #23. On the other hand, when the landmarks are highly consistent, e.g. landmarks #12, #28, #44, #49, #51 and #53, the actual and model-generated landmark positions match almost perfectly. The average errors per landmark between the “true” and model-generated displacement values are reported in Figure 4-7 for LR, AP and SI directions. This figure includes data pertaining to four subject examples including H2 and P2 which correspond to the best and worst cases, respectively. As shown in this figure, except for one subject (patient P2), the mean error per landmark is less than 1 mm for all phases of respiration and in all directions. Data pertaining to other subjects show similar values and variations.

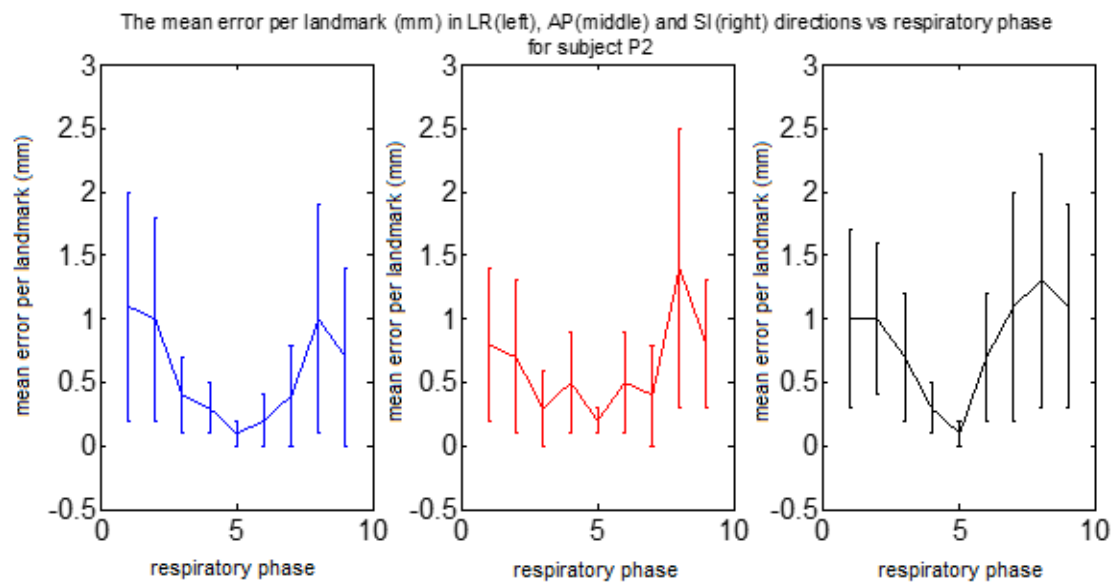
(a)



(b)



(c)



(d)

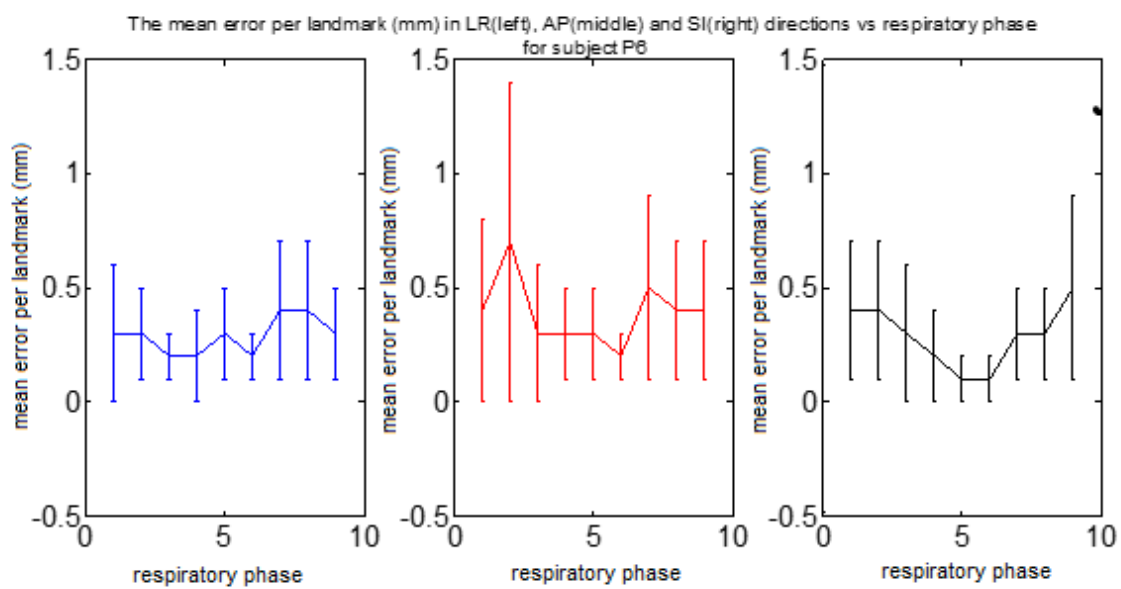
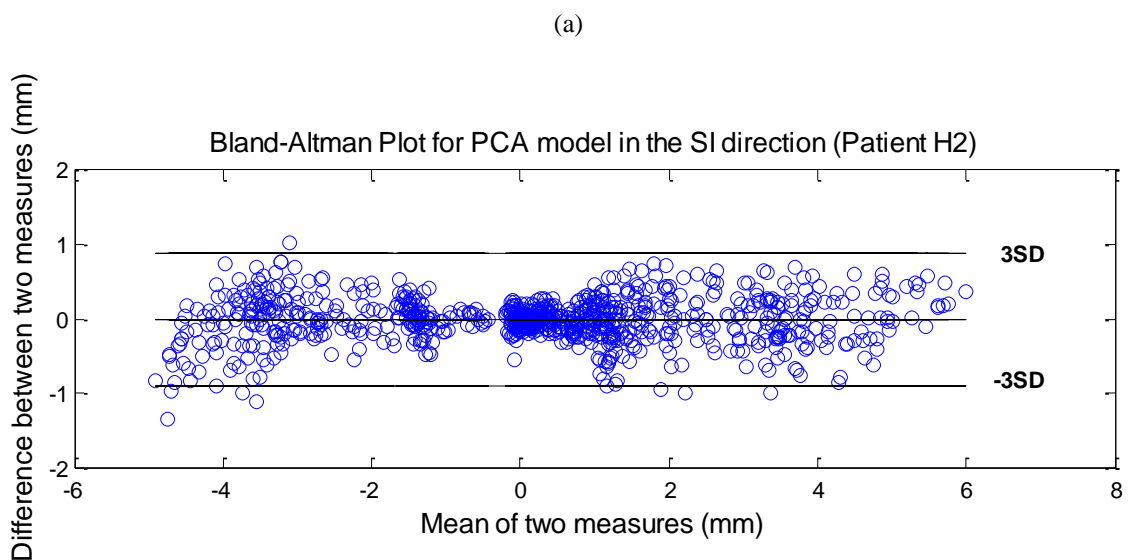


Figure 4–7 The mean error per landmark (mm) in the LR(left), AP(middle) and SI(right) directions versus respiratory phase for subjects (a) H1, (b) H2, (c) P2, and (d) P6.

Figures 4-8 (a) and 4-8 (b) illustrate Bland-Altman plots for subjects H2 and P6. These plots show good agreement between the “true” and model-generated displacements for all the landmarks in these subjects. As shown in these figures, except for very few outliers, the displacement error for most of the landmarks is less than 1.5mm. The results indicate that even the outliers did not exceed 2.0 mm. A similar trend was observed for other subjects. Similar to what have been discussed about errors associated with individual landmarks in Figure 4-6, Figure 4-8 shows that, in general, errors are higher for end inhalation phase of respiration, i.e. two ends of the displacement curves. It can be seen in Figure 4-6 that the output of PCA was smoother than the actual displacement curve, leading to the observed differences between the two curves. It is noteworthy that natural phenomena such as breathing are smooth, indicating that PCA model-generated displacement values might be closer to reality compared to displacements obtained from deformable image registration, which is regarded as “true” displacements.



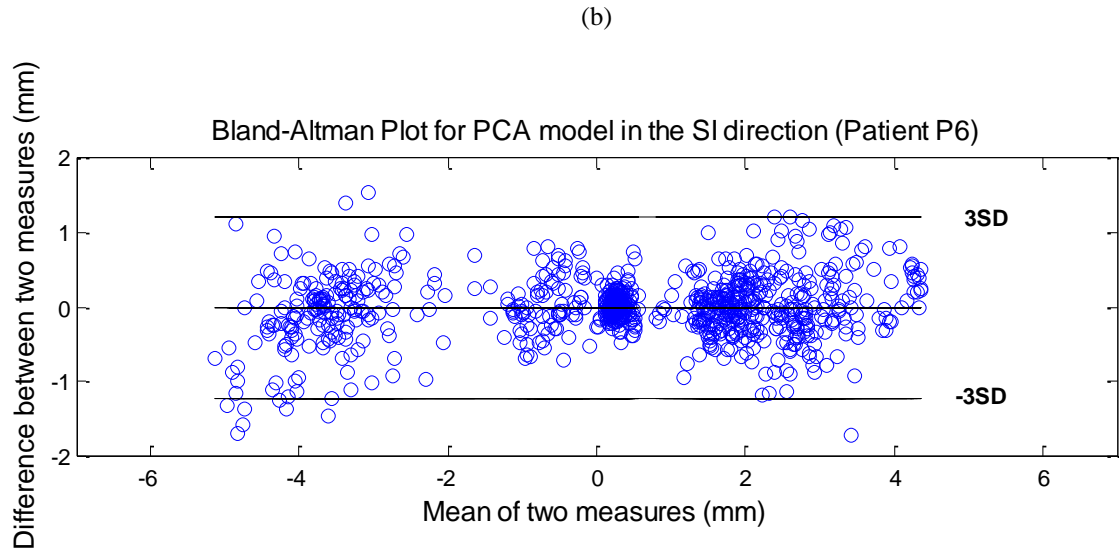


Figure 4–8 The Bland-Altman plots for subjects (a) H2 and (b) P6 indicating favorable agreement between “true” and model generated displacement fields.

4.3.2 Biomechanics based tumor tracking results using the “true” and PCA model based diaphragm displacements

Figure 4-9 illustrates the FE model of patient H1. This figure illustrates a 3D model of the patient’s lung at end exhalation (Figure 4-9 (a)). Corresponding displacement magnitude distribution developed through end exhalation to end inhalation is also shown (Figure 4-9 (b)). The figure also shows two sections of the displacement magnitude distribution through the tumor. These sections indicate that the tumor did not lead to significant disturbances in the displacement field.

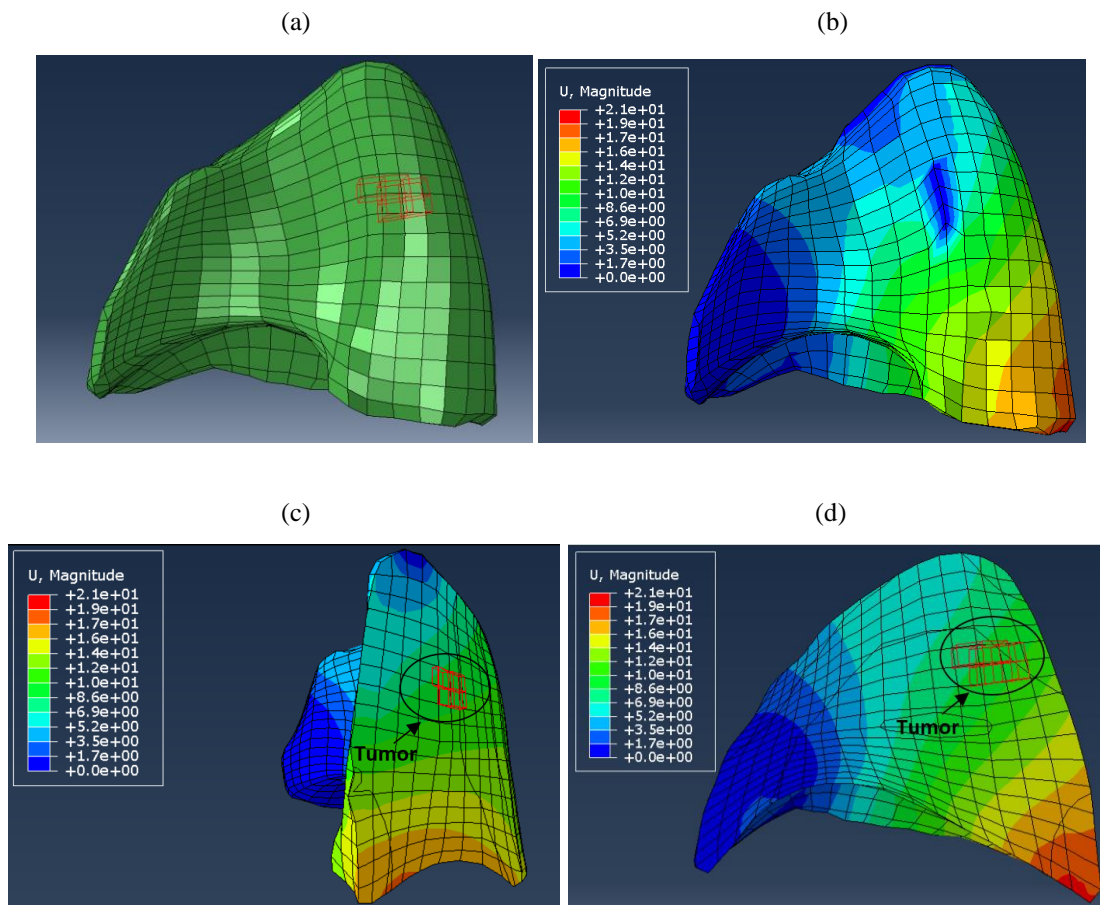


Figure 4-9 (a) 3D FE model of the lung at end exhalation phase; (b) 3D displacement distribution superimposed on the end exhalation phase; (c) a sagittal section of the displacement distribution through the tumor and (d) a coronal section of the displacement distribution through the tumor.

Table 4-1 lists the tumor displacements in SI, AP and RL directions calculated using the PCA model-generated boundary conditions and the “true” boundary conditions in conjunction with the lung FE model. According to this table, the mean displacement error along the SI, AP and RL directions was less than 0.5 mm. This indicates that the proposed diaphragm model’s error propagation in typical biomechanical models does not impact the accuracy in tumor motion prediction significantly.

H2	H1	P2	Mean \pm SD
----	----	----	---------------

Displacement of tumor centroid from “true” motion data (mm)	[0.21, 1.76, -7.46]	[-1.06, 4.99, -10.39]	[-12.06, -5.00, -14.23]	[-4.30, 0.58, -10.69]
Displacement of tumor centroid from model-generated motion data (mm)	[1.11, 1.77, -7.39]	[-1.23, 4.22, -9.73]	[-11.98, -4.95, -14.11]	[-4.03, 0.35, -10.41]
Error (mm)	[0.90, 0.01, 0.07]	[0.18, 0.77, 0.66]	[0.07, 0.04, 0.12]	[0.38±0.45, 0.27±0.43, 0.28±0.33]

Table 4-1 Tumor displacement values in LR, AP and SI directions obtained from “true” diaphragm motion data and the PCA model-generated diaphragm displacement field. The displacement errors resulting from the two different boundary conditions and the Mean±SD values are also provided.

4.4 Discussion and conclusions

A highly accurate model, developed using PCA was proposed for diaphragm motion characterization. This model was developed to be used as a major component of an expert system being developed for lung tumor motion management in EBRT. The expert system is designed to predict lung tumor motion/deformation during treatment using surrogate signals of the patient’s chest surface motion. The premise of the expert system is the known correlation between the chest surface motion, which can be measured non-invasively during EBRT, and diaphragm motion. The latter motion is used as prescribed displacement boundary conditions for a previously developed lung biomechanical model used in the expert system. In addition to biomechanical applications, diaphragm motion modeling can be used in a group of respiratory motion models which use diaphragm motion as surrogate to other anatomical target motions^{8,30–39,49}. In the proposed model, we employed the TFI technique to select consistent diaphragm landmarks for all subjects involved in the study. This is extremely important to ensure diaphragm local region anatomical consistency among the subjects. Unlike existing methods, the proposed model is 3D, while motion data was obtained through non-rigid registration. Both qualitative and quantitative results

indicate favorable agreement between “true” and model-generated diaphragm displacement fields. In the results section, we showed that one source of error in the proposed model is the few inconsistencies that occur in landmark selection. Errors occurring due to inconsistency in selecting the landmarks can be compensated for by using more rigorous methods for landmark selection. For example, it is possible to include more anatomical information into the process of Transfinite Interpolation to achieve higher consistency. Alternatively, 2D TFI used in this study can be replaced with 3D TFI to compensate for errors resulting from inconsistent landmark selection. However, we showed that such errors did not affect the biomechanics based tumor tracking results significantly.

To further evaluate the PCA model, a previously developed lung FE model was used to calculate tumor motion in three patients where the “true” diaphragm motion and the PCA model based motion were used as the boundary conditions in the lung biomechanical model. Comparison of results obtained from these two sets of diaphragm motion indicated that the mean errors in tumor motion estimation for the three patients were 0.38mm, 0.27mm and 0.29mm in RL, AP and SI directions, respectively. This confirms that error propagation from the proposed PCA model into typical biomechanical lung model had insignificant impact on the biomechanical model’s overall accuracy. It is noteworthy that all subjects enrolled in this study were either lung cancer or COPD patients. Cancer and COPD affect functionality of the diaphragm differently, while the number of subjects in each category in this study was not sufficient for capturing all those motion patterns. As such, better results are expected by incorporating more subjects in the process of developing the PCA model. To compare the proposed method to the model proposed by McQuaid et al.²⁸ for diaphragm SI motion, we calculated the mean error per landmark for all patients using leave-one out scheme. Using the model proposed in this study, the mean \pm SD error per landmark in the SI direction ranged between 0.1 ± 0.1 mm and 1.3 ± 1.0 mm for the 10 patients. This is a significant improvement to the quantitative results of McQuaid et al. who reported for two patients an error ranging between 3.2 ± 2.4 mm and 5.1 ± 4.4 mm. Overall, the results of the proposed method show promising accuracy to characterize the motion of the diaphragm and subsequently to predict lung tumor motion.

All steps involved in the model development, including segmentation, registration and landmark selection are fully automatic. As such, the proposed model has a good potential to be incorporated into expert system frameworks aimed at studying and modeling respiratory motion for various biomedical applications. One example of such framework is the biomechanics-based real-time lung tumor tracking system described in this paper which aims at more effective lung EBRT systems.

4.5 References

1. Keall PJ, Sawant A, Cho B, et al. Electromagnetic-guided dynamic multileaf collimator tracking enables motion management for intensity-modulated arc therapy. *Int J Radiat Oncol Biol Phys*. 2011;79(1):312-320. doi:10.1016/j.ijrobp.2010.03.011.
2. Wu J, Ruan D, Cho B, et al. Electromagnetic detection and real-time DMLC adaptation to target rotation during radiotherapy. *Int J Radiat Oncol Biol Phys*. 2012;82(3). doi:10.1016/j.ijrobp.2011.06.1958.
3. Keall PJ, Colvill E, O'Brien R, et al. The first clinical implementation of electromagnetic transponder-guided MLC tracking. *Med Phys*. 2014;41(2):20702. doi:10.1118/1.4862509.
4. Ernst F, Bruder R, Schlaefler A, Schweikard A. Correlation between external and internal respiratory motion: A validation study. *Int J Comput Assist Radiol Surg*. 2012;7(3):483-492. doi:10.1007/s11548-011-0653-6.
5. Hoogeman M, Prévost JB, Nuyttens J, Pöll J, Levendag P, Heijmen B. Clinical Accuracy of the Respiratory Tumor Tracking System of the CyberKnife: Assessment by Analysis of Log Files. *Int J Radiat Oncol Biol Phys*. 2009;74(1):297-303. doi:10.1016/j.ijrobp.2008.12.041.
6. King AP, Rhode KS, Razavi RS, Schaeffter TR. An adaptive and predictive respiratory motion model for image-guided interventions: Theory and first clinical application. *IEEE Trans Med Imaging*. 2009;28(12):2020-2032. doi:10.1109/TMI.2009.2028022.
7. McClelland JR, Hughes S, Modat M, et al. Inter-fraction variations in respiratory motion models. *Phys Med Biol*. 2011;56(1):251-272. doi:10.1088/0031-9155/56/1/015.

8. Nehrke K, Börnert P, Manke D, Böck JC. Free-breathing cardiac MR imaging: study of implications of respiratory motion--initial results. *Radiology*. 2001;220(3):810-815. doi:10.1148/radiol.2203010132.
9. Ruan D, Fessler JA, Balter JM, Berbeco RI, Nishioka S, Shirato H. Inference of hysteretic respiratory tumor motion from external surrogates: a state augmentation approach. *Phys Med Biol*. 2008;53(11):2923-2936. doi:10.1088/0031-9155/53/11/011.
10. Seppenwoolde Y, Berbeco RI, Nishioka S, Shirato H, Heijmen B. Accuracy of tumor motion compensation algorithm from a robotic respiratory tracking system: a simulation study. *Med Phys*. 2007;34(7):2774-2784. doi:10.1118/1.2739811.
11. Buerger C, Clough RE, King AP, Schaeffter T, Prieto C. Nonrigid motion modeling of the liver from 3-D undersampled self-gated golden-radial phase encoded MRI. *IEEE Trans Med Imaging*. 2012;31(3):805-815. doi:10.1109/TMI.2011.2181997.
12. Colgan R, McClelland J, McQuaid D, et al. Planning lung radiotherapy using 4D CT data and a motion model. *Phys Med Biol*. 2008;53(20):5815-5830. doi:10.1088/0031-9155/53/20/017.
13. McClelland JR, Blackall JM, Tarte S, et al. A continuous 4D motion model from multiple respiratory cycles for use in lung radiotherapy. *Med Phys*. 2006;33(9):3348-3358. doi:10.1118/1.2222079.
14. Shechter G, Shechter B, Resar JR, Beyar R. Prospective motion correction of X-ray images for coronary interventions. *IEEE Trans Med Imaging*. 2005;24(4):441-450. doi:10.1109/TMI.2004.839679.
15. Vandemeulebroucke J, Rit S, Kybic J, Clarysse P, Sarrut D. Spatiotemporal motion estimation for respiratory-correlated imaging of the lungs. *Med Phys*. 2011;38(1):166-178. doi:10.1118/1.3523619.
16. Isaksson M, Jalden J, Murphy MJ. On using an adaptive neural network to predict lung tumor motion during respiration for radiotherapy applications. *Med Phys*. 2005;32(12):3801-3809. doi:10.1118/1.2134958.
17. Torshabi AE, Pella A, Riboldi M, Baroni G. Targeting accuracy in real-time tumor tracking via external surrogates: a comparative study. *Technol Cancer Res Treat*.

- 2010;9(6):551-562. <http://www.ncbi.nlm.nih.gov/pubmed/21070077>.
18. McClelland JR, Hawkes DJ, Schaeffter T, King AP. Respiratory motion models: A review. *Med Image Anal.* 2013;17(1):19-42. doi:10.1016/j.media.2012.09.005.
 19. Werner R, Ehrhardt J, Schmidt R, Handels H. Patient-specific finite element modeling of respiratory lung motion using 4D CT image data. *Med Phys.* 2009;36(5):1500-1511. doi:10.1118/1.3101820.
 20. Zhang T, Orton NP, Mackie TR, Paliwal BR. Technical note: A novel boundary condition using contact elements for finite element based deformable image registration. *Med Phys.* 2004;31(9):2412-2415. doi:10.1118/1.1774131.
 21. Eom J, Shi C, Xu XG, De S. Modeling respiratory motion for cancer radiation therapy based on patient-specific 4DCT data. In: *Lecture Notes in Computer Science (Including Subseries Lecture Notes in Artificial Intelligence and Lecture Notes in Bioinformatics)*. Vol 5762 LNCS. ; 2009:348-355. doi:10.1007/978-3-642-04271-3_43.
 22. Al-Mayah A, Moseley J, Brock KK. Contact surface and material nonlinearity modeling of human lungs. *Phys Med Biol.* 2008;53(1):305-317. doi:10.1088/0031-9155/53/1/022.
 23. Al-Mayah A, Moseley J, Velec M, Brock KK. Sliding characteristic and material compressibility of human lung: parametric study and verification. *Med Phys.* 2009;36(10):4625-4633. doi:10.1118/1.3218761.
 24. Al-Mayah A, Moseley J, Velec M, Hunter S, Brock K. Deformable image registration of heterogeneous human lung incorporating the bronchial tree. *Med Phys.* 2010;37(9):4560-4571. doi:10.1118/1.3471020.
 25. Al-Mayah A, Moseley J, Velec M, Brock K. Effect of Friction and Material Compressibility on Deformable Modeling of Human Lung. In: *Biomedical Simulation SE - 11*. Vol 5104. ; 2008:98-106. doi:10.1007/978-3-540-70521-5_11.
 26. Fuerst B, Mansi T, Carnis F, et al. Patient-Specific Biomechanical Model for the Prediction of Lung Motion From 4-D CT Images. *IEEE Trans Med Imaging.* 2015;34(2):599-607.
 27. McQuaid SJ, Lambrou T, Cunningham VJ, Bettinardi V, Gilardi MC, Hutton BF. The application of a statistical shape model to diaphragm tracking in respiratory-gated cardiac

- PET images. *Proc IEEE*. 2009;97(12):2039-2052. doi:10.1109/JPROC.2009.2031844.
28. McQuaid SJ, Lambrou T, Hutton BF. A novel method for incorporating respiratory-matched attenuation correction in the motion correction of cardiac PET-CT studies. *Phys Med Biol*. 2011;56(10):2903-2915. doi:10.1088/0031-9155/56/10/002.
 29. Blackall J, King A, Penney G, et al. A Statistical Model of Respiratory Motion and Deformation of the Liver. *Med Image Comput Comput Interv MICCAI 2001*. 2001;2208:1338-1340. doi:10.1007/3-540-45468-3.
 30. Buliev IG, Badea CT, Kolitsi Z, Pallikarakis N. Estimation of the heart respiratory motion with applications for cone beam computed tomography imaging: a simulation study. *Inf Technol Biomed IEEE Trans*. 2003;7(4):404-411. doi:10.1109/TITB.2003.821336.
 31. Cerviño LI, Chao AKY, Sandhu A, Jiang SB. The diaphragm as an anatomic surrogate for lung tumor motion. *Phys Med Biol*. 2009;54:3529-3541. doi:10.1088/0031-9155/54/11/017.
 32. Jahnke C, Paetsch I, Nehrke K, et al. Rapid and complete coronary arterial tree visualization with magnetic resonance imaging: Feasibility and diagnostic performance. *Eur Heart J*. 2005;26(21):2313-2319. doi:10.1093/eurheartj/ehi391.
 33. King AP, Rhode KS, Ma Y, et al. Registering preprocedure volumetric images with intraprocedure 3-D ultrasound using an ultrasound imaging model. *IEEE Trans Med Imaging*. 2010;29(3):924-937. doi:10.1109/TMI.2010.2040189.
 34. Manke D, Rensch P, Nehrke K, B??rnert P, D??ssel O. Model evaluation and calibration for prospective respiratory motion correction in coronary MR angiography based on 3-D image registration. *IEEE Trans Med Imaging*. 2002;21(9):1132-1141. doi:10.1109/TMI.2002.804428.
 35. Rijkhorst EJ, Rivens I, Ter Haar G, Hawkes D, Barratt D. Effects of respiratory liver motion on heating for gated and model-based motion-compensated high-intensity focused ultrasound ablation. In: *Lecture Notes in Computer Science (Including Subseries Lecture Notes in Artificial Intelligence and Lecture Notes in Bioinformatics)*. Vol 6891 LNCS. ; 2011:605-612. doi:10.1007/978-3-642-23623-5_76.
 36. Rit S, Wolthaus JWH, van Herk M, Sonke J-J. On-the-fly motion-compensated cone-beam

- CT using an a priori model of the respiratory motion. *Med Phys.* 2009;36(6):2283-2296. doi:10.1118/1.3115691.
37. Zhang Q, Pevsner A, Hertanto A, et al. A patient-specific respiratory model of anatomical motion for radiation treatment planning. *Med Phys.* 2007;34(12):4772-4781. doi:10.1118/1.2804576.
38. Shechter G, Resar JR, McVeigh ER. Displacement and velocity of the coronary arteries: Cardiac and respiratory motion. *IEEE Trans Med Imaging.* 2006;25(3):369-375. doi:10.1109/TMI.2005.862752.
39. Xu Q, Hamilton RJ. A novel respiratory detection method based on automated analysis of ultrasound diaphragm video. *Med Phys.* 2006;33(4):916-921. doi:10.1118/1.2178451.
40. Vedam SS, Kini VR, Keall PJ, Ramakrishnan V, Mostafavi H, Mohan R. Quantifying the predictability of diaphragm motion during respiration with a noninvasive external marker. *Med Phys.* 2003;30(4):505-513. doi:10.1118/1.1558675.
41. Castillo R, Castillo E, Guerra R, et al. A framework for evaluation of deformable image registration spatial accuracy using large landmark point sets. *Phys Med Biol.* 2009;54(7):1849-1870. doi:10.1088/0031-9155/54/7/001.
42. Castillo E, Castillo R, Martinez J, Shenoy M, Guerrero T. Four-dimensional deformable image registration using trajectory modeling. *Phys Med Biol.* 2010;55(1):305-327. doi:10.1088/0031-9155/55/1/018.
43. Karami E, Wang Y, Gaede S, Lee T-Y, Samani A. Anatomy-based algorithm for automatic segmentation of human diaphragm in noncontrast computed tomography images. *J Med Imaging.* 2016;3(4):46004. doi:10.1117/1.JMI.3.4.046004.
44. Rueckert D, Sonoda LI, Hayes C, Hill DL, Leach MO, Hawkes DJ. Nonrigid registration using free-form deformations: application to breast MR images. *IEEE Trans Med Imaging.* 1999;18(8):712-721. doi:10.1109/42.796284.
45. Mastin CW. Fundamentals of Grid Generation (P. Knupp and S. Steinberg). *SIAM Rev.* 1995;37(2):264-265. doi:10.1137/1037067.
46. Pearson K. On lines and planes of closest fit to systems of points in space. *London, Edinburgh, Dublin Philos Mag J Sci.* 1901;2(1):559-572.

doi:10.1080/14786440109462720.

47. Shirzadi Z, Sadeghi-Naini A, Samani A. Toward in vivo lung's tissue incompressibility characterization for tumor motion modeling in radiation therapy. *Med Phys*. 2013;40(5):51902. doi:10.1118/1.4798461.
48. Karami E, Gaede S, Lee T-Y, Samani A. A biomechanical approach for in vivo lung tumor motion prediction during external beam radiation therapy. *Proc SPIE Med Imaging*. 2015;9415:941512. doi:10.1117/12.2082447.
49. Blackall JM, Ahmad S, Miquel ME, McClelland JR, Landau DB, Hawkes DJ. MRI-based measurements of respiratory motion variability and assessment of imaging strategies for radiotherapy planning. *Phys Med Biol*. 2006;51(17):4147-4169. doi:10.1088/0031-9155/51/17/003.

Chapter 5 « A Neural Network Approach for Biomechanics-based Tracking of Lung Tumors during External Beam Radiation Therapy »

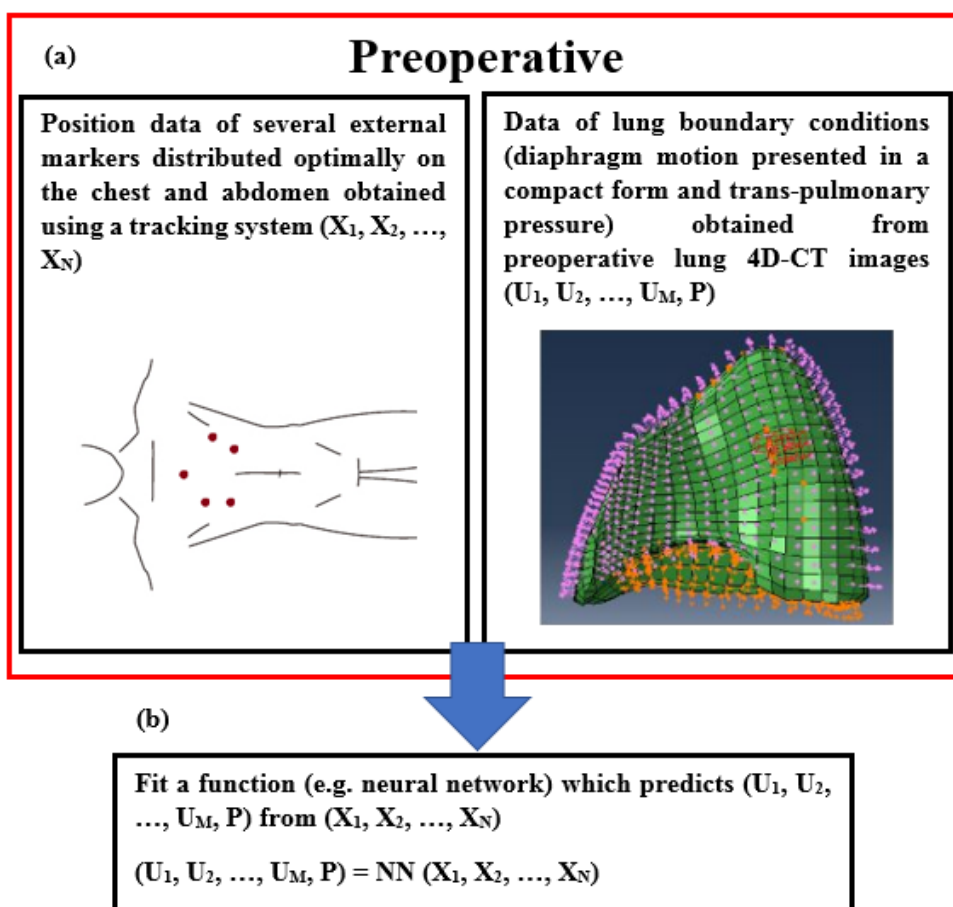
5.1 Introduction

According to statistics, cancer is one of the leading causes of death worldwide¹. EBRT is one of the primary treatment methods of lung cancer which is difficult to perform due to respiration induced tumor motion. Various methods have been proposed for tumor motion compensation, including motion encompassing methods, breath-hold methods^{2,3}, respiratory gating methods^{4,5} and real-time tracking methods⁶⁻¹¹. Among these methods, real-time tracking methods have become popular as they can potentially lead to maximum normal tissue sparing and short treatment sessions. Real-time tracking can be performed directly or indirectly. Direct tracking can be done by real-time imaging of the tumor or implanted fiducial markers⁵ or real-time tracking of electromagnetic coils, implanted in the tumor. The latter is done with electromagnetic tracking devices^{8,9,12,13}.

Although direct real-time imaging provides high accuracy in tumor motion estimation¹⁴, it is invasive as it requires near continuous fluoroscopy, irrespective of using implanted fiducial markers, leading to high radiation dose. The electromagnetic tracking approach is also invasive, due to the potential risk of pneumothorax or clip migration¹⁵. In indirect tracking methods, which are generally non-invasive, external signals are used such as signals representing chest motion acquired using optical tracking¹⁶. For these methods to work well, a strong and robust correlation between the external signal and 3D tumor position is required. However, a number of studies, which use the motion of a single chest/abdomen marker as surrogate to tumor motion, indicate that the correlation between the chest/abdomen motion obtained from a single marker and tumor motion is not robust or strong for all subjects^{17,18}. These results stem from the fact that the chest and abdominal surface motion is too complex to be fully characterized with one single marker. In addition

to the necessity for developing robust and strong correlations between surrogate signal and tumor motion, the tumor tracking method should account for tumor geometry variations during breathing. A recent study indicates that the size of Gross Tumor Volume (GTV) can vary by up to 62% during breathing¹⁹ concluding that lung tumor deformation should be accounted for.

In this paper, we present an expert system for indirect lung tumor tracking which addresses the limitations with current indirect tumor tracking methods. The proposed tumor tracking framework consists of a lung biomechanical model being used for tumor motion/deformation tracking and two neural networks which estimate the lung biomechanical model real-time boundary conditions from chest motion data. The proposed tumor tracking algorithm is summarized in Figure 5-1.



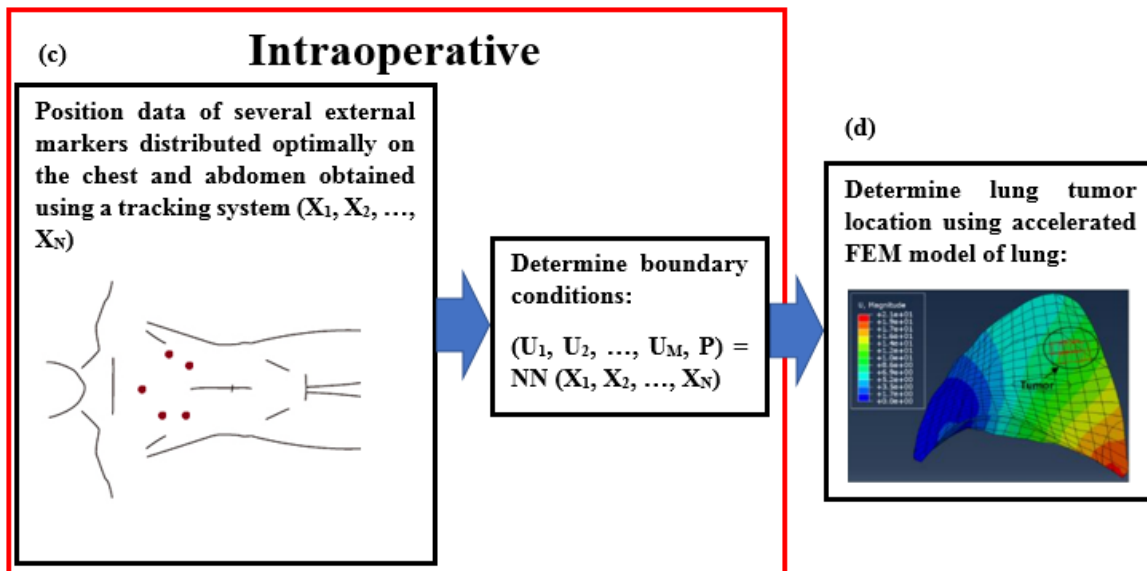


Figure 5–1 A block diagram of lung tumor tracking system. It involves four steps of (a) pre-treatment chest surface motion tracking and image based estimation of the lung boundary conditions. These boundary conditions include prescribed displacement boundary conditions of lung bottom surface which is equal to diaphragm surface displacements shown in orange and lung trans-pulmonary pressure shown in purple. (b) Fitting a function (e.g. using neural network (NN) which maps chest surface data to lung boundary conditions. This fitting requires the diaphragm to be presented in a compact form. (c) Intra-treatment chest surface data acquisition and mapping to boundary conditions in real-time. (d) Calculating lung tumor position using an accelerated lung biomechanical model.

As shown in Figure 5-1, the proposed algorithm consists of a pre-treatment step, where the lung biomechanical model is built from pre-treatment 4D-CT data, and a relationship is established between chest motion data, which is obtained from tracking an optimal number of chest markers, and lung biomechanical model boundary conditions. The lung biomechanical model boundary conditions include diaphragm displacement values and trans-pulmonary pressure. The second step in the proposed algorithm is the intra-treatment step where the real-time lung biomechanical model BCs are estimated from the chest motion data using the mapping function developed in the first step, and the tumor motion/deformation is calculated. Several research groups have tackled the problem of lung tumor tracking using mathematical models in conjunction with 4D CT or CBCT images^{20–25}. In contrast to indirect heuristic mathematical methods of lung tumor motion prediction which rely solely on data fitting mathematical model, the proposed method is a

hybrid method of heuristic data fitting in conjunction with a tissue deformation, physics-based model. The first component of the data fitting model is an NN used to predict the lung BCs from input chest surface motion data. To ensure robustness of this NN, an optimal number of markers leading to highest correlation between chest surface motion data and tumor motion can be determined and used instead of a single marker. It should be noted that in this work, we developed individualized NNs where pre-treatment data of each patient over all respiration phases were used to develop the patient specific NN to be used during treatment for the same patient. The second component is the lung biomechanical model which inputs the BCs obtained from the NN to output the intra-treatment tumor position and geometry. This hybrid approach is believed to be more effective than using a solely heuristic model (e.g. NN) to calculate tumor position and geometry directly from the chest wall surface motion data. The reason is that the NN in the latter scenario is expected to be highly complex while being prone to data overfitting. Using an accurate lung biomechanical model in the proposed system has two advantages: 1) accuracy of tumor motion tracking will be high and 2) tumor geometry variations during respiration can be taken into account, paving the way for more accurate radiation dose distribution calculation. In this paper, our focus is the first block of Figure 5-1 which is the NN training and testing. After training and testing the NN, it was incorporated into a previously developed lung biomechanical model and the total accuracy of the system was evaluated.

5.2 Materials and methods

5.2.1 Data acquisition

In this study, patient-specific NNs were developed for five patients using 4D CT images. These patients were scanned using a 16-slice Philips Brilliance Big Bore CT scanner (Philips Medical Systems, Cleveland, USA) operating in helical mode. The scanning parameters are: 120 kVp and 400 mAs/slice for tube potential and current, respectively. The pitch of the couch depended on the patient's breathing period and was set to around 0.1. The intra-slice pixel size of the data was set to vary from 0.98 mm to 1.29 mm while the slice thickness was set to 3 mm. Projection data were sorted using the Real-time Position ManagementTM (RPM) system (Varian Medical Systems, Inc., Palo Alto, CA, USA). Three of the patients had only one set of 4D CT images while the other two patients

had both pre-treatment and follow-up 4D CT images. Each 4D CT data set includes 10 respiratory phases. For the first three patients, 90% of the images were used for training the NNs and 10% of them were used for testing the NNs. This training scheme allows for testing the proposed tumor tracking method in prediction of intra-fraction motion variations. For the fourth and fifth patients, the pre-treatment images were used for training the NNs and the follow-up images were used to test the NNs to assess the algorithm accuracy in predicting the inter-fraction motion variations.

5.2.2 Rib motion tracking for obtaining the chest motion data

Chest motion data required to be used as input to the NNs was obtained through semi-automatic segmentation of individual ribs and sternum body, followed by rigid registration of each bone from end exhalation phase to each phase of respiration. To have sufficient data representing the chest surface motion, we tracked the motion of 8th, 9th and 10th left ribs, 6th and 10th right ribs and the sternum body. The segmented ribs and sternum body are shown in Figure 5-2. These landmarks were selected empirically by looking at motion patterns of the individual ribs and selecting the ones which are less similar. In addition to the rib motion signals, an AP signal was obtained from the RPM device used for sorting the 4D CT images. As such, instead of using one chest motion signal, we used 7×3 motion signals obtained from 6 chest markers and one abdominal marker, which together represent the chest and abdomen motion more accurately.

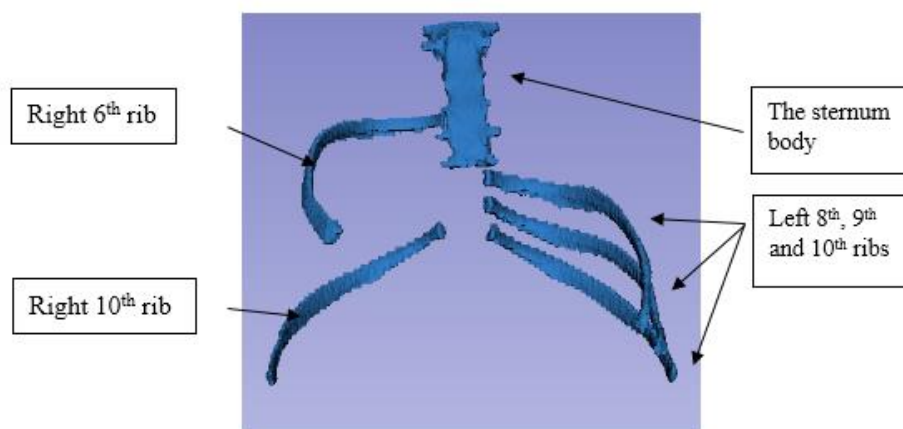
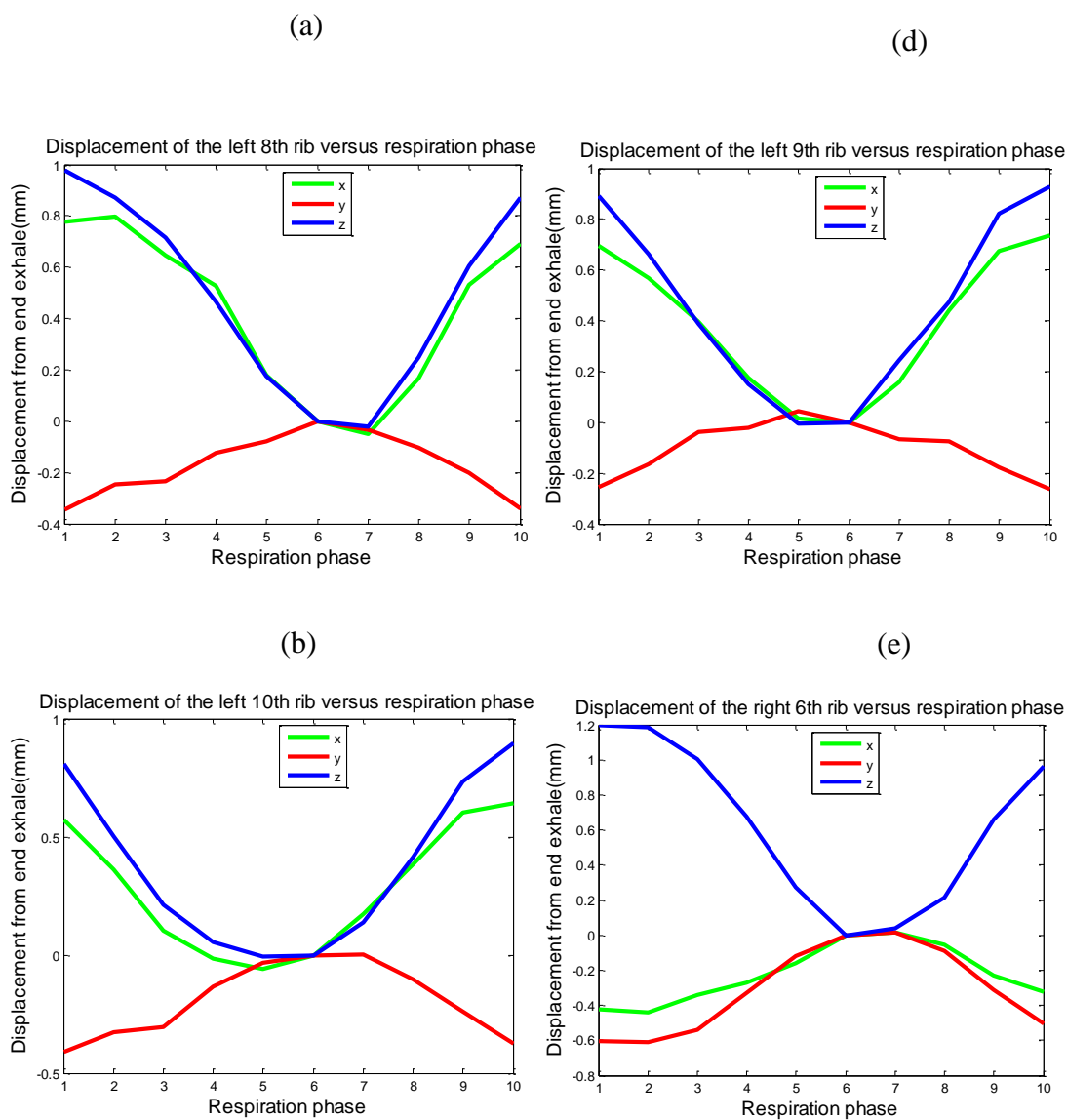


Figure 5–2 Segmented 8th, 9th and 10th left ribs, 6th and 10th right ribs and the sternum body.

After performing rigid registration, the tip of each rib was segmented using an automatic algorithm which finds the most anterior point of each rib, and selects a group of rib points located within 2mm of the most anterior point. Next, the motion signals for the rib tip were calculated by averaging the motion signals of all the points within the segmented tip. As for the sternum body, its displacement data were obtained by finding the displacement of its centroid. The motion signals obtained for the rib tips and sternum body are shown in Figure 5-3 for subject #2.



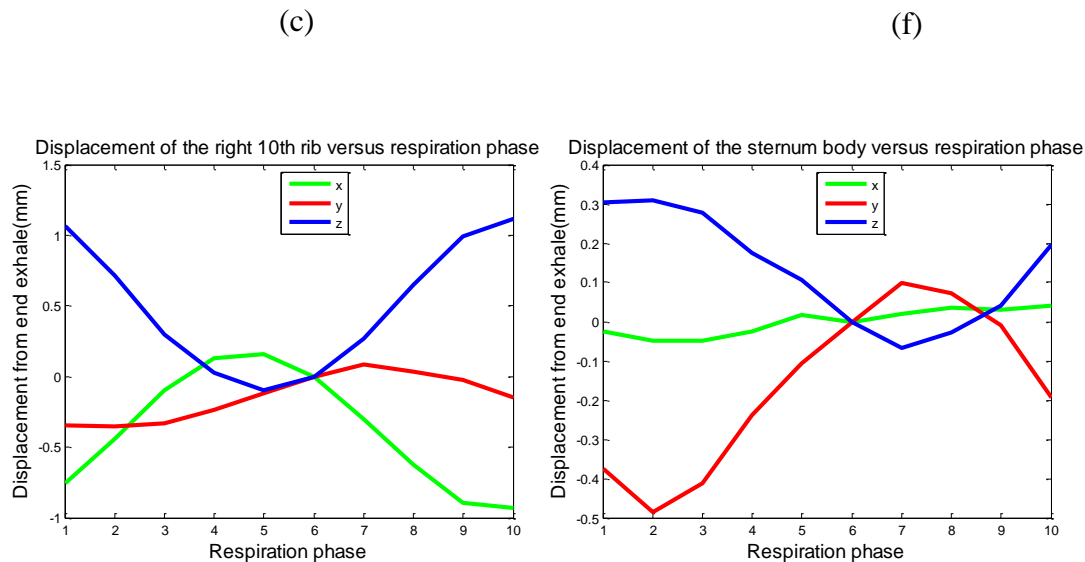


Figure 5–3 The x, y, and z displacement component data of segmented ribs and sternum body for subject #2.

5.2.3 Diaphragm motion and trans-pulmonary pressure data

The first NN was trained to estimate the diaphragm displacement field from chest motion data. The diaphragm displacement field at each phase of respiration was obtained through segmenting the diaphragm-lung contact surface using the algorithm proposed by Karami et al.²⁶, followed by registering the segmented diaphragm to end exhalation phase diaphragm using Free Form Deformation (FFD) non-rigid registration. To use the diaphragm displacement fields as lung biomechanical model BCs, the calculated deformation fields were mapped onto the bottom surface nodes of the lung FE mesh using nearest neighbor interpolation method. The bottom surface nodes of FE mesh are shown in Figure 5-4 (a). The displacements assigned to the diaphragm nodes are the outputs of the first NN. For the five subjects being studied in this paper, the bottom surface of the lung mesh has 113, 187, 89, 80, and 93 nodes, respectively. Therefore, the displacement of the lung's bottom surface for these patients and at each phase of respiration is characterized by 113×3 , 187×3 , 89×3 , 80×3 , and 93×3 matrices, respectively. The diaphragm nodes and corresponding SI, AP and LR displacement data for subject #2 are shown in Figures 5-4 (a), (b), (c) and (d), respectively.

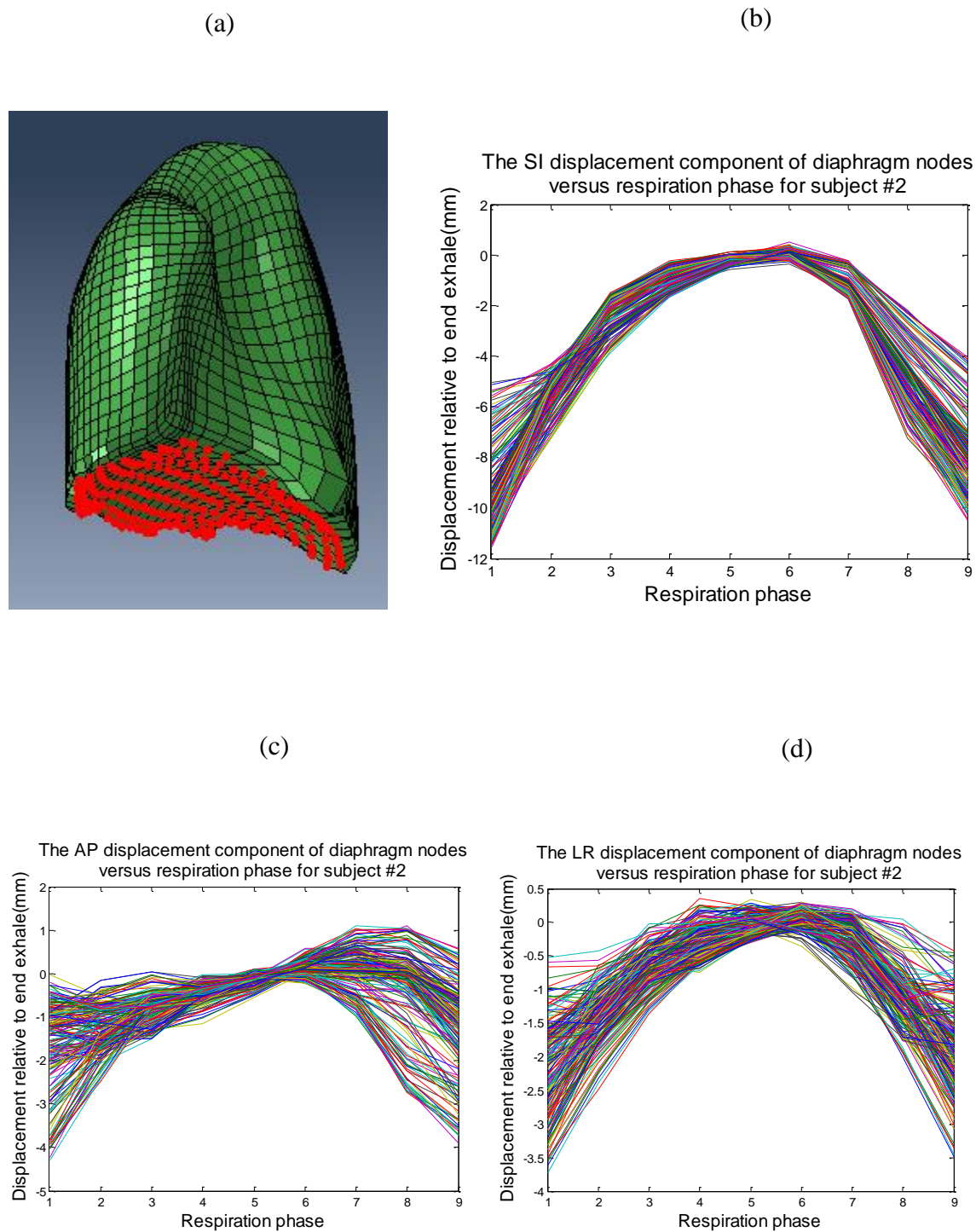


Figure 5–4 (a) The diaphragm nodes. (b), (c) and (d) corresponding SI, AP and LR displacement curves for subject #2. Each curve color in (b), (c), and (d) represents a node of the diaphragm.

The second NN was trained to estimate the trans-pulmonary pressure from chest motion data. The trans-pulmonary pressure magnitude was obtained through optimization as described in detail in Karami et al.²⁷. The optimization framework used for calculating the trans-pulmonary pressure values is depicted in Figure 5-5. As shown in this figure, at each phase of respiration, the pressure was calculated by comparing simulated image with its corresponding actual CT image. The simulated image was obtained using deformed FE mesh and Thin Plate Spline (TPS) image registration method. The optimized pressure curves for the first three subjects are shown in Figure 5-6 (a). The pre-treatment and follow-up optimized pressure curves obtained for subjects #4 and #5 are shown in Figure 5-6 (b).

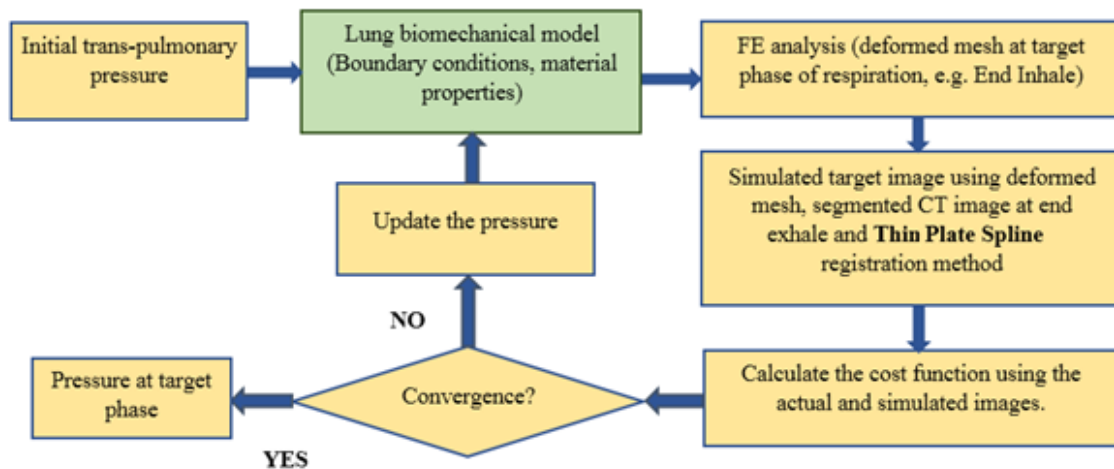


Figure 5–5 Optimization framework used to calculate trans-pulmonary pressure at each phase of respiration. In this framework, a pre-developed lung biomechanical model for which the trans-pulmonary pressure acts as BC, is used to optimize the pressure. The cost function is the difference between the actual CT images and the images constructed using the deformed mesh and TPS image registration method.

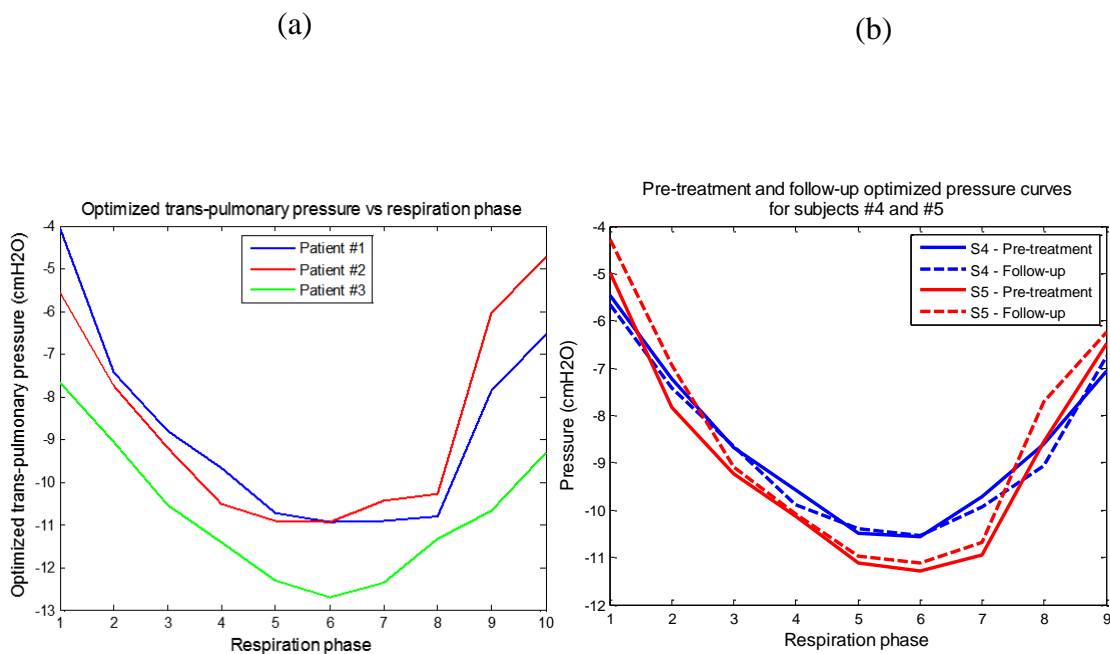


Figure 5-6 (a)The optimized pressure curves for subjects #1, #2 and #3. (b)The pre-treatment (solid line) and follow-up (dashed line) optimized pressure curves for subjects #4 and #5.

5.2.4 Neural Networks Training

5.2.4.1 Data preparation

For the first three subjects, to prepare the data for training the neural networks for each patient, PCA was performed on normalized chest and diaphragm motion data to reduce their size (spatial reduction). It should be noted that, in this context, PCA was used to capture the time variations of the chest motion and diaphragm motion using a compact mathematical form. In this study, PCA indicated that for chest motion data and diaphragm motion, 98% of information can be expressed using only 2 eigen vectors. As such, the chest and diaphragm motion data were reduced to two 2×9 matrices, while the pressure is a 1×9 vector where 9 is the number of phases other than the reference phase. Next, all matrices were normalized between 0 and 1 to be used for NN training. Examples of normalized principal components of chest motion data and diaphragm motion are depicted in Figures 5-7 (a) and (b) for subject #2.

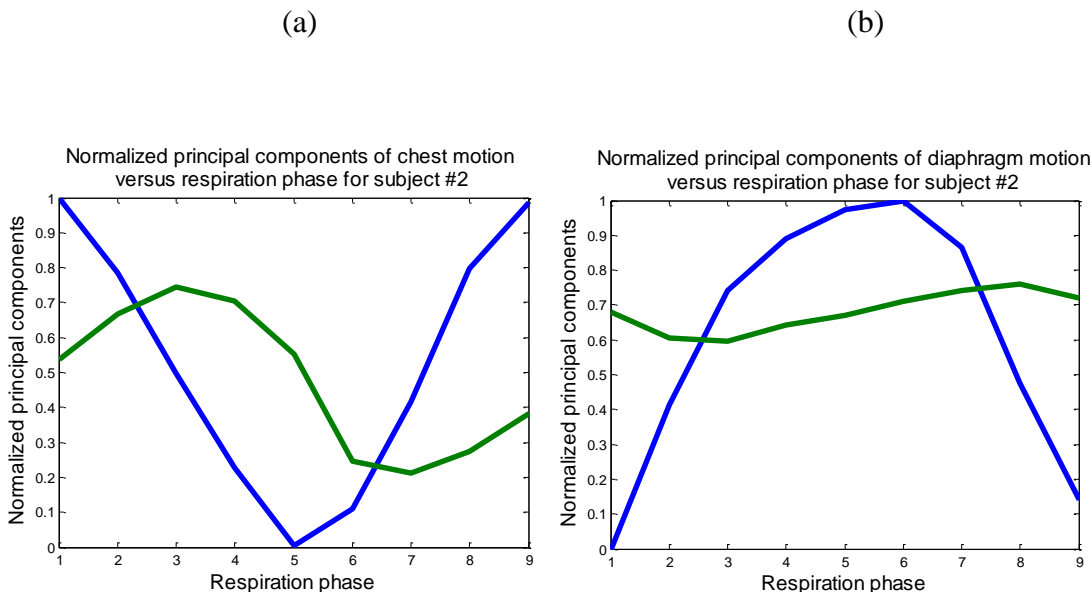


Figure 5–7 Normalized principal components of (a) chest, and (b) diaphragm motion data for subject #2.

After normalization, the input and output vectors were divided to training and test data sets. For that purpose, we used the leave-one-out cross validation scheme. After data division, a NN was used for estimating the trans-pulmonary pressure and another NN was used for estimating the diaphragm motion from chest motion data. We used feed forward networks, with one hidden layer while the Levenberg-Marquardt algorithm was used to train the networks. The training and testing of NNs were implemented in MATLAB. For the remaining two subjects, as mentioned earlier, the pre-operative data was used for training two NNs for each patient and the follow-up data was used for testing them. For subjects #4 and #5, as indicated earlier, follow up 4D CT images are available which allowed evaluating the proposed method with inter-fractionation. For these subjects, data preparation was similar to the first three patients, except that normalization prior to training was eliminated to be able to model the inter-fraction variations in the magnitude of signals.

5.2.4.1.1 Accounting for base-line shift

To account for base-line shifts that occurred between pre-treatment and follow-up sessions, we used Free Form Deformation non-rigid registration to register the end-exhale lung from the first data set to the end-exhale lung from the second data set, and the lung FE mesh was adjusted accordingly. The similarity measure used for registration is the mutual

information. Here, we had to use non-rigid registration for removing the base-line shifts because the pre-treatment images were taken with patient's hands up beside their head, while the follow up images were taken with patient's hands beside their body. These different positions affect the lung anatomy. In a more conventional clinical setting where the patient set up is similar for planning and treatment sessions, chest surface data can be used for rigid registration of the lung to account for base-line shifts, eliminating the need for daily imaging sessions.

5.2.4.2 Diaphragm motion estimation using Neural Network

The NN configuration for estimating the diaphragm motion from chest motion data is shown in Figure 5-8. As shown in this figure, the network has one hidden layer with two neurons, and both input and output layers of NN are of size 2. The NN configuration for pressure fitting is similar to the network used for diaphragm motion estimation except that the output layer is of size 1.

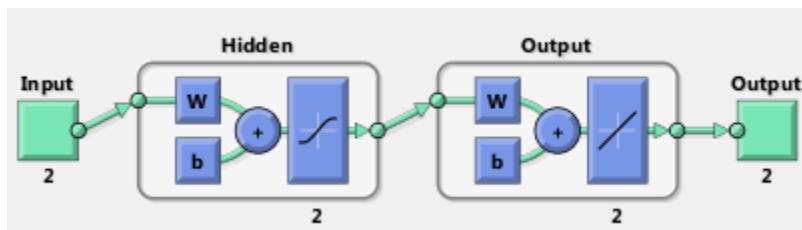


Figure 5–8 Feed forward NN used to estimate the diaphragm motion from chest motion data. The network has one hidden layer with two nodes.

5.2.5 Validation

Validation was performed both qualitatively and quantitatively. For the first three patients, data division was performed 9 times for each phase. Next, the NN was trained and tested. For the fourth and fifth patients, the follow-up data was used to test the NNs developed using the pre-treatment data. The performance of NNs was assessed using the mean error in diaphragm motion and pressure estimation. A second validation was performed by assessing the NN error propagation in the lung biomechanical model. For this purpose, the output of NN was used as the lung BCs to predict tumor motion and deformation.

5.3 Results

5.3.1 Qualitative validation

Results of NN training step indicate that the accuracy of data fitting depends strongly on the marker location and the number of markers used for training. For instance, the sternum body was not a good landmark for the subjects being studied in this paper and the results of data fitting improved significantly for all subjects when the sternum body was removed from the landmarks set. In addition, while the results indicate that the pressure inter-fraction variations can be successfully obtained from chest motion data, for diaphragm inter-fraction motion estimation, the presence of an abdominal marker is necessary. Overall, the results indicate that with suitable marker location/number, both pressure and diaphragm motion can be estimated from chest motion data. Figures 5-9 and 5-10 depict examples of results obtained from intra-fraction and inter-fraction validation tests, respectively. Figure 5-9 (a), depicts the actual trans-pulmonary pressure curves overlaid on the pressure values predicted by the NN for subject #2. Figure 5-9 (b) illustrates the actual principal components of diaphragm motion overlaid on the corresponding NN predicted values for the same subject. Figures 5-10 (a) and (b) depict similar results for subject #4 which was used to test the model for inter-fraction motion variation prediction. Qualitatively, the results obtained from NNs agree very well with the actual pressure and diaphragm motion values.

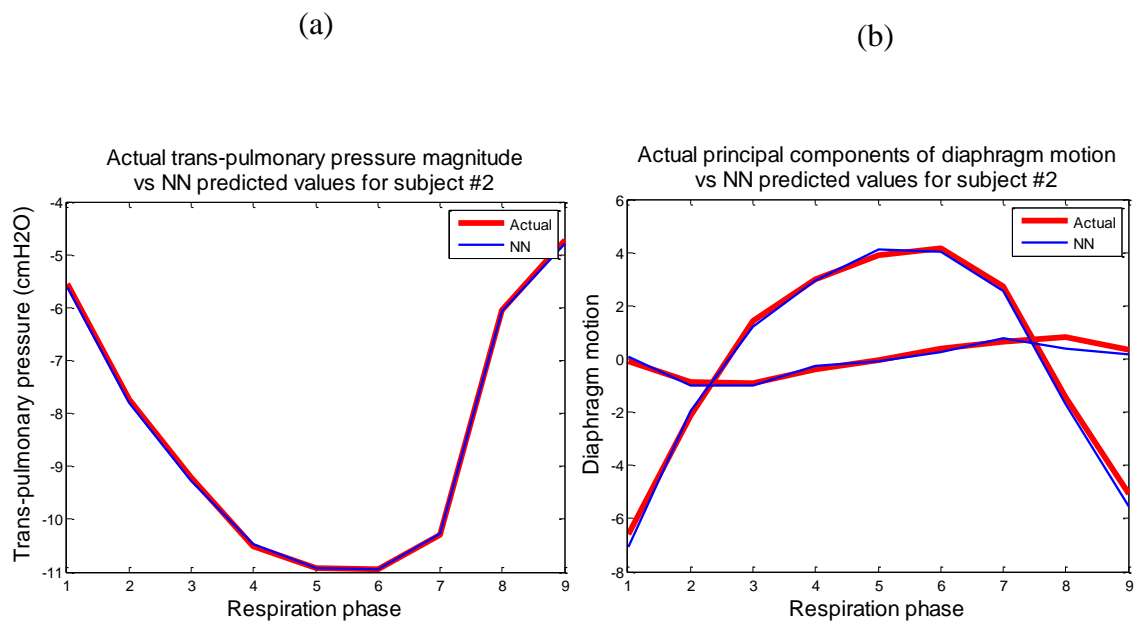


Figure 5-9 Intra-fraction validation test. (a) Actual and NN estimated trans-pulmonary pressure curves, and (b) diaphragm motion principal components for subject #2.

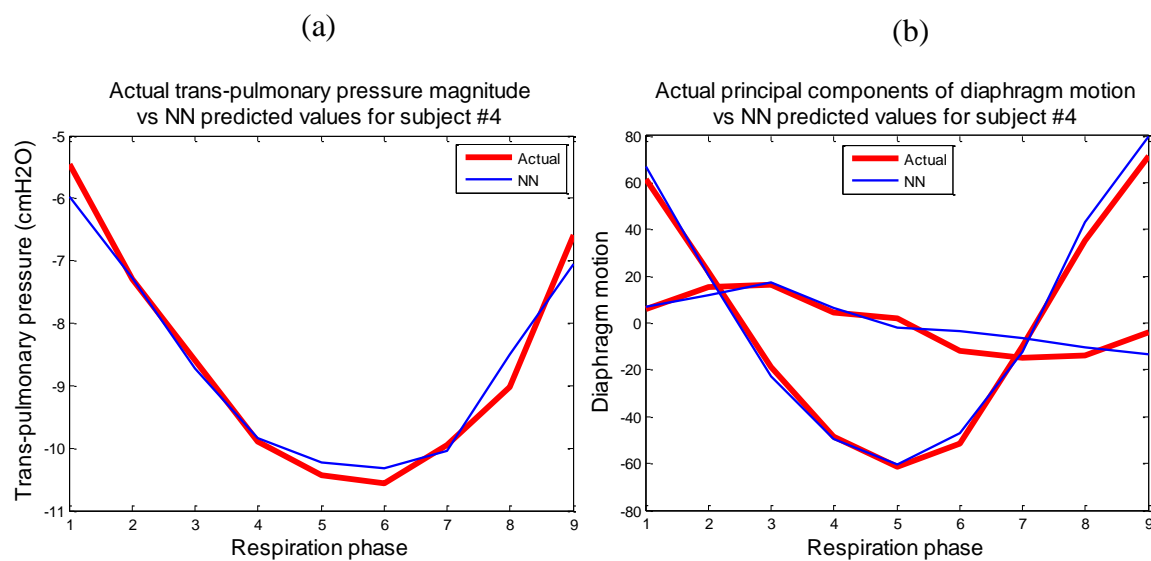
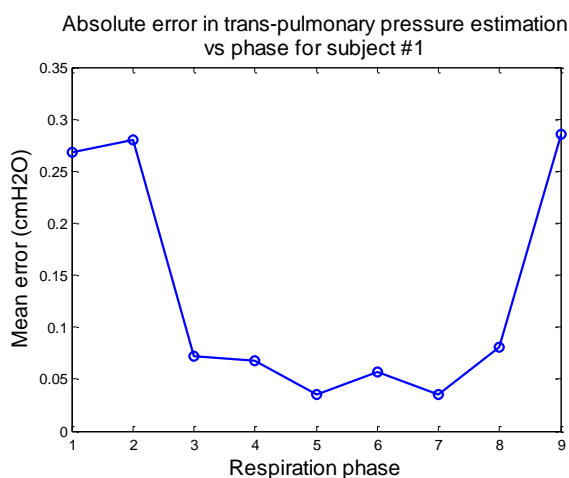


Figure 5-10 Results obtained from inter-fraction motion estimation test. (a) Actual and NN-estimated trans-pulmonary pressure curves, and (b) diaphragm motion principal components for subject #4.

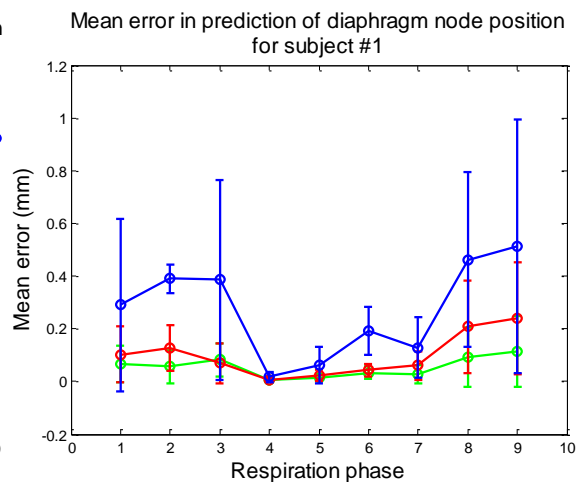
5.3.2 Quantitative validation

After developing the NNs, the first quantitative validation was performed by calculating the mean error in estimating the diaphragm displacement field and trans-pulmonary pressure values. Figures 5-11 (a), (b), and (c) depict the mean error in pressure estimation for each test data set for the first three patients. Figures 5-11 (e), (f), and (g) illustrate the mean error per landmark in estimating the diaphragm motion for the same patients. As shown in these figures, the absolute error in pressure estimation is less than 0.3 cmH₂O, and the mean error per landmark in diaphragm motion estimation is less than 0.6 mm over all subjects, phases of respiration, and dimensions. These results indicate high accuracy in estimating the diaphragm motion and trans-pulmonary pressure intra-fraction variations.

(a)



(d)



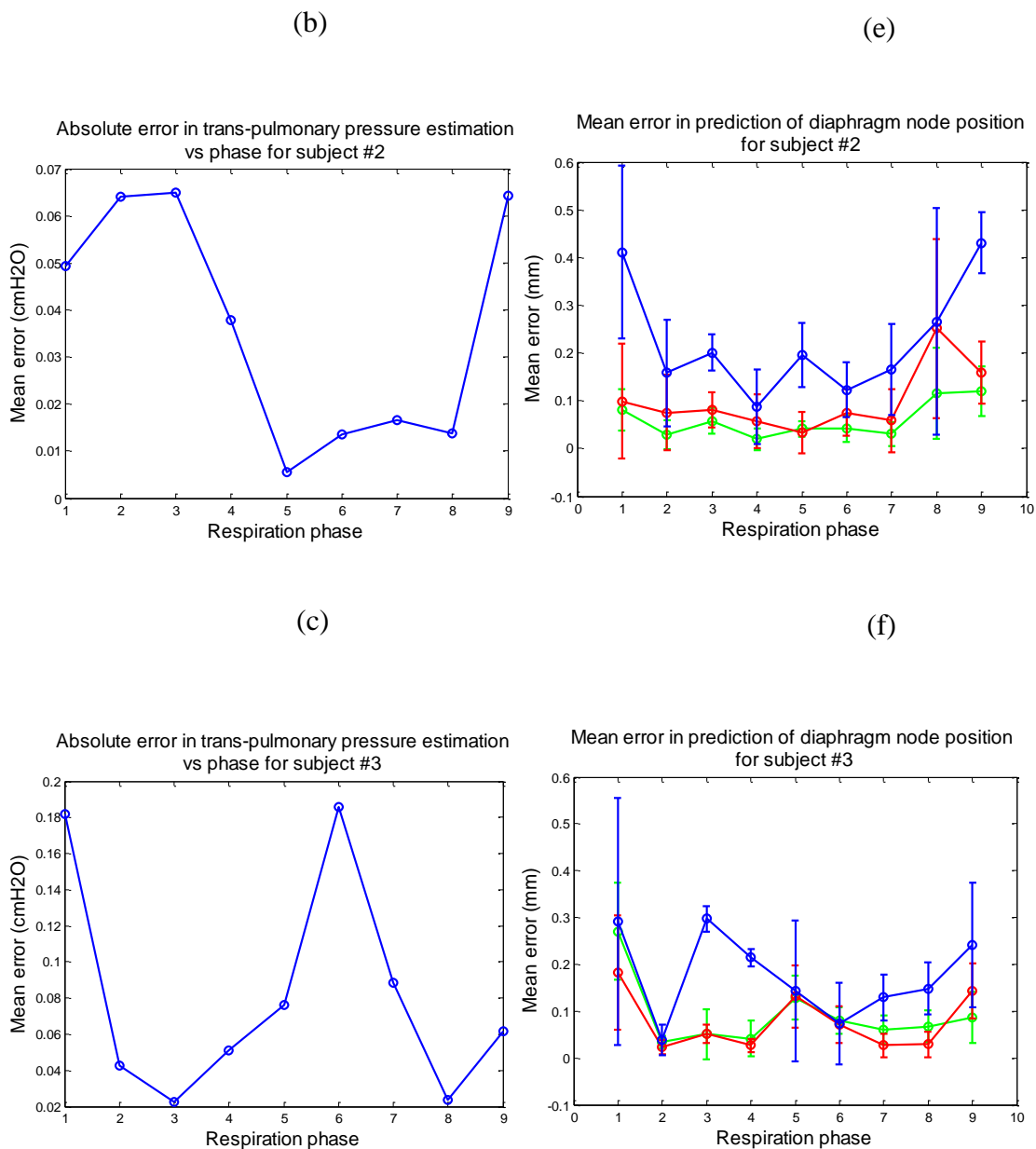


Figure 5–11 (a), (b) and (c) Mean error in pressure estimation vs respiration phase. (d), (e) and (f) Mean error in diaphragm motion estimation vs respiration phase.

Table 5-1 represents quantitative results for subjects #4 and #5. As indicated by this table, the mean error in diaphragm motion estimation in x, y and z directions is 0.25 (mm), 0.19 (mm) and 0.14 (mm), respectively. In addition, the mean error in pressure estimation is 0.24 (cmH₂O) which is favorable.

	Mean error per landmark in			Mean error in pressure estimation (cmH ₂ O)
	diaphragm motion prediction (mm)			
	x	y	z	
Subject #4	0.20	0.23	0.11	0.22
Subject #5	0.29	0.15	0.16	0.25
Mean \pm SD	0.25 \pm 0.06	0.19 \pm 0.06	0.14 \pm 0.04	0.24 \pm 0.02

Table 5-1 Mean error in inter-fraction diaphragm motion (mm) and trans-pulmonary pressure (cmH₂O) prediction for subjects #4 and #5.

The second quantitative validation was performed by incorporating the NNs in the lung tumor tracking algorithm. For this purpose, the NN predicted boundary conditions were used to predict the tumor motion and the results were compared to tumor tracking results obtained from actual lung BCs. For this purpose, first the Dice similarity coefficient between the actual tumor volume and the volume predicted by lung biomechanical model was calculated where the lung biomechanical BCs were obtained from 4D CT images. The results are reported in Tables 5-2 and 5-3. Next, the same calculation was performed using the NNs to obtain the lung biomechanical model BCs and calculate the tumor trajectories. Results of the second calculation are reported in Tables 5-4 and 5-5 for estimation of intra-fraction and inter-fraction motion variations, respectively. These results indicate that the proposed algorithm can estimate the intra-fraction tumor motion variations with a mean Dice similarity coefficient of 0.86 ± 0.06 . In the presence of inter-fraction motion, the Dice similarity coefficient is reduced by 5% where the mean Dice obtained from actual BCs is 0.88 ± 0.06 and it is reduced to 0.83 ± 0.06 . Despite the aforementioned error, the results are still favorable.

Phase number	1	2	3	4	5	6	7	8	9
Patient #1	0.80	0.90	0.87	0.90	0.90	0.90	0.88	0.79	0.82

Patient #2	0.90	0.88	0.86	0.90	0.93	0.93	0.78	0.81	0.79
Patient #3	0.83	0.86	0.85	0.90	0.94	0.93	0.85	0.80	0.84
Mean \pm SD	0.84 \pm 0.05	0.88 \pm 0.02	0.86 \pm 0.01	0.90 \pm 0.0	0.92 \pm 0.02	0.92 \pm 0.02	0.84 \pm 0.05	0.80 \pm 0.01	0.82 \pm 0.03

Table 5-2 Dice similarity coefficient between actual Gross Tumor Volume (GTV) and the lung biomechanical model estimated GTV for three subjects over the full respiratory cycle. The lung biomechanical model is driven with image derived (actual) boundary conditions. These patients were used to assess the algorithm performance in estimating the intra-fraction motion variation.

Phase number	1	2	3	4	5	6	7	8	9
Patient #4	0.88	0.86	0.89	0.92	0.94	0.92	0.87	0.83	0.81
Patient #5	0.86	0.90	0.86	0.95	0.94	0.90	0.85	0.79	0.83
Mean \pm SD	0.87 \pm 0.01	0.88 \pm 0.03	0.88 \pm 0.02	0.94 \pm 0.02	0.94 \pm 0.0	0.91 \pm 0.01	0.86 \pm 0.01	0.81 \pm 0.03	0.82 \pm 0.01

Table 5-3 Dice similarity coefficient between actual Gross Tumor Volume (GTV) and the lung biomechanical model estimated GTV for two subjects over the full respiratory cycle. The lung biomechanical model is driven with image derived (actual) boundary conditions. These patients were used to assess the algorithm performance in estimating the inter-fraction motion variation.

Phase number	1	2	3	4	5	7	8	9	10
Patient #1	0.79	0.90	0.86	0.90	0.90	0.90	0.87	0.79	0.81
Patient #2	0.89	0.86	0.86	0.90	0.92	0.93	0.78	0.82	0.81

Patient #3	0.84	0.84	0.85	0.90	0.92	0.93	0.83	0.80	0.84
Mean \pm SD	0.81 \pm 0.03	0.87 \pm 0.03	0.86 \pm 0.01	0.90 \pm 0.0	0.91 \pm 0.01	0.92 \pm 0.02	0.83 \pm 0.05	0.80 \pm 0.02	0.82 \pm 0.02

Table 5-4 Dice similarity coefficient between actual Gross Tumor Volume (GTV) and the lung biomechanical model estimated GTV for four subjects over the full respiratory cycle. The lung biomechanical model is driven with Neural Network estimated BCs. These patients were used to assess the algorithm performance in estimating the intra-fraction motion variation.

Phase number	1	2	3	4	5	6	7	8	9
Patient #4	0.81	0.80	0.80	0.89	0.90	0.90	0.80	0.79	0.81
Patient #5	0.80	0.84	0.80	0.93	0.91	0.89	0.78	0.73	0.75
Mean \pm SD	0.81 \pm 0.01	0.83 \pm 0.01	0.80 \pm 0.0	0.91 \pm 0.03	0.91 \pm 0.01	0.90 \pm 0.02	0.79 \pm 0.01	0.76 \pm 0.04	0.78 \pm 0.04

Table 5-5 Dice similarity coefficient between actual Gross Tumor Volume (GTV) and the lung biomechanical model estimated GTV for four subjects over the full respiratory cycle. The lung biomechanical model is driven with Neural Network estimated BCs. These patients were used to assess the algorithm performance in estimating the inter-fraction motion variation.

5.4 Discussion and Conclusions

Highly accurate NNs were developed for diaphragm motion characterization and transpulmonary pressure estimation from chest motion data. These NNs were developed to be used as a major component of an expert system being developed for lung tumor motion management in EBRT. The expert system is designed to predict lung tumor motion/deformation during treatment using surrogate signals of the patient's chest surface motion.

The premise of the expert system is the known correlation between the chest surface motion, which can be measured non-invasively during EBRT, and lung boundary conditions required for a previously developed lung biomechanical model used in the expert system. The chest motion data was obtained through segmentation and rigid registration of five individual ribs and sternum body. Ribs do not stretch and slide as skin can. As such, to minimize the difference between rib motion and skin motion, we picked subjects who had less fat under their skin. An abdominal motion signal was also obtained using the RPM marker. The diaphragm motion data was obtained using non-rigid registration while the trans-pulmonary pressure values were obtained using an optimization framework described in Figure 5-5. Both qualitative and quantitative results indicate favorable agreement between “true” and NN-based prediction of lung boundary conditions.

The results presented in this paper indicate that the proposed NN-based approach can be effectively used to predict the lung BCs from chest motion data. In addition, the results indicate that the trained NNs work well for prediction of both intra-fraction and inter-fraction variations in pressure and diaphragm motion. To further evaluate the NNs, a previously developed lung FE model was used to calculate tumor motion in five patients where the “true” BCs and the NN-based estimated BCs were used in the lung biomechanical model. Comparison of results obtained from these two sets of boundary conditions indicated that when the chest motion data is used to predict the lung BCs, the accuracy of tumor motion tracking is reduced by less than 5%. This confirms that error propagation from the NN-based boundary condition estimation into typical biomechanical lung model had insignificant impact on the biomechanical model’s overall accuracy.

It is noteworthy that all subjects enrolled in this study were either lung cancer or COPD patients while the previously developed lung biomechanical model was developed for healthy subjects. As such, better results are expected by incorporating more patient specific parameters such as nonuniform tissue mechanical properties pertaining to pathological tissue. In addition, it is known that different patients have different breathing patterns and the location of markers should not be fixed for all patients. In fact, the raw data used in this study indicates significant breathing irregularities can happen from session to session but those irregularities can be detected by using suitable markers. As such, a systematic method

can be used to individualize chest marker location optimization to increase the BC prediction accuracy. Real-time tracking of lung tumors has been tackled by many research groups including methods proposed for modeling intra-fraction²⁸⁻³¹ and inter-fraction^{30,32-35} variations. Such methods rely on using intermittent 4D CT³⁶, Cone-Beam CT²⁹, 4D CBCT³⁴, MR imaging, or using implanted fiducial markers imaged with fluoroscopy³⁷ to find the intra-fraction tumor motion. However, none of these methods can adequately image the 3D motion of the lung required for the whole treatment session. Repeated 4D CT^{32,33} or daily CBCT^{30,34,35} scans have also been used for measuring the inter-fraction motion variations which are reported to be mainly caused by base-line shifts in tumor positions relative to other organs^{34,35}.

Surrogate-driven tracking of lung tumors has been tackled by several research groups, including more recent studies published by McClelland et al.³⁸, Martin et al.²³, and Fassi et al.^{21,25}. All the existing tracking methods rely on Deformable Image Registration (DIR) followed by fitting functions relating the surrogate signal to the control points used for registration. Results presented by McClelland et al. indicate DIR-based tracking methods perform poorly in intra-fraction motion prediction unless optimum base-line landmark shifts are calculated and accounted for. Their results indicate that the base-line shift is not similar for different regions of the lung leading to necessity of non-rigid image registration performed on treatment day to account for those shifts. To address this issue, Fassi et al. propose using daily CBCT images to find the base-line shifts. Unlike DIR-based methods which rely on fitting a separate function for each of the control point displacements that define the B-spline transformation, the proposed algorithm relates the surrogate signal to lung boundary conditions, i.e. pressure and diaphragm motion. This approach results in algorithm robustness because lung BCs are associated with the physiology of breathing which is expected to have fewer variations over the course of treatment. Using a physics-based model with variable boundary conditions obtained from chest surface data, allows for accounting for inconsistent regional base-line shifts reported by other groups. Finally, to account for patient set-up variability through treatment sessions, the lung FE mesh needs to be adjusted accordingly. For this purpose, a high-resolution image of the chest/abdomen surface can be acquired to be registered to the same surface segmented on the pre-treatment

base-line image. Such a high resolution surface acquisition is possible using AlignRT® designed and produced by Vision RT for Surface Guided Radiation Therapy. This would eliminate the need for performing daily CBCT images required for finding the base-line shift of control points in DIR-based tracking methods. Overall, the results presented in this paper demonstrate the feasibility of tumor tracking using a biomechanics-based approach paving the way towards more accurate and robust EBRT.

5.5 References

1. Torre LA, Bray F, Siegel RL, Ferlay J, Lortet-tieulent J, Jemal A. Global Cancer Statistics, 2012. *CA a cancer J Clin.* 2015;65(2):87-108. doi:10.3322/caac.21262.
2. Boda-Heggemann J, Frauenfeld A, Weiss C, et al. Clinical outcome of hypofractionated breath-hold image-guided SABR of primary lung tumors and lung metastases. *Radiat Oncol.* 2014;9(1):10. doi:10.1186/1748-717X-9-10.
3. Hanley J, Debois MM, Mah D, et al. Deep inspiration breath-hold technique for lung tumors: The potential value of target immobilization and reduced lung density in dose escalation. *Int J Radiat Oncol Biol Phys.* 1999;45(3):603-611. doi:10.1016/S0360-3016(99)00154-6.
4. Cui Y, Dy JG, Sharp GC, Alexander B, Jiang SB. Robust fluoroscopic respiratory gating for lung cancer radiotherapy without implanted fiducial markers. *Phys Med Biol.* 2007;52(3):741-755. doi:10.1088/0031-9155/52/3/015.
5. Shirato H, Shimizu S, Kunieda T, et al. Physical aspects of a real-time tumor-tracking system for gated radiotherapy. *Int J Radiat Oncol Biol Phys.* 2000;48(4):1187-1195. doi:10.1016/S0360-3016(00)00748-3.
6. Sharp GC, Jiang SB, Shimizu S, Shirato H. Prediction of respiratory tumour motion for real-time image-guided radiotherapy. *Phys Med Biol.* 2004;49(3):425-440. doi:10.1088/0031-9155/49/3/006.

7. Torshabi AE, Pella A, Riboldi M, Baroni G. Targeting accuracy in real-time tumor tracking via external surrogates: a comparative study. *Technol Cancer Res Treat*. 2010;9(6):551-562. <http://www.ncbi.nlm.nih.gov/pubmed/21070077>.
8. Keall PJ, Colvill E, O'Brien R, et al. The first clinical implementation of electromagnetic transponder-guided MLC tracking. *Med Phys*. 2014;41(2):20702. doi:10.1118/1.4862509.
9. Wu J, Ruan D, Cho B, et al. Electromagnetic detection and real-time DMLC adaptation to target rotation during radiotherapy. *Int J Radiat Oncol Biol Phys*. 2012;82(3). doi:10.1016/j.ijrobp.2011.06.1958.
10. Murphy MJ. Tracking Moving Organs in Real Time. *Semin Radiat Oncol*. 2004;14(1):91-100. doi:10.1053/j.semradonc.2003.10.005.
11. Shirato H, Suzuki K, Sharp GC, et al. Speed and amplitude of lung tumor motion precisely detected in four-dimensional setup and in real-time tumor-tracking radiotherapy. *Int J Radiat Oncol Biol Phys*. 2006;64(4):1229-1236. doi:10.1016/j.ijrobp.2005.11.016.
12. Keall PJ, Sawant A, Cho B, et al. Electromagnetic-guided dynamic multileaf collimator tracking enables motion management for intensity-modulated arc therapy. *Int J Radiat Oncol Biol Phys*. 2011;79(1):312-320. doi:10.1016/j.ijrobp.2010.03.011.
13. Balter JM, Wright JN, Newell LJ, et al. Accuracy of a wireless localization system for radiotherapy. *Int J Radiat Oncol Biol Phys*. 2005;61(3):933-937. doi:10.1016/j.ijrobp.2004.11.009.
14. Poulsen PR, Cho B, Sawant A, Ruan D, Keall PJ. Dynamic MLC tracking of moving targets with a single kV imager for 3D conformal and IMRT treatments. *Acta Oncol (Madr)*. 2010;49(7):1092-1100. doi:10.3109/0284186X.2010.498438.
15. Imura M, Yamazaki K, Shirato H, et al. Insertion and fixation of fiducial markers for setup and tracking of lung tumors in radiotherapy. *Int J Radiat Oncol Biol*

- Phys.* 2005;63(5):1442-1447. doi:10.1016/j.ijrobp.2005.04.024.
16. Baroni G, Riboldi M, Spadea MF, et al. Integration of Enhanced Optical Tracking Techniques and Imaging in IGRT. *J Radiat Res.* 2007;48 Suppl A:A61-A74. doi:10.1269/jrr.48.A61.
 17. Tsunashima Y, Sakae T, Shioyama Y, et al. Correlation between the respiratory waveform measured using a respiratory sensor and 3D tumor motion in gated radiotherapy. *Int J Radiat Oncol Biol Phys.* 2004;60(3):951-958. doi:10.1016/j.ijrobp.2004.06.026.
 18. Ahn S, Yi B, Suh Y, et al. A feasibility study on the prediction of tumour location in the lung from skin motion. *Br J Radiol.* 2004;77(919):588-596. doi:10.1259/bjr/64800801.
 19. Weiss E, Wijesooriya K, Dill SV, Keall PJ. Tumor and normal tissue motion in the thorax during respiration: Analysis of volumetric and positional variations using 4D CT. *Int J Radiat Oncol Biol Phys.* 2007;67(1):296-307. doi:10.1016/j.ijrobp.2006.09.009.
 20. McClelland JR, Hughes S, Modat M, et al. Inter-fraction variations in respiratory motion models. *Phys Med Biol.* 2011;56(1):251-272. doi:10.1088/0031-9155/56/1/015.
 21. Fassi A, Seregini M, Riboldi M, et al. Surrogate-driven deformable motion model for organ motion tracking in particle radiation therapy. *Phys Med Biol.* 2015;60(4):1565-1582. doi:10.1088/0031-9155/60/4/1565.
 22. Fayad H, Pan T, Pradier O, Visvikis D. Patient specific respiratory motion modeling using a 3D patient's external surface. *Med Phys.* 2012;39(6):3386-3395. doi:10.1118/1.4718578.
 23. Martin J, McClelland J, Yip C, et al. Building motion models of lung tumours from cone-beam CT for radiotherapy applications. *Phys Med Biol.* 2013;58(6):1809-1822. doi:10.1088/0031-9155/58/6/1809.

24. Isaksson M, Jalden J, Murphy MJ. On using an adaptive neural network to predict lung tumor motion during respiration for radiotherapy applications. *Med Phys*. 2005;32(12):3801-3809. doi:10.1118/1.2134958.
25. Fassi A, Schaerer J, Fernandes M, Riboldi M, Sarrut D, Baroni G. Tumor tracking method based on a deformable 4D CT breathing motion model driven by an external surface surrogate. *Int J Radiat Oncol Biol Phys*. 2014;88(1):182-188. doi:10.1016/j.ijrobp.2013.09.026.
26. Karami E, Wang Y, Gaede S, Lee T-Y, Samani A. Anatomy-based algorithm for automatic segmentation of human diaphragm in noncontrast computed tomography images. *J Med Imaging*. 2016;3(4):46004. doi:10.1117/1.JMI.3.4.046004.
27. Karami E, Gaede S, Lee T-Y, Samani A. A biomechanical approach for in vivo lung tumor motion prediction during external beam radiation therapy. *Proc SPIE Med Imaging*. 2015;9415:941512. doi:10.1117/12.2082447.
28. Cai J, Read PW, Sheng K. The effect of respiratory motion variability and tumor size on the accuracy of average intensity projection from four-dimensional computed tomography: an investigation based on dynamic MRI. *Med Phys*. 2008;35(11):4974-4981. doi:10.1118/1.2982245.
29. Guckenberger M, Meyer J, Wilbert J, et al. Intra-fractional uncertainties in cone-beam CT based image-guided radiotherapy (IGRT) of pulmonary tumors. *Radiother Oncol*. 2007;83(1):57-64. doi:10.1016/j.radonc.2007.01.012.
30. Purdie TG, Bissonnette JP, Franks K, et al. Cone-Beam Computed Tomography for On-Line Image Guidance of Lung Stereotactic Radiotherapy: Localization, Verification, and Intrafraction Tumor Position. *Int J Radiat Oncol Biol Phys*. 2007;68(1):243-252. doi:10.1016/j.ijrobp.2006.12.022.
31. Seppenwoolde Y, Berbeco RI, Nishioka S, Shirato H, Heijmen B. Accuracy of tumor motion compensation algorithm from a robotic respiratory tracking system: a simulation study. *Med Phys*. 2007;34(7):2774-2784. doi:10.1118/1.2739811.

32. Britton KR, Starkschall G, Tucker SL, et al. Assessment of Gross Tumor Volume Regression and Motion Changes During Radiotherapy for Non-Small-Cell Lung Cancer as Measured by Four-Dimensional Computed Tomography. *Int J Radiat Oncol Biol Phys.* 2007;68(4):1036-1046. doi:10.1016/j.ijrobp.2007.01.021.
33. Redmond KJ, Song DY, Fox JL, Zhou J, Rosenzweig CN, Ford E. Respiratory Motion Changes of Lung Tumors Over the Course of Radiation Therapy Based on Respiration-Related Four-Dimensional Computed Tomography Scans. *Int J Radiat Oncol Biol Phys.* 2009;75(5):1605-1612. doi:10.1016/j.ijrobp.2009.05.024.
34. Sonke J-J, Rossi MMG, Wolthaus JWH, van Herk M, Damen E, Belderbos J. Frameless stereotactic body radiotherapy for lung cancer using four-dimensional cone beam CT guidance. *Int J Radiat Oncol Biol Phys.* 2009;74(2):567-574. doi:10.1016/j.ijrobp.2008.08.004.
35. Sonke JJ, Lebesque J, van Herk M. Variability of Four-Dimensional Computed Tomography Patient Models. *Int J Radiat Oncol Biol Phys.* 2008;70(2):590-598. doi:10.1016/j.ijrobp.2007.08.067.
36. Guckenberger M, Wilbert J, Meyer J, Baier K, Richter A, Flentje M. Is a Single Respiratory Correlated 4D-CT Study Sufficient for Evaluation of Breathing Motion? *Int J Radiat Oncol Biol Phys.* 2007;67(5):1352-1359. doi:10.1016/j.ijrobp.2006.11.025.
37. Seppenwoolde Y, Berbeco RI, Nishioka S, Shirato H, Heijmen B. Accuracy of tumor motion compensation algorithm from a robotic respiratory tracking system: A simulation study. *Med Phys.* 2007;34(7):2774-2784. doi:10.1118/1.2739811.
38. McClelland JR, Hughes S, Modat M, et al. Inter-fraction variations in respiratory motion models. *Phys Med Biol.* 2011;56(1):251-272. doi:10.1088/0031-9155/56/1/015.

Chapter 6 « Summary, Conclusion, and Future Work »

6.1 Summary

The overall goal of the thesis was to develop a surrogate-driven, biomechanics-based, real-time lung tumor tracking algorithm to be used during EBRT. The purpose is to eliminate the need for intra-treatment imaging or invasive procedures currently used for real-time tracking of lung tumors. An effective surrogate-driven, biomechanics-based tracking algorithm requires the following components:

- Automatic image processing algorithms to be used for extracting the model requirements from 4D images.
- A robust and accurate lung biomechanical model with adaptive boundary conditions.
- A compact form mathematical model of diaphragm motion to be used for real-time estimation of the diaphragm motion from surrogate signals.
- Robust and accurate functions relating the surrogate signal to the lung boundary conditions.

In Chapters 2-5 of this thesis, we presented the methods used to build each required component for the proposed real-time lung tumor tracking algorithm.

In Chapter 2, a fully automatic anatomy-based algorithm was proposed for segmentation of the entire diaphragm in non-contrast CT images. The challenges associated with the diaphragm segmentation such as its similar tissue density distribution to its surrounding organs are addressed using *a priori* anatomical knowledge about human diaphragm. In fact,

the proposed algorithm takes advantage of the fact that the diaphragm is in contact with its surrounding organs while those organs present sufficiently high contrast regions within the CT images.

Image information required for the lung biomechanical modeling includes segmented lungs and their boundary conditions such as diaphragm motion, ribcage motion, and lung-trachea interface. Given that the proposed diaphragm segmentation algorithm segments the diaphragm's surrounding organs, the segmented organs can be readily used for lung biomechanical modeling.

The proposed algorithm may have limitations pertaining to presence of pathological conditions that may affect the diaphragm's anatomy or the anatomy of its surrounding organs. In our data set, there are cases where the anatomy of the ribcage or the aorta have been altered because of pathology while the results are still sufficiently accurate as the algorithm follows the anatomy of surrounding organs. We believe that as long as the diaphragm remains in contact with its surrounding organs, the proposed algorithm can be used to segment the diaphragm effectively. While these limitations may slightly affect the diaphragm segmentation accuracy, they are not anticipated to have significant effect on the lung biomechanical model accuracy. In fact, the diaphragm portion required for lung biomechanical modeling is the one which is in contact with the lungs and the results indicate that the lung-diaphragm contact surface can be segmented with high accuracy.

The major application of the entire diaphragm segmentation is to develop accurate computational biomechanical models of the diaphragm. The diaphragm computational models can be used in various applications ranging from in-depth understanding of the diaphragm's physiology and developing effective diagnostic techniques of relevant respiratory diseases to computer assisted clinical procedures such as lung cancer radiotherapy and liver intervention. Lung cancer radiotherapy can benefit greatly from accurate biomechanical modelling of the diaphragm as a major driver of lung tumor motion during respiration cycle. In this case, the model can be integrated with the lung's biomechanical model to facilitate accurate prediction of the tumor motion, paving the way for computer assisted motion compensation in radiotherapy procedures.

The results obtained in this study indicate that the proposed algorithm is capable of accurate delineation of the entire diaphragm, paving the way for accurate biomechanical modeling of the diaphragm necessary for many clinical applications. In addition, the sub-algorithms used in this algorithm can be used to extract all the image information required for lung biomechanical modeling, indicating that the first objective of this thesis is fully met in this paper.

In Chapter 3, a biomechanical model was proposed specifically for lung tumor tracking during EBRT. One unique feature of this model is using patient specific loading and material properties data which were obtained from 4D CT imaging data processed within an optimization framework. The lung biomechanical model serves as a core component of the system which determines the tumor location and its geometry throughout respiration. This data can be fed to a robotic system driving a linear accelerator which changes the radiation beam orientation consistent with the tumor motion to achieve optimal EBRT outcome. The proposed lung biomechanics model involves two types of loading. The diaphragm motion related loading defined as prescribed displacement boundary conditions and the trans-pulmonary pressure arising from chest muscle contraction and relaxation. These loading components were determined before treatment using 4D CT image data using optimization. The trans-pulmonary pressure curves obtained through optimization agree well with pressure measurement data reported in the literature. Another important feature of the proposed lung biomechanics model is its treatment of the incompressibility of the lung tissue. The model considers variable tissue incompressibility characterized by Poisson's ratio through various respiration phases. This is essential for studying the lung mechanics under breathing physiological conditions as the air content within the tissue varies substantially from the end exhalation phase, where tissue incompressibility is maximum, to the end inhalation phase, where tissue incompressibility is minimum. Optimized Poisson's ratio variations are consistent with expected trend. In this work, the Poisson's ratio was assumed to be uniformly distributed throughout the lung volume. While this may be a good assumption in healthy lungs, a level of deviation from this uniformity assumption is expected with lung cancer patients or patients who have other lung disease such as Chronic Obstructive Pulmonary Disease (COPD). Especially in the latter, the

Poisson's ratio is expected to be significantly heterogeneous. In such cases, the Poisson's ratio has to be treated as such, leading to a multi parameter optimization algorithm which can be solved to provide diagnostic information in addition to data pertaining to the lung tissue mechanical properties. Among other advantages of using the biomechanics approach for tumor tracking is its ability to compute the variable lung tumor geometry throughout respiration. This can be highly advantageous as the variable volume data can be used in conjunction with an advanced radiation dose distribution algorithm which considers tumor volume geometry variation during EBRT. As indicated earlier, one source of error in our model is the tissue mechanical properties which is expected to be heterogeneous in patients who suffer from lung disease. Despite assuming homogeneous tissue and assigning lung tissue hyperelastic parameters which are not patient specific, the quantitative results obtained in this study are quite favorable. The results published in this chapter satisfy our second goal which was developing an accurate lung biomechanical model suitable for radiotherapy applications.

In Chapter 4, a highly accurate model was proposed for diaphragm motion characterization using principal component analysis. This model was developed to be used as a major component of the biomechanics-based lung tumor tracking algorithm. In the proposed model, we employed the TFI technique to select consistent diaphragm landmarks for all subjects involved in the study. This is essential to ensure diaphragm local region anatomical consistency among the subjects. Unlike existing methods, the proposed model is 3D while motion data was obtained through deformable image registration. Both qualitative and quantitative results indicate favorable agreement between "true" and model-generated diaphragm displacement fields.

It is noteworthy that all subjects enrolled in this study were either lung cancer or COPD patients. While it is known that Cancer and COPD affect functionality of the diaphragm differently, the low number of subjects in each category in this study is not large enough to capture various motion patterns anticipated in the mentioned groups of patients. As such, better results are expected by incorporating more subjects in the process of developing the PCA model. The results presented in this chapter meet our third goal of developing a

compact form mathematical model of diaphragm motion. This paves the way towards using expert system frameworks aimed at studying and modeling respiratory motion for various biomedical applications including our proposed tumor tracking algorithm.

In Chapter 5, the proposed biomechanics-based lung tumor tracking algorithm is completed by developing highly accurate NNs for diaphragm motion characterization and trans-pulmonary pressure estimation from chest motion data. Quantitative validation was performed in two steps. First, the performance of NN was tested on un-seen data where qualitative results indicate favorable agreement between “true” and NN-estimated lung boundary conditions. Quantitative results indicate that the proposed NN-based approach can be effectively used to predict the lung BCs from chest motion data. In addition, the results indicate that the trained NNs work well for prediction of both intra-fraction and inter-fraction variations in trans-pulmonary pressure and diaphragm motion. To further evaluate the NNs, our proposed lung FE model was used to calculate tumor motion in five patients where the “true” BCs and the NN-based estimated BCs were used for driving the lung biomechanical model. Comparison of results obtained from these two sets of boundary conditions indicated that when the chest motion data is used to predict the lung BCs, the accuracy of tumor motion tracking is reduced by less than 5%. This confirms that error propagation from the NN-based boundary condition estimation into typical lung biomechanical model had insignificant impact on the biomechanical model’s overall accuracy. As such, these results indicate the feasibility of biomechanics-based real-time tumor tracking during EBRT. To further evaluate the proposed algorithm towards achieving a higher level of confidence necessary for clinical translation, more subjects should be recruited.

6.2 Conclusions and Future Directions

Results presented in this thesis indicate the feasibility of real-time lung tumor tracking using biomechanical modeling. While these results are encouraging, the number of patient samples are small, and further clinical studies are required to perform a comprehensive assessment of the algorithm performance and its sensitivity to anatomical changes during

treatment, artifacts in 4D CT images, and types of contrast used for imaging (oral or intervenors). While the number of patients used in this study is small, it is justified as the main objective of this thesis was to address the modeling challenges associated with using biomechanics-based tumor tracking algorithms.

As mentioned earlier, there are two challenges associated with biomechanics-based procedures. First, updating the lung BCs in real-time. Second, reducing the FEA computation cost. The main goal of this thesis, which was met in Chapters 2-5, was to address the first challenge. To build upon this work, the first step is to use systematic methods for optimizing the location/number of chest/abdominal markers. Next, one should perform several clinical studies and recruit a sufficient number of patients with different tumor locations and various ranges of tumor motion to assess the algorithms performance for a larger population. Finally, GPU programming or model reduction methods should be used to increase the FEA speed. For instance, statistical FEA developed by our group can be used to speed up the FEA¹.

Like any other real-time tracking method, another step should be added to the algorithm where the motion/deformation is predicted ahead of time to account for system latencies. Aside from real-time tumor tracking purposes, the proposed framework can be used for respiratory motion modeling required for many applications such as radiotherapy treatment planning and lung image reconstruction. The last study, in which the diaphragm motion is obtained from chest motion data, can be used for developing respiratory motion models for other applications such as lung/liver interventions where real-time diaphragm boundary conditions are required.

6.3 Closing Remarks

During the past decades, numerous studies have been conducted to address challenges associated with respiratory motion, including difficulties in imaging and medical interventions. Despite enormous efforts and investments, these challenges are not fully addressed, indicating the complexity of the problem. As presented in this work, breaking the lung tumor tracking problem to smaller problems of lung FE modeling and lung BC prediction from chest motion data results in achieving higher accuracy in motion modeling,

paving the way towards accurate and real-time tracking of lung tumors. While the main objective of this thesis was to develop a real-time tumor tracking algorithm, another important goal achieved in this study was to build a physics-based tool which can be used for better understanding of the respiratory system function. As presented in Chapter 3, the proposed framework for lung biomechanical modeling allows for calculating patient specific trans-pulmonary pressure and incompressibility parameter data. The proposed framework can also be used for calculating patient specific tissue mechanical properties such as stiffness parameters. To address the tissue heterogeneity issue caused by disease, the lung tissue abnormalities can be segmented using automatic segmentation algorithms such as texture detection methods. Next, the segmented regions may be assigned different mechanical properties followed by an optimization step to find the tissue mechanical properties for each segment. As such, the proposed lung biomechanical model can be used in conjunction with lung images and experimental data to increase our knowledge about alterations caused by disease in tissue mechanical properties. To conclude, not only the proposed tracking algorithm can potentially be used for real-time lung tumor tracking, it can also be used effectively for developing better understanding of the respiratory system in normal and pathological situations.

1. Mousavi SR, Khalaji I, Sadeghi Naini A, Raahemifar K, Samani A. Statistical finite element method for real-time tissue mechanics analysis. *Comput Methods Biomech Biomed Engin.* 2012;15(6):595-608. doi:10.1080/10255842.2010.550889.

Appendices

Appendix A: Research Ethics



Western
Research

Research Ethics

Western University Health Science Research Ethics Board HSREB Annual Continuing Ethics Approval Notice

Date: January 09, 2015

Principal Investigator: Dr. Stewart Gaede

Department & Institution: Schulich School of Medicine and Dentistry/Medical Biophysics, London Health Sciences Centre

HSREB File Number: 6917

Study Title: Assessment of clinical and technological factors predicting survival and toxicity outcomes in locally advanced lung cancer, seen at the LRCF between 2004-2010

Sponsor:

HSREB Renewal Due Date & HSREB Expiry Date:

Renewal Due -2016/02/29

Expiry Date -2016/03/08

The Western University Health Science Research Ethics Board (HSREB) has reviewed the Continuing Ethics Review (CER) Form and is re-issuing approval for the above noted study.

The Western University HSREB operates in compliance with the Tri-Council Policy Statement Ethical Conduct for Research Involving Humans (TCPS2), the International Conference on Harmonization of Technical Requirements for Registration of Pharmaceuticals for Human Use Guideline for Good Clinical Practice Practices (ICH E6 R1), the Ontario Freedom of Information and Protection of Privacy Act (FIPPA, 1990), the Ontario Personal Health Information Protection Act (PHIPA, 2004), Part 4 of the Natural Health Product Regulations, Health Canada Medical Device Regulations and Part C, Division 5, of the Food and Drug Regulations of Health Canada.

Members of the HSREB who are named as Investigators in research studies do not participate in discussions related to, nor vote on such studies when they are presented to the REB.

The HSREB is registered with the U.S. Department of Health & Human Services under the IRB registration number IRB 00000940.

Ethics Officer to Contact for Further Information

Erika Baile ebaile@uwo.ca	Grace Kelly grace.kelly@uwo.ca	Mina Mekhal mmekhal@uwo.ca	Vikki Tran vikki.tran@uwo.ca
------------------------------	-----------------------------------	-------------------------------	---------------------------------

This is an official document. Please retain the original in your files.

Curriculum vitae

Education

2012-2017 **Western University**

PhD in Medical Biophysics

London, Canada

2007-2012 **Isfahan University of Technology**

Bachelor of Science in Electrical Engineering

Isfahan, Iran

Publications

1. **Elham Karami**, Yong Wang, Stewart Gaede, Ting-Yim Lee, Abbas Samani, “Anatomy-based algorithm for automatic segmentation of human diaphragm in non-contrast computed tomography images”, *J. Med. Imag.* 3(4), 046004 (Nov 22, 2016).
2. **Elham Karami**, Stewart Gaede, Ting-Yim Lee, Abbas Samani, “Diaphragm motion characterization using chest motion data for biomechanics-based lung tumor tracking during EBRT”, *Proc. SPIE 9786*, Medical Imaging 2016: Image-Guided Procedures, Robotic Interventions, and Modeling, 97860Z (March 18, 2016)
3. **Elham Karami**, Stewart Gaede, Ting-Yim Lee, Abbas Samani, “A biomechanical approach for *in vivo* lung tumor motion prediction during external beam radiation therapy”, *Proceeding of SPIE Vol. 9415*, 941512 (2015).
4. **Elham Karami**, Stewart Gaede, Ting-Yim Lee, Abbas Samani, “Fully automatic algorithm for segmenting full human diaphragm in non-contrast CT Images”, *Proceeding of SPIE Vol. 9417*, 941709 (2015).

5. **Elham Karami**, Stewart Gaede, Ting-Yim Lee, Abbas Samani, “In-vivo lung biomechanical model for effective tumor motion tracking in external beam radiation therapy”, Under review in *Medical Physics Journal*, May 2017.
6. **Elham Karami**, Stewart Gaede, Ting-Yim Lee, Abbas Samani, “PCA-based Model of Human Diaphragm Motion Derived from 4D CT Images for Effective Tumor Motion Management”, Under review in *J. Med. Imag.*, June 2017.
7. **Elham Karami**, Stewart Gaede, Ting-Yim Lee, Abbas Samani, “A Machine Learning Approach for Biomechanics-based Tracking of Lung Tumors during External Beam Radiation Therapy”, Under review in *Journal of Expert Systems with Applications*, June 2017.

Abstracts and Presentations

1. **Elham Karami**, Stewart Gaede, Ting-Yim Lee, Abbas Samani, “A Robust method for tracking the lung tumors during External Beam Radiation Therapy”, submitted to *Imaging Network Ontario*, 2016, Toronto, Canada.
2. **Elham Karami**, Stewart Gaede, Ting-Yim Lee, Abbas Samani, “ PCA-Based diaphragm motion model from 4D CT data”, in *Computer Methods in Biomechanics and Biomedical Engineering and Imaging and Visualization*, 2015, Montreal, Canada.
3. **Elham Karami**, Stewart Gaede, Ting-Yim Lee, Abbas Samani, “Experimentally Validated Biomechanical Model of *in vivo* Lung under EBRT considering Diaphragm Motion Hysteresis”, in *World Congress of Medical Physics and Biomedical Engineering*, 2015, Toronto, Canada.
4. **Elham Karami**, Stewart Gaede, Ting-Yim Lee, Abbas Samani, “Characterizing Human Diaphragm Motion Hysteresis for Biomechanics-based Lung Tumor Motion Prediction during EBRT”, in *Imaging Network Ontario*, 2015, London, Canada.

5. **Elham Karami**, Stewart Gaede, Ting-Yim Lee, Abbas Samani, “Lung Tissue Elasticity Imaging Using X-ray Computed Tomography”, in *Imaging Network Ontario*, 2014, Toronto, Canada.

Awards

1. **2nd Prize in the Poster Presentation Competition**
11th Annual London Imaging Discovery Day, June 21, 2016.

Related Work Experience

1. **Supervision of the following 3 undergraduate student research projects.**
Western University, Canada, 2012-current.
 - a. **Development of a fully automatic algorithm for full human diaphragm segmentation in non-contrast CT images (Implementation in ITK)**
 - b. **Lung Tissue Elasticity Imaging Using X-ray Computed Tomography**
 - c. **A Robust method for tracking the lung tumors during External Beam Radiation Therapy using chest motion data**
2. **Teaching Assistant for "Human and Animal Biomechanics" course, Western University, Canada, 2013-2015.**
3. **Teaching Assistant for "Introduction to Image Processing" course, Isfahan University of Technology, Iran, 2011-2012.**
4. **Teaching Assistant for "Communications I", Isfahan University of Technology, 2011.**